



## MASTER THESIS

### Validated finite element models of composite bones in a sideways load configuration

carried out for the purpose of obtaining the degree of  
Master of Science (MSc or Dipl.-Ing. or DI), submitted at  
TU Wien, Faculty of Mechanical and Industrial Engineering, by

**Julia Theresa Kamml**

1426397  
Friedmanngasse 1c/10  
1160 Vienna

under the supervision of

Assoc. Prof. Dipl.-Ing. Dr.techn. Dieter Pahr

*E317*

*Institut of Lightweight Design and Structural Biomechanics  
Vienna University of Technology*

Lorenzo Grassi PhD

Assoc. Prof. Hanna Isaksson

*Department of Biomedical Engineering  
Faculty of Engineering  
Lund University*

reviewed by

Dieter Pahr  
Institute for Lightweight Design  
and Structural Biomechanics

Bernhard Pichler  
Institut für Mechanik der  
Werkstoffe und Strukturen

Affidavit

I declare in lieu of oath, that I wrote this thesis and performed the associated research myself, using only literature cited in this volume. If text passages from sources are used literally, they are marked as such.

I confirm that this work is original and has not been submitted elsewhere for any examination, nor it is currently under consideration for a thesis elsewhere.

I further confirm, that going to press of this thesis needs the confirmation of the examination committee.

Vienna, June, 2017

---

Julia Kamml

# Acknowledgment

I would like to sincerely thank all the members of the Biomechanics Group at Lund University and all the people who helped me throughout this master thesis, especially my family and friends.

This work could have particularly not be done without the wise advices of my supervisor Dr. Lorenzo Grassi, Prof. Hanna Isaksson and Prof. Dieter Pahr to whom I express all my gratitude.

# Contents

|  |            |
|--|------------|
| <b>Abstract</b>  | <b>V</b>   |
| <b>Kurzfassung</b>   | <b>VII</b> |
| <b>1 Introduction</b>  | <b>1</b>   |
| 1.1 Literature Review - State of the art . . . . .           | 5          |
| 1.2 Motivation and aim of the thesis . . . . .               | 12         |
| 1.3 Structure of the thesis . . . . .                        | 14         |
| <b>2 Background</b>  | <b>15</b>  |
| 2.1 Composite bones . . . . .                                | 15         |
| 2.2 Finite Element Modelling (FEM) in Biomechanics . . . . . | 17         |
| 2.3 Digital Image Correlation (DIC) . . . . .                | 18         |
| <b>3 Material and Methods</b>                                | <b>23</b>  |
| 3.1 Material . . . . .                                       | 23         |
| 3.2 In-vitro DIC experiments . . . . .                       | 24         |
| 3.3 Finite Element Modelling . . . . .                       | 28         |
| 3.4 Validation Process . . . . .                             | 39         |

|  |            |
|--|------------|
| <b>4 Results</b>   | <b>44</b>  |
| 4.1 Repeatability test of DIC  | 45         |
| 4.2 Validation of FE-models at 1120 N  | 55         |
| 4.3 Validation of FE-models at 4000 N  | 62         |
| <b>5 Discussion</b>  | <b>70</b>  |
| <b>A Repeatability of DIC</b>  | <b>75</b>  |
| A.1 Repeatability of displacements and strains - compared to test 3                    | 75         |
| A.2 Deviation of Absolute displacements and Minor and Major strains for every Specimen | 77         |
| <b>B Repeatability of FE-models - qualitative</b>                                      | <b>80</b>  |
| <b>C Inter-specimen repeatability of FEM at 4000N</b>                                  | <b>89</b>  |
| <b>D Validation with all DIC-data points at 1120 N</b>                                 | <b>95</b>  |
| <b>E Validation against single DIC-tests at 1120 N</b>                                 | <b>98</b>  |
| <b>Bibliography</b>  | <b>115</b> |

# Abstract

Subject-specific finite element (FE) models are considered to be a major step in assessing fracture risk and femoral strength in individual patients. In order to bring their application to the clinics their behaviour and accuracy have to be evaluated extensively in vitro, first. Therefore, validation of the adopted FE-modelling procedure against data obtained from mechanical testing is crucial. The aim of this thesis was to validate finite element models of synthetic femurs against experimental measurement data and to automatise this procedure. Five composite femurs were tested in a sideways-fall loading configuration. Full-field minor and major principal strains were measured with digital image correlation (DIC) at the medial femoral neck of synthetic bones during non-destructive tests at a load of 1120 N and 4000 N. About 1600 data points per test obtained from DIC were used for validation. Finite element models were built for each synthetic bone, and eight different sets of boundary conditions were attempted to replicate the experimental loading conditions. A validation algorithm was implemented to accurately register DIC-point clouds on the surface of the FE-models and to automatise the validation procedure. A linear regression analysis was performed between measured and predicted principal strains, resulting in a slope of 0.7 and a coefficient of determination of 0.9 when DIC-data was pooled at a load of 1120 N. We could show that noise has a higher influence on strain derivation of DIC when strains were small, as also reported in literature. For this reason, FE-models were additionally validated at a load of 4000 N. Herein, the slope was 0.8 and the coefficient of determination was 0.8 when a linear regression analysis was performed between principal strains of DIC measurements of one test

and results of one FE-model. This is to the authors knowledge the first study validating FE-models with a continuous field of deformation data at this site and in this specific loading configuration. Our data provides further insight into the strain response at the medial part of the femoral neck, which is crucial for understanding fracture mechanisms.

# Kurzfassung

Osteoporotische Frakturen im Bereich des Oberschenkelhalses stellen die Medizin nach wie vor vor große Herausforderungen. Individuelle Finite Elemente (FE) Modelle, die speziell für den Femur des jeweiligen Patienten berechnet werden, können ein großer Schritt in Richtung Risikoerkennung und Prävention sein. Patienten mit erhöhtem Risiko einer Fraktur könnten so gezielt für die entsprechende Behandlung selektiert werden. Damit diese Methode tatsächlich in der Klinik angewandt werden kann ist eine intensive in-vitro Untersuchung hinsichtlich ihrer Zuverlässigkeit und Genauigkeit vonnöten. Deshalb müssen die FE-Modelle zunächst mit mechanischen Versuchen validiert werden. Das Ziel dieser Arbeit war es, FE-Modelle mit Messdaten zu validieren und diesen Ablauf zu automatisieren. Fünf künstliche Knochen wurden zunächst in einem mechanischen Versuch getestet, wobei ein seitlicher Fall auf den Trochanter simuliert wurde. Dabei wurden minimale und maximale Hauptdehnungen bei einer Last von 1120 N und 4000 N vollflächig mit Digital Image Correlation (DIC) an der Oberfläche im Bereich des medialen Oberschenkelhalses gemessen. Etwa 1600 Datenpunkte konnten zur Validierung verwendet werden. Für jeden Femur wurden jeweils acht verschiedene FE-Modelle entwickelt, die sich hinsichtlich ihrer Randbedingungen unterscheiden. Ein Validierungsalgorithmus wurde implementiert, um die Punktwolken, die durch DIC generiert wurden mit großer Genauigkeit auf der entsprechenden Oberfläche der FE-Modelle zu registrieren und um den Validierungsprozess zu automatisieren.

Die Steigung der Regressionsgerade betrug 0.7 und das Bestimmtheitsmaß lag bei 0.9, wenn die Messdaten bei einer Last von 1120 N gepoolt wurden. Ein FE-Modell

wurde dabei mit einem experimentellen Testset bestehend aus fünf zerstörungsfreien Prüfungen verglichen. Es konnte gezeigt werden, dass Rauschen einen stark erhöhten Einfluss auf die Ableitung der Dehnungen aus den Verschiebungen hatte, wenn die Dehnungen, d.h. Last kleiner waren, wie auch in der Literatur bereits berichtet wurde. Deshalb wurden die FE-Modelle zusätzlich bei einer Last von 4000 N validiert. Hierbei erhielten wir eine Steigung der Regressionsgerade von 0.8, das Bestimmtheitsmaß betrug 0.8. Ein FE-Modell wurde dabei mit den Messdaten einer einzelnen Prüfung verglichen. Unserem Wissen nach ist dies die erste Studie, die FE-Modelle mit vollständigen Messdaten aus DIC an dieser Stelle (medialer Oberschenkelhals) und in diesem Lastfall (seitlicher Fall) vergleicht. Dabei geben unsere Daten und Ergebnisse tieferen Einblick in die Ausprägung der Belastungsreaktionen im medialen Teil der Oberschenkelhalses, was die Grundlage für das Verstehen der Bruchmechanismen darstellt.

# Chapter 1

## Introduction

Osteoporotic hip fractures are a major health problem in western countries and cause considerable societal burdens and expenses in health care [9]. Osteoporosis is a systemic condition which causes microarchitectural deterioration of bone tissue and a decrease in bone density [38]. Vertebrae, wrist and hip are often regarded as the typical sites for osteoporotic fractures, but results of large prospective studies have shown that almost all types of fractures are increased in patients with decreased bone density [11] [43] [46]. Especially elderly people are likely to suffer from hip fractures since risk increases ten-fold with every 20 years of age due to reducing bone strength and increasing number of falls [35] [27]. Ninety percent of these fractures are the result of a simple fall from a standing height [10]. Hip fractures frequently result in disability and are a primary cause of morbidity and mortality [25] [2], with up to twenty percent of the patients dying within the first year following the fracture. Less than half of those who survive regain their previous level of function and independence [34] [29] [8]. As the prevalence of osteoporosis and the incidence of hip fracture increase with age, new preventive strategies are required to face demographic change worldwide [9] [26] [1]. The aim is to reduce the number of fractures by effectively identifying patients with high fracture risk above a certain level for therapy. Effective treatments for osteoporosis are individually adapted to the patient and to the progress of the

disease and include hormone replacement therapy, selective oestrogen receptor modulators, bisphosphonates, Parathyroid hormone, teriparatides, calcitonin, vitamin D and calcium as well as selected exercise programmes [12].

Clinical diagnostic methods of osteoporosis are based on the assessment of bone mineral quantity: the bone mineral density (BMD). BMD is defined as bone mineral mass contained in a certain bone volume of interest (mass per volume). Using a dual energy X-ray absorptiometry (DXA) image of either femoral neck or lumbar spine, BMD is calculated from the attenuation of X-rays in absolute terms as grams of mineral per area (square centimeter) scanned. This is one of the limitations of the DXA approach, as it does not calculate true three dimensional BMD as mass per volume, but uses a two dimensional image.

The World Health Organisation (WHO) criterion for defining osteoporosis is the T-score (see figure 1.2): it is the number of standard deviations that a patient's BMD is above or below the reference value of a healthy thirty-year-old adult. A T-score of -2.5 or less is the threshold for osteoporosis, a T-score between -1.0 to -2.5 indicates low bone mass with already increased fracture risk compared to a healthy thirty year old bone, referred to as osteopenia [39]. The majority of hip fractures occur in patients with bone mineral density in the osteopenic range, this suggests that factors other than bone mineral density contribute to a patient's risk of fracture [38] [51].

One option for assessing the fracture risk is the Fracture Risk Assessment Tool (FRAX) released in 2008 by the WHO. FRAX is estimating the ten-year probability of a major osteoporotic fracture (in the proximal part of the humerus, the wrist, the hip or the vertebrae) and is available as an online tool <sup>1</sup>. The basis of the calculation are clinical risk factors (for a list of risk factors, see figure 1.2). Femoral neck BMD is included as a risk factor, but it is not compulsory for the estimation of the fracture risk. As fracture probability varies markedly among different regions in the world, the risk assessment also includes calculation for different countries [51]. Even if the

---

<sup>1</sup> <https://www.sheffield.ac.uk/FRAX/tool.jsp>

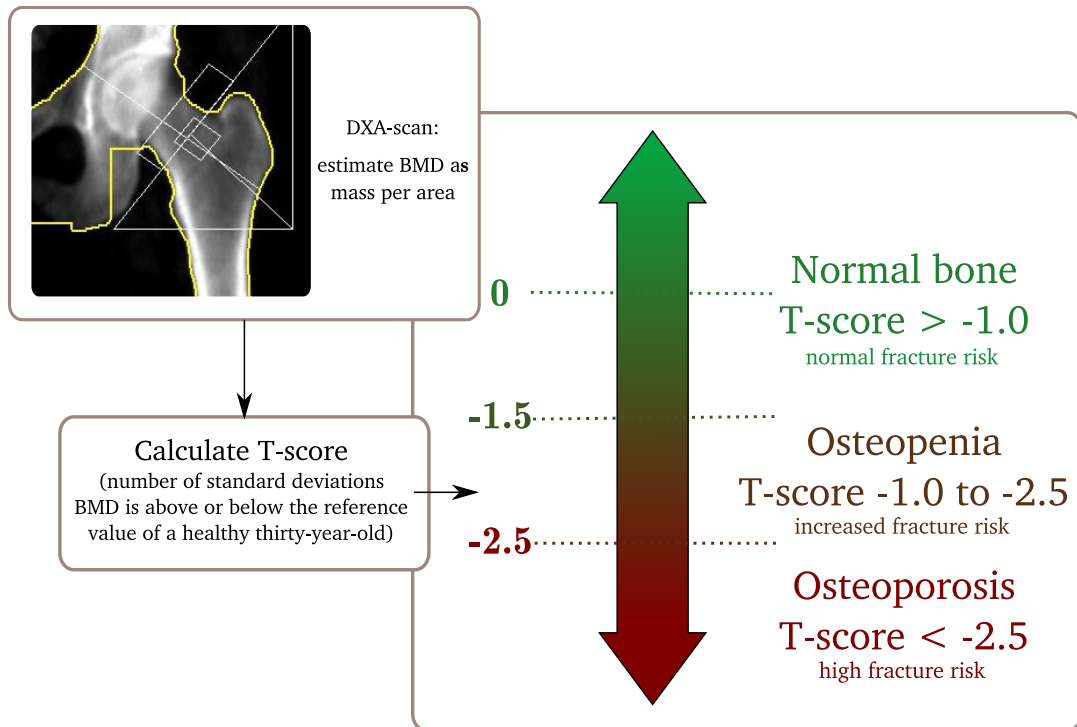


**Figure 1.1:** T-score, WHO-criteria for defining osteoporosis: the number of standard deviation that a patient's BMD is above or below the reference value of a healthy thirty year old

use of clinical risk factors in combination with BMD enhances the accuracy of the hip fracture risk prediction and provides higher specificity and sensitivity than either alone [28], FRAX still is not free from limitations. It excludes, for example, racial and ethnic differences which are known to have influence on the fracture risk [47] [53]. Moreover, the characterisation of spacial distribution of bone mineral density in all three dimensions lacks due to the fact that DXA images are only two-dimensional. Some studies reported that simple tools based on criteria like sex, age, BMD, fractures since the age of fifty or falls during the last twelve months perform as well or better than FRAX and that the effectiveness in selecting patients for treatment and therefore lowering fracture risk has never been quantified [42]. Nevertheless, the greatest problem still remains that the largest group suffering from hip fractures consists of patients who have not been diagnosed having a high risk or osteoporosis, but

The screenshot shows a web-based questionnaire for the FRAX index. At the top, it displays 'Country: UK' and a 'Name/ID:' field with a user icon. A link 'About the risk factors' is visible in the top right. The main section is titled 'Questionnaire:' and contains 12 numbered items:

- Age (between 40 and 90 years) or Date of Birth: Includes input fields for Age and Date of Birth (Year, Month, Day).
- Sex: Radio buttons for Male and Female.
- Weight (kg): Input field.
- Height (cm): Input field.
- Previous Fracture: Radio buttons for No (selected) and Yes.
- Parent Fractured Hip: Radio buttons for No (selected) and Yes.
- Current Smoking: Radio buttons for No (selected) and Yes.
- Glucocorticoids: Radio buttons for No (selected) and Yes.
- Rheumatoid arthritis: Radio buttons for No (selected) and Yes.
- Secondary osteoporosis: Radio buttons for No (selected) and Yes.
- Alcohol 3 or more units/day: Radio buttons for No (selected) and Yes.
- Femoral neck BMD (g/cm<sup>2</sup>): Includes a dropdown menu labeled 'Select BMD' and an input field.

At the bottom right, there are 'Clear' and 'Calculate' buttons.

**Figure 1.2:** Calculation of FRAX index including different risk factors [24]

show a BMD in the osteopenic range [51].

Hence, it can be a major step forward in health care to find other techniques for assessment of fracture risk such as subject-specific finite element (FE) models, calculating the bone strength as a predictor of fracture risk. These numerical models are extracted from a medical image and provide three dimensional shape, material properties and boundary conditions depending on a suitable load case similar to real conditions. The bone strength is most influenced by shape, bone tissue distribution, bone tissue properties and the loading configuration [7] [55]. Thus, subject-specific FE-models developed from computed tomography (CT) data could become a powerful tool in clinical use to predict bone strength and fracture risk, as they take into account structural determinants of bone strength in 3D as well as boundary conditions in different loading situations [44] [48].

In-vitro validation methods for these models are a preliminary requirement for clin-

ical application and use in screening, which stand in need for a well validated tool closely matching experimental findings.

## 1.1 Literature Review - State of the art

### 1.1.1 Validation of FE-models with strain gauges and failure load

Strain gauges are measurement devices attached to the surface of a specimen. They use the change of their electrical resistance while being deformed to calculate surface strains via the so called gauge factor. Since strain gauge measurements are a reliable but restricted method due to irregularities of the surface, many studies validated their FE-models of femurs with data obtained from strain gauges.

The first study to investigate the accuracy of CT-based FE-models of two proximal human femurs already demonstrated that FE-modelling can be an excellent method for estimating strength in single stance and fall [33]. Using a von Mises effective strain failure criterion, the FE-analysis predicted bone failure to within 8 percent of the experimental fracture loads assuming linear isotropic material properties for trabecular bone and within 17 percent assuming nonlinear material properties. However, the predicted surface stresses and strains correlated poorly with the data obtained from SG measurements [33]. It was also demonstrated that critical regions with peak stresses appeared within the intertrochanteric region during fall and not within the Ward's Triangle (see figure 1.3) where bone loss appears first [30]. This may indicate that Ward's Triangle region is structurally unimportant in regard to stresses and strains. The critical strain regions were shown to exist more distally, within the intertrochanteric region during impact of fall.

Quantitative CT-based FE-models had been shown to perform better in the prediction of strength compared to statistical models which were developed based on correlation of regional bone density or dimensions obtained from quantitative CT

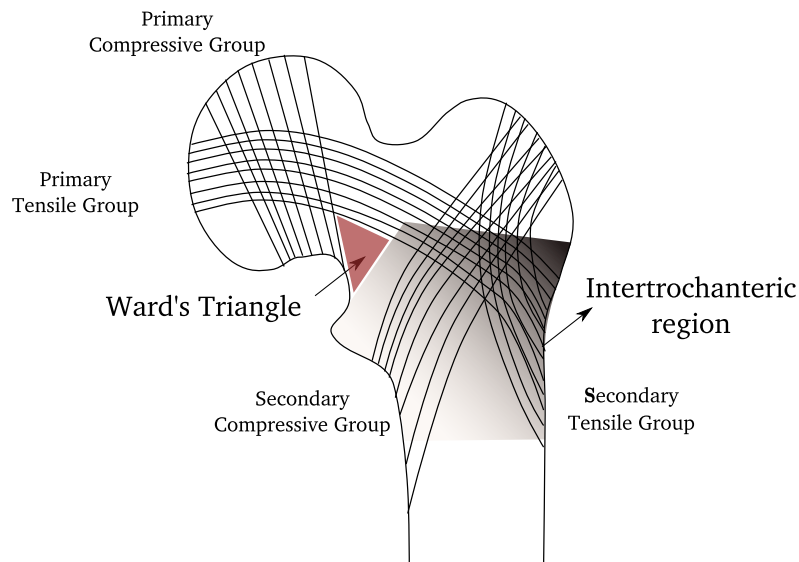


**Figure 1.3:** Intertrochanteric Region and Ward's Triangle: The Ward's Triangle is located where trabeculae which transfer load to the cortical bone shell form a triangle. With increasing bone loss the Ward's Triangle's area increases

and DXA with strength: the statistical models were developed from a training set of 25 cadaver bones loaded until fracture. 26 femurs were afterwards evaluated regarding ultimate fracture load in a single stance loading condition. The FE method explained at least 20 percent more of the variance in strength than the DXA models (with a slope of the regression curve of 0.85 and a  $R^2$  of 0.84), even if all three methods proved to be generally successful at predicting fracture load. With FEA being a relatively young method by then and DXA-imaging based fracture risk assessment being already established, the potential of FEA in orthopedics was proven to be high [7].

*Bessho et al.* validated their CT-based FE-models in terms of principal strains, displacements, yield and fracture loads obtained from in vitro measurements with 12

SGs on eleven fresh frozen cadaver bones in single stance position respectively. Yield and fracture load prediction showed good results with a significant linear correlation between data from simulations and measurements. Strains in the elastic and plastic phase showed slopes of the regression equation of 0.91 and 0.92 and a determination coefficient of 0.93 [3]. *Trabelsi et al.* obtained similar values with a determination coefficient of 0.96 for strains and displacements also validated with SGs in a single-leg-stance loading condition [48].

Another mechanical study was performed in a double-blinded manner. Data of patient-specific finite element models was validated based on QCT with measurements from 5 strain gauges on 12 bones in non-destructive tests. Strains, displacement magnitude and overall bone stiffness were compared applying a load 250 N, 500 N and 1000 N. Validating the FEA with experimental data of all measurements the linear regression showed an  $R^2$  of 0.93 and a slope of the regression curve of 1.01. Looking at the strain measurements separately the FEA correlated with the experimental data by 95 percent ( $R^2 = 0.95$ ) with a slope of the regression curve of 1.04. Regarding the local total displacements on the bone surface, the FEA correlated with the experimental data by 87 percent ( $R^2 = 0.87$ ) with a slope of the regression curve of 0.99 [49].

*Schileo et al.* performed a combined numerical-experimental study comparing FE predicted strains with SG measurements. Eight cadaver femurs with 15 SGs attached were tested non-destructively under six different loading conditions. The best agreement of principal strains provided an  $R^2$  of 0.91 and a slope of the regression curve of 1.01 [44].

Whether a strain-based failure criteria could identify the failure patterns of bone was verified with three cadaver femurs in an single-leg-stance loading condition and it revealed that the proposed strain criterion managed to correctly identify the level of failure risk and the location of fracture onset in the modelled specimens, while Von Mises or maximum principal stress criteria performed less well. *Schileo et al.* therefore propose a maximum principal strain criterion as a in vivo risk factor assessment

in long bones [45]. Therefore, the quality of FEA predicting strains has to be further investigated.

*Koivumäki et al.* validated FE-models of cadaver bones in a sideways fall loading condition, which were generated from CT-scans. The in-vitro tests were conducted until failure. Fracture load was used to compare models and experiments. The estimated fracture loads from FE-models were highly correlated with the experimental data, with a slope of 0.93, an  $R^2$  of 0.87 and an intercept of 258N in a model including both, trabecular and cortical bone. A less complex and less computational expensive model (trabecular bone had been removed, only cortical bone included) had a slope of 1.13, an  $R^2$  of 0.73 and an intercept of -360N, which proves that also these models which need less computational time are suitable for to estimate bone fracture load [32] [31].

Another numerical-experimental study in sideways fall loading configuration was performed by *Grassi et al.* The FE-models of three femora were validated via strains and displacements on 16 different aspects of the bone. Strains measured by SGs were predicted with an  $R^2$  of 0.91 and a regression slope of 1.06. The prediction of displacements showed an  $R^2$  of 0.93 and a slope of 0.87. The highest strain prediction errors occurred in the lateral aspect of the neck of all specimens and was about 30 percent. According to the author, these large errors deserve further investigations, since under sideways fall configuration the lateral neck region is likely to be one of the most strained [20].

| Author                     | Ref  | Material          | Loading condition               | Validation Criteria                                      | Device | Results of Validation   |
|----------------------------|------|-------------------|---------------------------------|--|--------|---|
| <i>Lotz et al.</i>         | [33] | 2 cadaver femora  | single stance and sideways fall | failure stresses and strains                             | 9 SGs  | Load: within 8 percent for linear isotropic material properties, within 17 percent for non-linear ; predicted surface stresses correlate poorly |
| <i>Cody et al.</i>         | [7]  | 26 cadaver femora | single stance                   | fracture load  |        | $R^2 = 0.83$ , $slope = 0.8534$   |
| <i>Bessho et al.</i>       | [3]  | 11 cadaver femora | single stance                   | principal strains, displacement, yield and fracture load | 12 SGs | strain: $R^2 = 0.9292$ , $slope = 0.912$ in elastic phase, $R^2 = 0.9292$ , $slope = 0.919$ in plastic phase                                    |
| <i>Trabelsi et al.</i>     | [48] | 1 cadaver femur   | single stance                   | displacements and strains                                | 11 SGs | displacements and strain gauges pooled: $R^2 = 0.957$ , $slope = 0.965$   |
| <i>Trabelsi et al.</i>     | [49] | 12 cadaver femora | single stance                   | displacements, strains and axial stiffness of specimen   | 5 SGs  | all measurements pooled: $R^2 = 0.93$ , $slope = 1.0093$ , only strains: $R^2 = 0.95$ , $slope = 1.0362$  |
| <i>Schileo et al. 2008</i> | [44] | 8 cadaver femora  | single stance                   | principal strains  | 15 SGs | $R^2 = 0.95$ , $slope = 0.97$   |

| Author                  | Ref          | Material                                      | Loading condition | Validation Criteria          | Device | Results of Validation  |
|-------------------------|--------------|---|-------------------|------------------------------|--------|--|
| <i>Koivumäki et al.</i> | [32]<br>[31] | 40 cadaver femora                             | sideways fall     | fracture load                |        | $slope = 0.929$ ; $R^2 = 0.867$ , (or model only including cortical bone: $R^2 = 0.73$ , $slope = 1.128$ ) |
| <i>Grassi et al.</i>    | [20]         | 3 cadaver femora                              | sideways fall     | strains and displacements    | 16 SGs | strains: $R^2 = 0.91$ , $slope = 1.06$ ; displacements: $R^2 = 0.93$ , $slope = 0.87$                      |
| <i>Dickinson et al.</i> | [14]         | 1 fourth generation composite femur (Sawbone) | single stance     | von Mises equivalent strains | 3D DIC | $R^2 = 0.862$ , $slope = 0.90$   |
| <i>Grassi et al.</i>    | [22]         | 6 fourth generation composite femora          | single stance     | principal strains            | 3D DIC | pooled data: $R^2 = 0.87$ , $slope = 0.84$   |
| <i>Grassi et al.</i>    | [21]         | 3 cadaver femora                              | principal strains | single stance                | 3D DIC | pooled data $R^2 = 0.93$ , $slope = 0.96$  |

Table 1.1: Literature Review - Overview of studies validating FE-models with different criteria

### 1.1.2 Digital Image Correlation in Biomechanics

Optical techniques like Digital Image Correlation (DIC) were only recently introduced to the research field of bone mechanics. It calculates displacements of a specimen (e.g. bone) during loading out of two different images by tracking facets with a specific grey value pattern. Strains can afterwards be derived from displacements. The advantage of DIC as a measurement technique is that it provides full-field (2D or 3D) measurement data compared to the discrete point data obtainable from other techniques like strain gauges.

The reliability and repeatability of surface strain measurements with DIC during destructive compressive testing of composite femurs on the anterior side in stance configuration was investigated by *Väänänen et al.* Composite femurs were used to minimize the uncertainties associated with the testing of cadaveric tissue and to understand the variability of DIC measurements itself. When applied loads were equalized the variation in strains between the bones was 20 – 25 percent. When the maximum strains were equalized, variation in the other regions where strains were lower was 5 – 10 percent. Results showed that the ability of nominally identical composite bones to bear high strains and loads before fracturing may vary between the samples [52]. As the emphasis was on destructive test, it might be interesting to test the repeatability of DIC within one sample in non-destructive tests.

For the understanding of loading, deformation and fracture behaviour of bone or other complex hierarchical materials, DIC has been used in several studies [54] [6] [37] and also provided new insights for refining existing FE models [5].

*Dickinson et al.* used a composite femur in a single stance load configuration and claimed that DIC has proven to be suitable for strain measurement in vitro. Using von Mises equivalent strains to validate FE-models with measured DIC-data they obtained results showing excellent agreement qualitatively and quantitatively (linear regression slope of 0.9 and  $R^2$  of 0.86) [14].

Also in validating and optimising QCT based 2D FE-models of cadaver femurs in a sideways fall loading condition, 2D DIC measurements were used. A good correla-

tion between 2D FEA stiffness prediction and measured stiffness was reported ( $R^2 = 0.71$ ), better than the correlation of BMD and measured stiffness. The qualitative strain field distribution in measurements and simulations showed good similarities [13].

*Grassi et al.* validated strains of FE-models of six composite femora against strain data from DIC obtained during fracture tests in a single-leg-stance loading configuration. FE-models were obtained from CT scans using the same semi-automatic segmentation process as in *Schileo et al.* [44] [45]. Principal strains both during the elastic phase and close to fracture showed a correlation coefficient close to 0.9, with slope and intercept close to unity and one. This was the first study to validate FE-results against 3D principal strain measurements over an entire surface of proximal femur. Evaluation of principal strains allows a better assessment of the tension or compression state with respect to von Mises strains and support the development of a strain based fracture criteria [22]. The same procedure was afterwards applied on 3 cadaver bones: subject-specific FE-models were validated against DIC measurements in the same set-up, obtaining a determination coefficient ( $R^2$ ) of 0.94 and a regression slope of 0.96 with an intercept of  $133\mu\varepsilon$  [21].

## 1.2 Motivation and aim of the thesis

In order to introduce subject-specific FE-models to clinical use their accuracy has to first be validated extensively *in vitro*. Many studies concentrated on directly predicting bone strength using stress- or strain-based criteria and a quasi-axial loading configuration, while validating models with strains in a non-destructive test condition can help to get further insight into limitations of FEM in the elastic regime.

The aim of this thesis was to investigate the accuracy of the strain prediction of FE-models with low magnitude (1.5 times body weight) load in the inferior aspect of the medial femoral neck of five composite femurs in a sideways fall loading configuration. This site is known to be a critical region for fracture due to high stresses in sideways-

fall [4]. The intention was to build FE-models that accurately predict strains in the femoral neck and automatise validation against DIC strain data.

Finite element predicted strains were compared to strains calculated from DIC. So far the majority of the studies used strain gauges (SGs) for validating strains and displacements obtained from FE-models with data from in vitro testing. The use of SG is restricted in the number of measurement points, whereas an optical technique such as DIC provides a continuous field of deformation data over a femoral surface [22]. Composite bones were employed since repeatability and reliability of DIC can be examined and also for practical reasons as they are easier to handle during the experiments and do not need special treatment such as cadavar bones. Furthermore, the automation of the modelling and validation procedure was easier to handle.

Fracture is the result of excessive strain or stress within the bone, so it represents the terminal manifestation of the loading process [3]. Nevertheless, stress and strain development during the loading process should also be validated in non-destructive tests. Furthermore, even if the assessment of the ultimate load works reliably in FEA, for further understanding the mechanisms behind bone deformation, validations of models with lower loads are necessary.

Simulating sideways fall is more applicable for estimating fracture risk than e.g. simulation of single stance, as the direction of the load application is proven to have a significant influence on bone strength [55] and most hip fractures occur due to fall to the side.

The validation of FE-models with minor and major principal strains in a sideways fall using DIC has not been performed so far. As it is crucial for the development of a fracture risk criteria using FEM to evaluate a sideways fall loading condition, we decided to close this gap.

### 1.3 Structure of the thesis

Chapter 2 provides a general overview and background knowledge of the material used and methods applied in this thesis.

First, material and structural properties as well as advantages of composite bones are explained. Then, FEM and its use in the field of biomechanics is described and a general overview of the procedure is given. Finally, DIC, the optical method used for validating the FE-models with in vitro test data is presented and procedures for extracting displacements and strains are explained.

Chapter 3 describes specifically how materials and methods were applied and how results were generated in this numerical-experimental study.

Material used for preparing the specimen is presented first. Then, the setup and performance of the DIC experiments are described. Afterwards, a description of how FE-models were generated is given. Last, the repeatability test of DIC and FEM and the validation process and their implementation are explained in detail.

Chapter 4 reports the results of the repeatability tests and validation.

First, results from repeatability tests of DIC are shown. Then, results of repeatability tests of FEM and results of validation at corresponding load are presented.

Finally, in chapter 5 discussion of the thesis is given.

Results, limitations and further investigations are discussed. Moreover, results are compared to the literature. Further, a summary of the thesis outcomes is presented.

The appendix provides additional data that was obtained during investigation and might be interesting for the reader to gain further information.

# Chapter 2

## Background

The material used and methods applied in this thesis are reviewed in the following chapter. First, material and structural properties of composite bones are presented. Then, FEM and its use in the field of biomechanics is described and a general overview of the procedure is given. Last, DIC, the optical method used for validating the FE-models with in vitro test data is explained shortly.

### 2.1 Composite bones

Composite bones are widely used in orthopaedic biomechanics research as they mimic the shape and material properties of human bone. Introduced in 1987, they have undergone several design changes: First and second generation bones were still limited by need of manual craftsmanship and were made of a rigid polyurethane foam core (mimicking trabecular bone) surrounded by an epoxy-reinforced, braided glass sleeve (first generation) or fiberglass-fabric-reinforced epoxy (second generation).

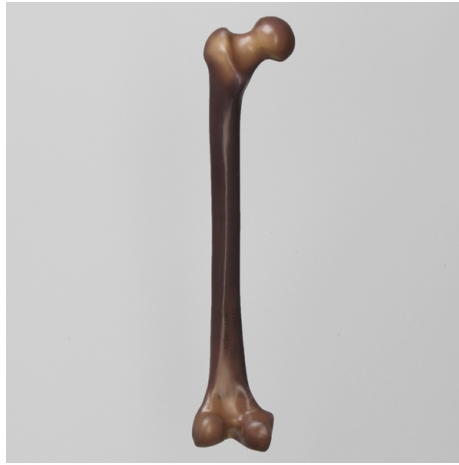


**Figure 2.1:** Fourth Generation Composite Femur (Sawbone)

With the introduction of new materials and manufacturing processes, composite bones are now manufactured with a pressure-injected technique by which short glass fiber reinforced epoxy is injection-molded around the polyurethane foam core and forming the cortical bone [15]. The currently best models are fourth generation composite bones which are an improved version of the third generation. Their advantage is the highly accurate reproduction of the biomechanical properties of human bone when placed under bending, axial and torsional load and the high consistency between the testing data. *Heinen et al.* as well as *Gardener et al.* tested large size fourth generation composite femurs under axial compression, bending and torsion, where torsion was not only applied on the diaphysis, but also on the femoral neck. The bones showed intra specimen variations under 10 percent for all load cases considering load and deflection or torque and rotation angle data. The failure modes of the composite bones were close to those of human cadaver bones reported in literature [23] [17].

Generally, composite bones may be superior to cadaver bones in specific experimental setups for several reasons e.g. lower costs, easier access, preservation and consistency between the specimens. Using DIC, the application of the speckle pattern on the

bone is facilitated. Thus, composite bones can easily be used for a pre-test before performing in-vitro test on cadaver bones as we did.

## 2.2 Finite Element Modelling (FEM) in Biomechanics

FEM is a numerical method to calculate mechanical behaviour and for example fracture risk or potential vulnerabilities. In solid bodies the deformation behaviour influenced by loading conditions in combination with internal determinants such as shape, material density and properties can be simulated. The method numerically approximates the solution of differential equations. In solid bodies, these bodies are divided into a finite amount of smaller parts with relatively simple shape, which are called finite elements. For each finite element the solution of the physical variable of the analytical partial differential equation of interest is approximated numerically by known initial functions and afterwards these equations are assembled into a larger system of equations that models the entire body subdivided by the finite element mesh. By using higher-order initial functions or applying a finer mesh the accuracy of the discrete solution can be increased to a certain level until solutions are converging.

While it evolved in the late 1950s it is now also a commonly used technique in orthopaedic research. FEM is used to predict not only failure and fracture risks, but also to evaluate stresses and strains in structures with complex inside and outside properties (e.g. changing E-modulus with every element depending on the grey value in CT-scans), with *Lotz et al.* applying it first on femurs to predict mechanical behaviour [33]. The strength of a bone can be characterised through internal (shape, bone tissue distribution and bone tissue properties) and external determinants (loading conditions) [7]. Bone has complex non-linear structural properties. Since FE-models can

take all these factors into account they can be used to evaluate stresses and strains in bone under loading. Over the years many studies have been conducted employing subject-specific FE-models. In parallel with computational power, complexity of the models increased. Only recently there is a trend towards simplified models to make these applicable in the clinics.

Nevertheless, the procedure of generating subject specific FE-models from bones typically follows these principles:

1. CT-scanning of the femur
2. Segmentation: extracting the geometries of the bone components based on their different density determined by grey value
3. Meshing: dividing solid geometry into a finite amount of small parts with certain refinement matching the problem
4. Applying material properties: based on the different material properties of each finite element based on the bone density (corresponding with gray value in CT-scans)
5. Defining boundary conditions resembling best the original loading situation and ultimately simulating the model response using a FE-solver package

## 2.3 Digital Image Correlation (DIC)

Digital Image Correlation is an optical non-contact technique to measure full-field strains and displacements e.g. during mechanical testing. It can be applied in different dimensional scales from microscopic to macroscopic level. Non-contact and full-field measuring are the advantages of DIC compared to other techniques such as SGs. With SGs only a specific amount of about 16 discrete points on the surface of the femur can be measured, which are sometimes not sufficient to monitor the experiment. Furthermore, DIC can provide a more complete description of the behaviour of specimens during in vitro tests.

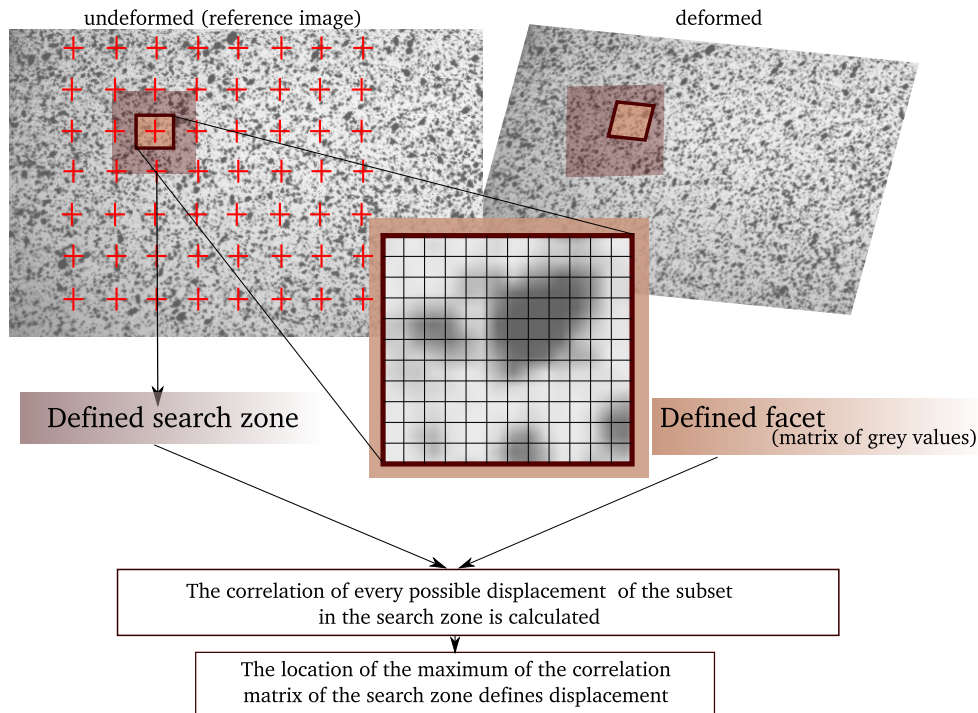


**Figure 2.2:** DIC - calculation of displacements in a 2D case

Biological specimens are mostly inhomogeneous and anisotropic, therefore it is extremely important to obtain full-field measurements, ideally with a contactless technique [40]. The advantage of contactless measuring is that there is no interference with the surface of the specimen and that for measuring no prerequisites for fixing devices on the specimen are needed. The rapid development of digital imaging technologies also results in the possibility of obtaining more accurate spatial and time resolved strain data. Nevertheless, DIC was only recently introduced in the field of bone mechanics and no consensus exists on its reliability for bone mechanics [19]. DIC provides full-field displacements to sub-pixel accuracy by comparing two digital images of the surface of interest acquired in undeformed (reference) and deformed states and can be implemented both in a two-dimensional (2D-DIC, with a single camera) and a three-dimensional (3D-DIC, using two or more cameras) version [41]. A small subset of the image characterised by a specific distribution of grey values is

tracked during the measurement. Based on its position in the reference image displacements are calculated during the different stages of image acquisition. In order to achieve different gray values on the surface a speckle pattern has to be applied, e.g. by spraying black and/or white paint or by applying speckles by hand. Cameras are placed with the optical axis normal to the specimen surface. Here, the procedure for a 2D-computation is explained (see also figure 2.2). The region of interest within the images is organised as a grid consisting of points to be analysed. The images are divided into smaller sub-images (facets or subsets) around the analysed points. Each facet is represented by a grey value distribution of pixels (matrices of grey values) and characterised by the information about this pattern and the location of the facet in space. A correlation algorithm identifies the best matching regions of the two images. Hereby, the definition of a search zone is not necessary, but recommended as it reduces computational cost. A search zone is a submatrix over which the correlation of the facets between the two pictures is calculated. The DIC algorithm works as a loop for each point of the analysed grid, calculating the correlation between the facet in the reference state and all the possible subset configurations within the search zone of the deformation state. The entry giving the maximum correlation coefficient within the matrix obtained is taken as the new position of the analysed point. After having performed the DIC algorithm on all entries, a matrix with displacements over the horizontal and vertical directions is obtained for each entry. A full-field displacement field can be extrapolated [18] [40].

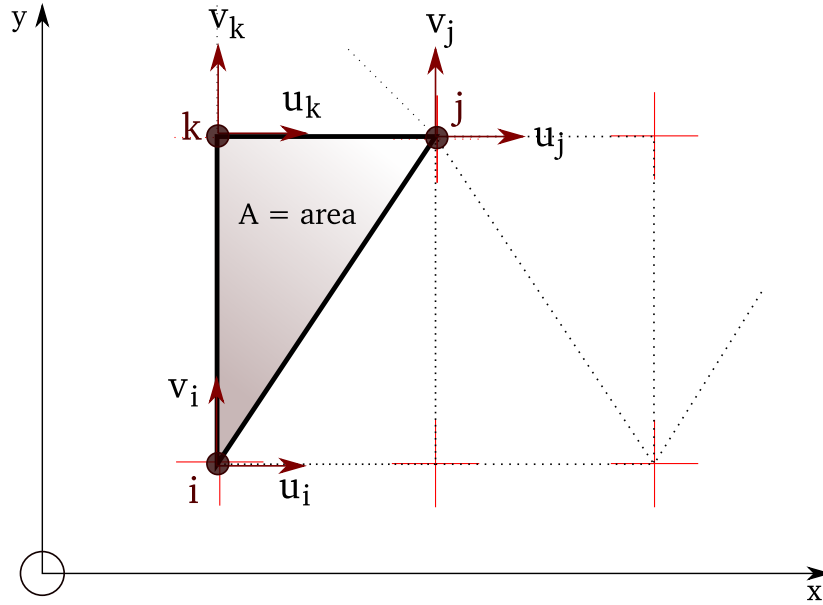


**Figure 2.3:** Constant strain triangular element in its undeformed state, in the point grid.  $u_{i,j,k}$  and  $v_{i,j,k}$  are the displacements in x- and y-direction

To estimate the strain field, several procedures can be applied, e.g. calculation of strains as displacement gradients by using different algorithms or with a numerical differentiation process. Triangulating the point grid and defining a set of strain triangles is one method. Likewise in the FEM, the Green-Lagrange strain tensor is derived from nodal coordinates and displacements.

$$\mathbf{G} = \frac{1}{2}(\mathbf{F}^T \mathbf{F} - \mathbf{I}) \quad (2.1)$$

$\mathbf{F}$  is the deformation gradient with

$$\mathbf{F} = \begin{bmatrix} \frac{\partial x}{\partial X} & \frac{\partial x}{\partial Y} \\ \frac{\partial y}{\partial X} & \frac{\partial y}{\partial Y} \end{bmatrix} = \mathbf{I} + \begin{bmatrix} \frac{\partial u}{\partial X} & \frac{\partial u}{\partial Y} \\ \frac{\partial v}{\partial X} & \frac{\partial v}{\partial Y} \end{bmatrix} = \mathbf{I} + \mathbf{D}$$

$\mathbf{D}$  is the displacement gradient tensor.  $u$  and  $v$  are the components of the displacement vector in  $x$  and  $y$  direction, respectively. The displacement vector can be obtained from the element shape functions  $N_i$ ,  $N_j$ ,  $N_k$  and the displacement components at each node  $u_{i,j,k}$  and  $v_{i,j,k}$ .

$$\mathbf{u} = \begin{bmatrix} u \\ v \end{bmatrix} = \begin{bmatrix} N_i & 0 & N_j & 0 & N_k & 0 \\ 0 & N_i & 0 & N_j & 0 & N_k \end{bmatrix} \begin{bmatrix} u_i \\ v_i \\ u_j \\ v_j \\ u_k \\ v_k \end{bmatrix} \quad (2.2)$$

with

$$N_i = \frac{1}{2A} [x_j y_k - x_k y_j + (y_j - y_k)X + (x_k - x_j)Y] \quad (2.3)$$

$$N_j = \frac{1}{2A} [x_k y_i - x_i y_k + (y_k - y_i)X + (x_i - x_k)Y] \quad (2.4)$$

$$N_k = \frac{1}{2A} [x_i y_j - x_j y_i + (y_i - y_j)X + (x_j - x_i)Y] \quad (2.5)$$

The components of the displacement vector  $\mathbf{u}$  can be derived with respect to  $X$  and  $Y$ , which allows the calculation of the deformation gradient  $\mathbf{F}$  and the Green-Lagrange strain tensor  $\mathbf{G}$  as a function of the nodal coordinates and displacements [18].

The displacement fields obtained with DIC are very accurate, whereas the derivation increases the influence of noise. Therefore the strain field is generally affected by large random error. In order to obtain better results, filtering can be applied to the digital images, to the DIC-computed displacement field, and/or to the DIC-computed strain field [40]. This has to be taken into account when using DIC in order to obtain strain fields.

# Chapter 3

## Material and Methods

In this chapter the material used for preparing the specimen is presented first. Then, the setup and performance of the DIC experiments are described. Afterwards, a description of how FE-models were generated is given and finally the validation process is explained. This thesis is using techniques of *Grassi et al.* [22] [18] and *Väänänen et al.* [52] for modelling and validating a the sideways fall FE-model of a proximal composite femur.

### 3.1 Material

Five fourth-generation large-sized composite femur bones (model 3406, *Sawbones, Pacific Research Laboratories Inc., Vashon, USA*) were cut approximately 15 cm below the minor trochanter and embedded in an aluminium pot ( $40 \times 41.5 \times 49$  mm) which was filled with epoxy (*Technovit 4071, Heraeus Kulzer, Wehrheim, Germany*). A CT-scan was taken of all five samples (*BRILLIANCE 64, Phillips*) in air, with a resolution of 1.2 pixel per millimeter and a slice thickness of 1 mm (X-ray tube current 180 mA, voltage 120 kVp).

## 3.2 In-vitro DIC experiments

The design of the in-vitro testing was not performed within this thesis, but experimental data was used for validation of FE-models. Therefore, the procedure is briefly explained.

### 3.2.1 Experimental Set-up

The schematic setup of the experiments can be seen in figure 3.1.

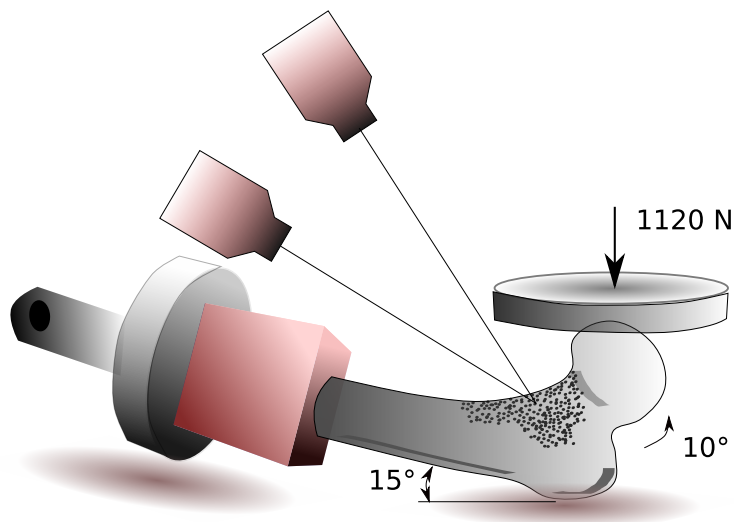


**Figure 3.1:** Setup of the experimental measurements using 3D-DIC

The composite femurs were first sprayed matt white to increase contrast and then painted with random black speckles, applied with a permanent marker on the anterior and posterior inferior femoral neck (see figure 3.2a). Afterwards, each of the five femurs was tested in a sideways fall condition (10 degrees abduction, 15 degrees

internal rotation). A dedicated aluminium jig was used to hold the bone in position while applying load with the loading device (*5500R, Instron, Inc.*).



(a) Speckle pattern on femur (b) Experimental setup in the lab with jig, loading device and light sources

**Figure 3.2:** Mechanical tests

A set of five non-destructive displacement controlled tests was performed at a rate of  $10 \text{ mm min}^{-1}$  with a pre-load of  $20 \text{ N}$  up to a load of  $1120 \text{ N}$  for each bone. From the size of the femur ( $48.5 \text{ cm}$ ) the height of a person owning that femur was estimated to be  $180 \text{ cm}$  [50]. The ideal body weight of a subject of the height is  $76 \text{ kg}$  [36]. Multiplied by  $1.5$  a load of  $1120 \text{ N}$  was obtained.

Afterwards each bone was tested until failure with a pre-load of  $20 \text{ N}$  and a loading rate of  $10 \text{ mm s}^{-1}$ .

The deformations during mechanical testing on the inferior medial femoral neck were recorded by a 3D-DIC system, consisting of two high-speed digital cameras (*Fastcam SA1.1, Photron, Inc.*,  $2 \text{ Mpx}$  resolution,  $200 \text{ fps}$ ). Two high intensity cold light sources (*DX15, Hedle GmbH, Germany*) provided diffuse light for the recording (see figure 3.2b).

A load cell (maximum axial load 100 kN, accuracy 0.5 percent of the reading within 1/500th of the load cell capacity, Instron, Inc.) measured the contact force at the femoral head. A digital acquisition module (DAQ, *Isi-DAQ-STD-8D*, *Isi-Sys, GmbH, Germany*) sampled the analogue signals (load applied on femoral head) of the load cell at the same frequency as the cameras were recording and synchronised them with the digital clock signal from the master camera. Therefore, force and displacements of the loading device can be associated with the corresponding image of DIC. An action camera (*Panasonic HX-A100*, 848x480 pixels, 200fps) was placed on the back of the loading device to record the inferior side of the neck.

Displacement and strain fields were calculated from the obtained images applying DIC. The software used for this purpose was called Vic3D (*v7, Correlated Solutions, Inc.*). Displacements were filtered fitting a cubic spline to the displacements at each facet over time, afterwards strains were derived from displacements.

### 3.2.2 Repeatability test of DIC

#### **Repeatability within every test set - point clouds, displacements and strains**

The tests of each specimen were compared to each other to gain additional information about repeatability of DIC in non-destructive tests. Within each set of tests (5 per femur) the third test was compared to the four others. Point clouds were also compared concerning their form by registering point clouds within every test set on point clouds of test 3. Afterwards, the surface was triangulated and the distances between the two point clouds were plotted on this surface represented by a specific colour. The repeatability tests were also performed in Matlab (*R2015b, MathWorks Inc.*), comparing displacements and major and minor principal strains at the first level where a force of 560 N and 1120 N was had been reached. First, the three-dimensional point clouds cropped in a way that outliers were excluded and then registered on one another with an rigid iterative closest point (ICP) registration algorithm provided in

Matlab. A sphere of 0.25 mm was created around the points of reference test 3 and displacements and strains of points within this sphere were compared to each other. The location of highest errors was determined to see whether the error is systematic. Displacements and major and minor principal strains that are 2 times higher or less than 0.5 the reference value are marked as outliers.

### Inter-specimens repeatability of DIC

The second repeatability test was performed to get information about the repeatability between the specimens in the region of interest. The procedure was similar to that used in the validation process in section 3.4. First, the DIC-point clouds were cropped to exclude outliers, by removing points which were not located in a sphere of 200 mm around the center of the DIC point cloud. The five DIC-point clouds per specimen were first registered on the FE-point cloud (see also figure 3.11) of external FE-nodes on the bone surface of specimen 1. For this purpose, the points on the outer surface of the FE-point cloud of the cortical component were extracted. The DIC-point clouds were then translated and rotated in a way to be positioned close to their final position and in the end registered on the surface with using an algorithm for rigid iterative closest point registration. By registering the five point clouds per sample on the surface of specimen 1 the data was pooled. DIC-data at a load of 1120 N was selected and cropped to the region of interest, that was used for validation later on (see figure 3.12). Data points with a  $\sigma = -1$  or  $\sigma \geq 0.02$  were excluded according to the recommendations of the Vic3D 2007 software guidelines<sup>1</sup>. Sigma is the confidence interval for the match at this point in pixels, so it is an indicator for the quality of the measurement. If sigma is  $-1$  the measurement is not valid. External elements forming the surface of the femur were extracted with the procedure also described in 3.4.2. The center and radius of each element were calculated in a way that the surface of the sphere contains the three principal nodes of the elements. The major and minor principal strains of DIC-points within each

---

<sup>1</sup> <http://www.correlatedsolutions.com/installs/Vic-3D-2010-manual.pdf>

sphere were averaged. The averaged data of each element of every specimen was compared to specimen 1 and mean and standard deviation of the minor and major principal of every bone were calculated to compare these values.

Finally, the distribution of minor and major principal strains was qualitatively compared by triangulating the surface and plotting major and minor principal strains on the surface where the absolute value is represented by a specific color.

### 3.3 Finite Element Modelling

The FEM procedure applied to each of the five bones can be divided into four main steps: Segmentation, Reverse Engineering, meshing and generating FE-models. A further description of the single steps will be provided in the following sections. For a general overview of the steps, please see figure 3.3

#### 3.3.1 Segmentation

The CT-scans of the five specimens were extracted and processed in *Seg3D* (*Seg3D Segmentation, CIBC, University of Utah, USA*) in a semi-automatic segmentation process. In order to extract the different components of the composite bone with different mechanical properties, different thresholds of gray value were applied and mask filters used. The surfaces of the components were extracted as triangular meshes.

#### 3.3.2 Reverse Engineering

The triangular meshes were first remeshed in *OpenFlipper* (*OpenFlipper, OpenMesh, RWTH-Aachen University, Germany*) in order to smooth the geometry (see table 3.1). Non-Uniform Rational B-Splines (NURBS) models were created from the triangulated geometries through a reverse engineering process (*Rhino v4.0, Robert*

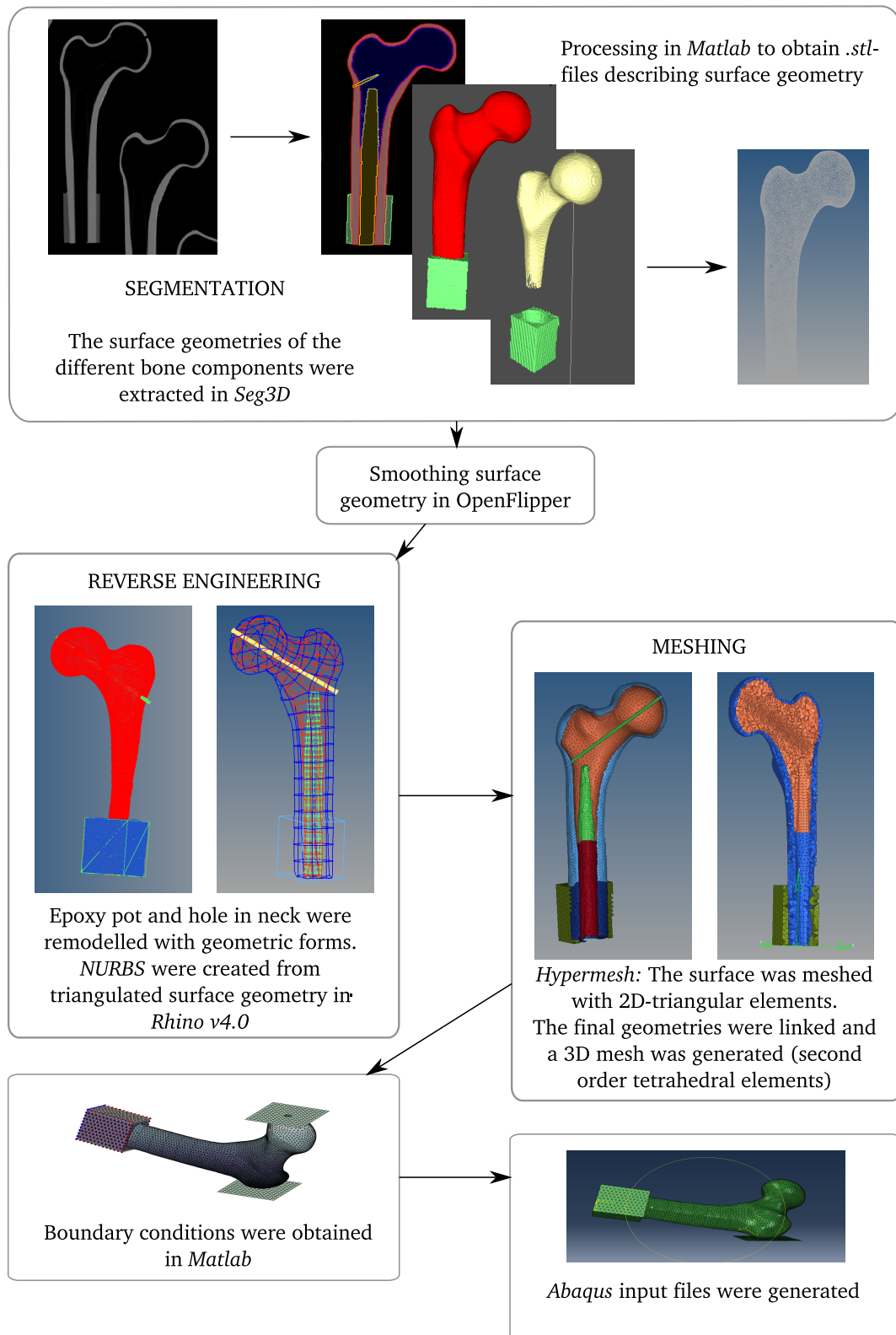


**Figure 3.3:** Finite Element Modelling: An overview

| Geometry                  | Remeshed to |
|---------------------------|-------------|
| Outer Shell Cortical Bone | 3 mm        |
| Cortical Bone             | 2 mm        |
| hole at distal position   | 1 mm        |

**Table 3.1:** Smoothing of the mesh in *OpenFlipper* applied previous to Reverse Engineering

*McNeel Ass., Seattle, USA*). The geometry of the epoxy pot and the hole which is located lengthways the femoral neck were modelled with geometrical shapes (cuboid and cylinder). The created surface curves were exported as *iges*-files.

### 3.3.3 Meshing

Meshes consisting of 10-node unstructured tetrahedral elements were built in *Hypermesh* (*Hyperworks, 14 Release, Altair Engineering Inc., Troy, USA*), based on the imported *iges*-files.

First, a two-dimensional triangular mesh with three nodes per element was built over all surfaces for each surface component respectively. The mesh configuration is varying over the geometry, i.e. in the regions of interest where critical stresses are expected (femoral neck), the mesh is kept smaller (2 mm) than in the other parts of the femur (3 mm) or on the surface of the epoxy pot (4 mm). Afterwards, a three dimensional mesh consisting of second-order tetrahedral elements (10 nodes per element) was created from the triangular element surfaces for each component.

### 3.3.4 Defining boundary conditions

The model consists of three different components (cortical bone, trabecular bone, epoxy pot) with different material properties (see table 3.3 and figure 3.4 (1)). The elements of cortical bone were again subdivided into three sections of head, neck and stem, since orientation of mechanical properties in these regions is different due to

different manufacturing methods influencing the orientation of material properties (see figure 3.4 (1)). The coordinate system was adjusted consistently in all five models. Nodes and elements were exported from the *Hypermesh*-environment and further processed in *Matlab*.

Boundary conditions were extracted in *Matlab* by importing only boundary nodes of the second order elements. The toolbox *iso2mesh* [16] was used.

A local coordinate system was defined in which the origin was contained in the center of the base of the epoxy pot (see figure 3.4 (6)). Node numbers for applying load on the femoral head and blocking at trochanter were determined by looking for the highest (where trochanter touches panel) and lowest (load is applied on femoral head) nodes in direction parallel to load (figure 3.4 (2)). Nodes for applying BC at the epoxy pot were found by looking for extremal values of nodes on the surface of external epoxy nodes (figure 3.4 (3)). The numbers of elements of contact surfaces at head and trochanter and the appropriate orientations of these elements were obtained by running a loop comparing node numbers of elements around the maximum and minimum points and node numbers of the external cortical nodes. Thus, element based surfaces could be defined (figure 3.4 (5)).

The femurs were rotated -15 degrees around the z-axis and 10 degrees around the y-axis respectively to simulate the loading configuration (see figure 3.4(6)). The orientation of mechanical properties of cortical bone in the neck was extracted as axis of a cylindrical hole in the neck and head of the femur (present due to manufacturing), using a straight line between the two averaged points of the hole boundaries in trabecular bone. For the orientation of the material properties in cortical bone, also see figure 3.4 (1).

Eight FE-models were implemented in *Abaqus* with different sets of boundary conditions, ranging from a simple node-based constraints to modelling contact. Nodes were imported as one node set and then node and element sets for different BC were defined and imported. Material properties as indicated by the manufacturer can be seen in

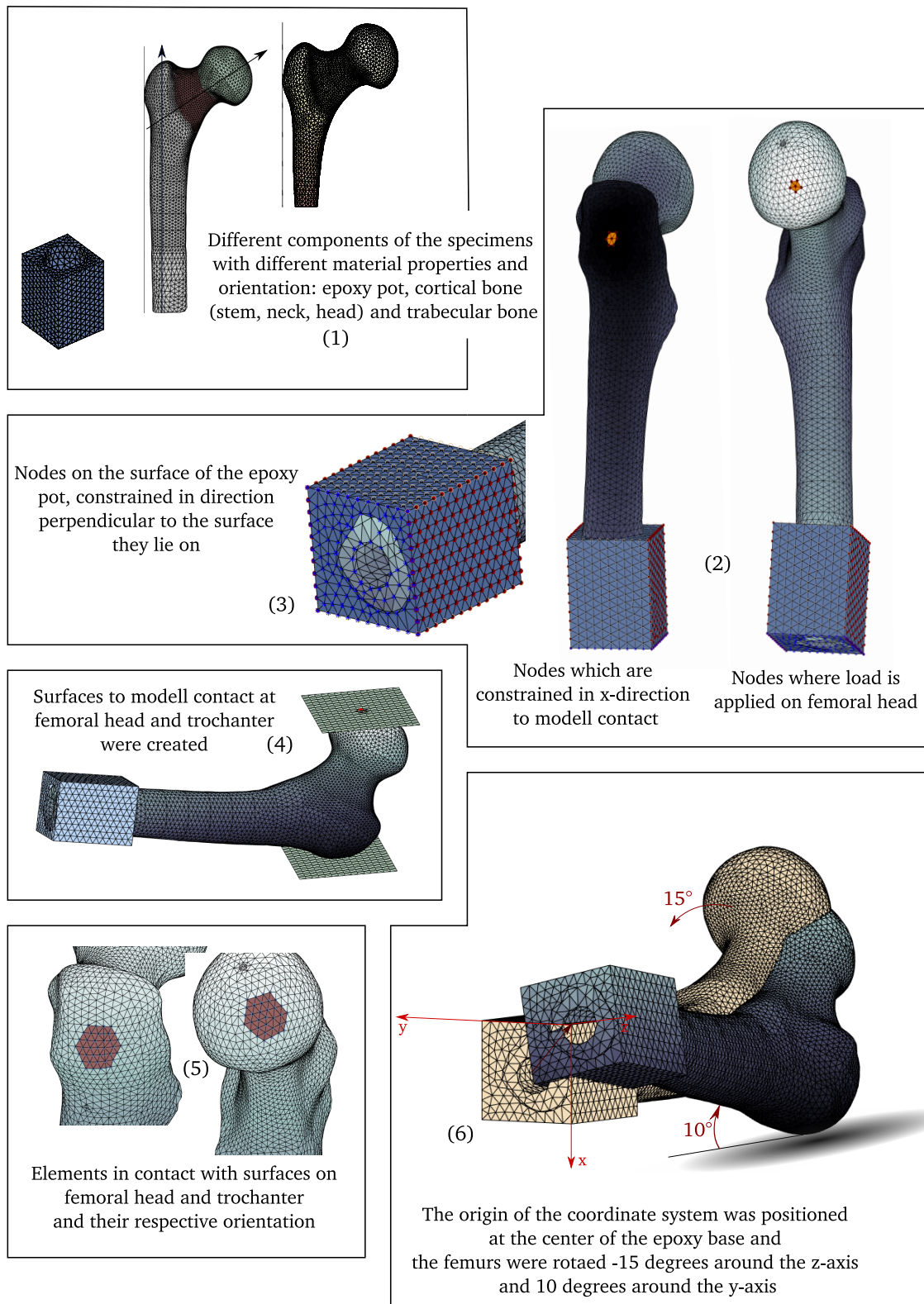


**Figure 3.4:** Different components, prerequisites and nodes for applying BCs were extracted in *Matlab*

table 3.2. Three dimensional tetrahedral second order continuum elements (element type C3D10) were used for meshing the specimen itself. The rigid surfaces for modelling contact at head and trochanter were made of rigid triangular three-dimensional elements (element type R3D3). For further description of the FE-models, please see table 3.4.

| material properties  | Cortical, longitudinal tensile | Cortical, longitudinal compressive | Cortical transverse tensile | Cancellous, compressive |
|----------------------|--------------------------------|------------------------------------|-----------------------------|-------------------------|
| Density [ $g/cm^3$ ] | 1.64                           | 1.64                               | 1.64                        | 0.27                    |
| E-modulus [ $MPa$ ]  | 16 000                         | 16 700                             | 10 000                      | 155                     |
| Poisson ratio        | 0.26                           | 0.26                               | 0.26                        | 0.3                     |

**Table 3.2:** Material properties for the cortical and trabecular part of the composite bones in use

| element set        | E-modulus [ $MPa$ ]    | Poisson | orientation | property    |
|--------------------|------------------------|---------|-------------|-------------|
| Epoxy              | 2500                   | 0.3     | global      | isotropic   |
| Trabecular bone    | 155                    | 0.26    | global      | isotropic   |
| Cortical bone stem | 16 000, 10 000, 10 000 | 0.26    | global      | orthotropic |
| Cortical bone neck | 16 000, 10 000, 10 000 | 0.26    | neck axis   | orthotropic |
| Cortical bone head | 16 000                 | 0.3     | global      | isotropic   |

**Table 3.3:** Material properties and orientations of the different bone components

### 3.3.5 Repeatability of FE-modelling

The results of the models in the region of the medial femoral neck were qualitatively compared by triangulating the surface and plotting major and minor principal strains on the surface where their value is represented by a specific color. Mean and standard deviation of every bone and model were calculated from the strains in the medial femoral neck area.

|                                | <b>Epoxy pot</b>   | <b>Femoral head</b>  | <b>Trochanter</b>   |
|--------------------------------|--|--|---|
| <b>Model 1</b><br>(Figure 3.5) | Epoxy pot constrained: lateral sides and base area constrained in direction perpendicular to surface ; | Load directly applied on femoral head: $\frac{1120N}{n}$ or $\frac{4000N}{n}$ , were $n$ is the number of neighbouring primary nodes of node with minimum x-value                  | contact node with maximal x-value and neighbouring primary nodes constrained in x-direction   |
| <b>Model 2</b><br>(Figure 3.6) | see Model 1  | see Model 1  | contact modelled as <i>*CONTACT PAIR, type=SURFACE TO SURFACE</i> between trochanter surface elements and rigid surface consisting of <i>R3D3</i> -elements , no friction applied |
| <b>Model 3</b><br>(Figure 3.7) | see Model 1  | see Model 1  | contact modelled as <i>*CONTACT PAIR , type=SURFACE TO SURFACE</i> between trochanter surface elements and rigid surface consisting of <i>R3D3</i> elements ; <i>Friction=0.1</i> |
| <b>Model 4</b><br>(Figure 3.7) | see Model 1  | contact modelled as <i>*CONTACT PAIR , type=SURFACE TO SURFACE</i> between head surface elements and rigid surface consisting of <i>R3D3</i> -elements, <i>NO Friction</i> applied | see Model 2   |

|                              | <b>Epoxy pot</b>  | <b>Femoral head</b>   | <b>Trochanter</b> |
|------------------------------|---|---|-------------------|
| <b>Model 5</b> (Figure 3.8)  | Movement of the surface of the epoxy pot connected to movement of a node corresponding to the hinge of the jig by <i>*KINEMATIC COUPLING</i> , the node has one degree of freedom(rotation around y-axis) | see Model 1   | see Model 1       |
| <b>Model 6</b> (Figure 3.9)  | see Model 5   | see Model 2   | see Model 2       |
| <b>Model 7</b> (Figure 3.10) | see Model 5   | see Model 4   | see Model 4       |
| <b>Model 8</b> (Figure 3.10) | see Model 5   | contact modelled as <i>*CONTACT PAIR</i> , <i>type=SURFACE TO SURFACE</i> between head surface elements and rigid surface consisting of <i>R3D3</i> -elements, <i>Friction = 0.65</i> applied | see Model 4       |

**Table 3.4:** FE-models with different boundary conditions at the different sites

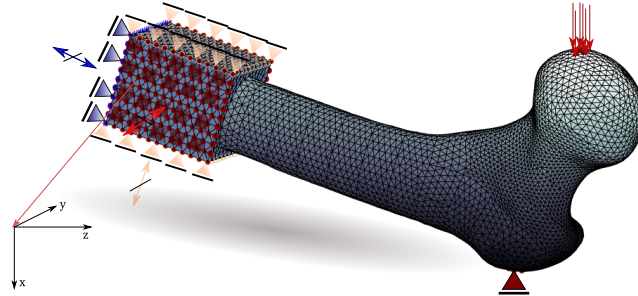


**Figure 3.5: Boundary conditions - Model 1:** Epoxy surface constrained perpendicular to surface, load of 1120 N / 4000 N applied directly on femoral head, contact point constrained in x-direction

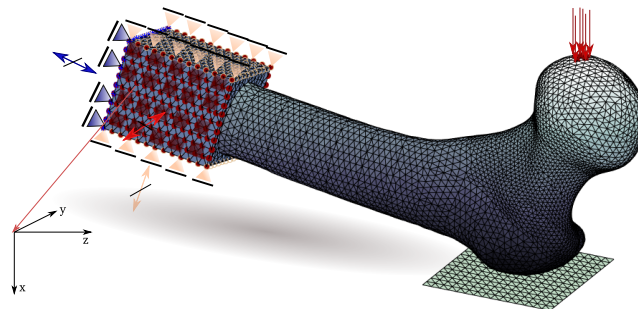


**Figure 3.6: Boundary conditions - Model 2 and 3:** Epoxy surface constrained perpendicular to surface, load of 1120 N / 4000 N applied directly on femoral head, contact at trochanter to rigid surface (composed of R3D3 elements) modelled frictionless and with friction of 0.1

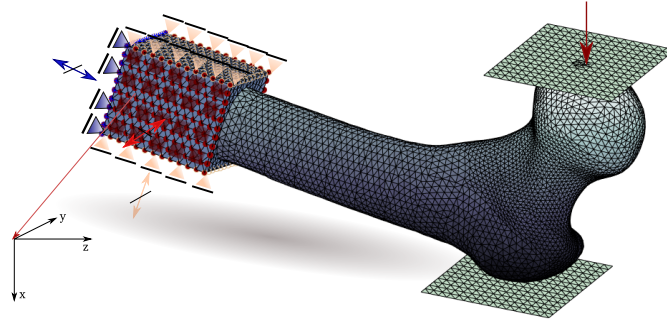


**Figure 3.7: Boundary conditions - Model 4:** Epoxy surface constrained perpendicular to surface, load of 1120 N / 4000 N applied on rigid surface on top of femoral head  $\rightarrow$  contact modelled frictionless, contact at trochanter to rigid surface (composed of R3D3 elements) modelled frictionless

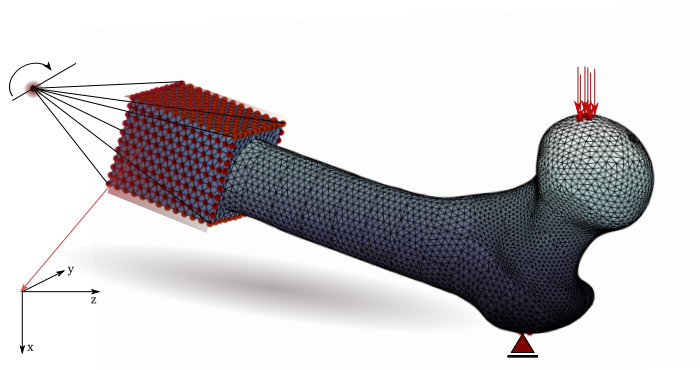


**Figure 3.8: Boundary conditions - Model 5:** Epoxy surface coupled to movement of reference node (degree of freedom: rotation around y-axis), load of 1120 N / 4000 N applied directly on femoral head, contact point constrained in x-direction

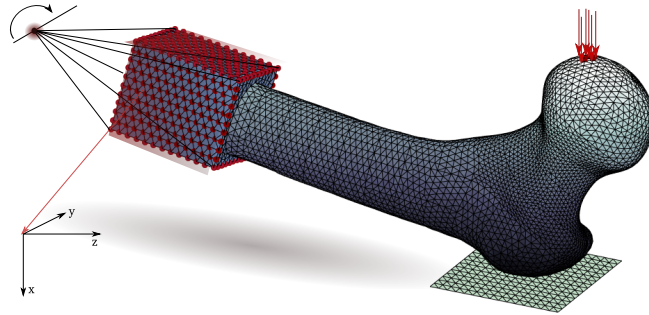


**Figure 3.9: Boundary conditions - Model 6:** Epoxy surface coupled to movement of reference node (degree of freedom: rotation around y-axis), load of 1120 N / 4000 N applied directly on femoral head, contact of trochanter to rigid surface (composed of R3D3 elements) modelled frictionless

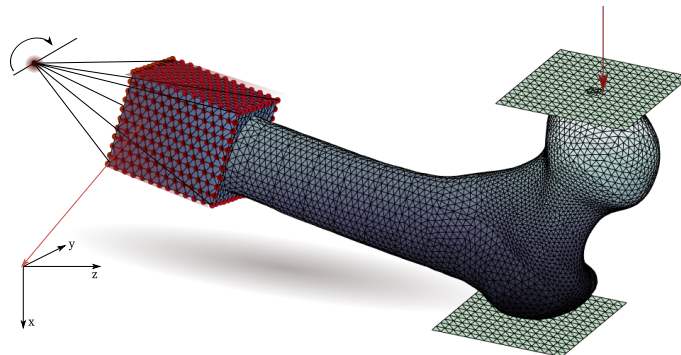


**Figure 3.10: Boundary conditions - Model 7 and 8:** Epoxy surface coupled to movement of reference node (degree of freedom: rotation around y-axis), load of 1120 N / 4000 N applied on rigid surface on top of femoral head → contact modelled frictionless, contact at trochanter to rigid surface (composed of R3D3 elements) modelled frictionless

## 3.4 Validation Process

FE-models were validated with principal strains measured during in vitro testing using DIC. FE data and DIC typically have different spatial resolution. Thus, a data comparison algorithm was developed in *Matlab*, based on existing scripts. The validation was performed for each composite bone at a load of 1120 N. At a load of 4000 N, femur 5 was excluded from the validation. A further overview of the validation procedure can be found in figure 3.11.

### 3.4.1 Preprocessing and Registration

According to the number of tests, five DIC data sets were compared to one FE-model. In order to validate the models with principal strains, every DIC-point cloud had to be registered on corresponding aspect of the FE-point cloud. For this purpose, the points on the outer surface of the FE-point cloud of the cortical component were extracted (figure 3.11(1)). Then, this new point cloud was cropped by excluding nodes of the lower part of the stem and of the epoxy pot. Since we were focusing on the head-neck part of the femur, nodes of other regions were not needed for the validation process (figure 3.11(2)). The DIC-point clouds were cropped to exclude outliers (figure 3.11(3)). Translation and rotation were applied to reposition them close to the final position (figure 3.11(4)(5)). Afterwards, the DIC-point cloud was registered on the FE-point cloud using a rigid iterative point (ICP) registration algorithm provided by *Matlab* (figure 3.11(6)). The point cloud of DIC was accurately registered over the FE-models, with an error less than 1.5 mm on the edges of the DIC-point cloud and close to zero in the central parts. DIC-point clouds of all five tests were registered on the FE-point cloud to pool the data of the five test and afterwards compare it to the principal strain of the FE-model.

DIC strain calculation is more accurate where cameras are in focus and on parts of the specimen with no or just slight curvature. Therefore, the appropriate DIC data was selected by cropping the point cloud and corresponding data again to a

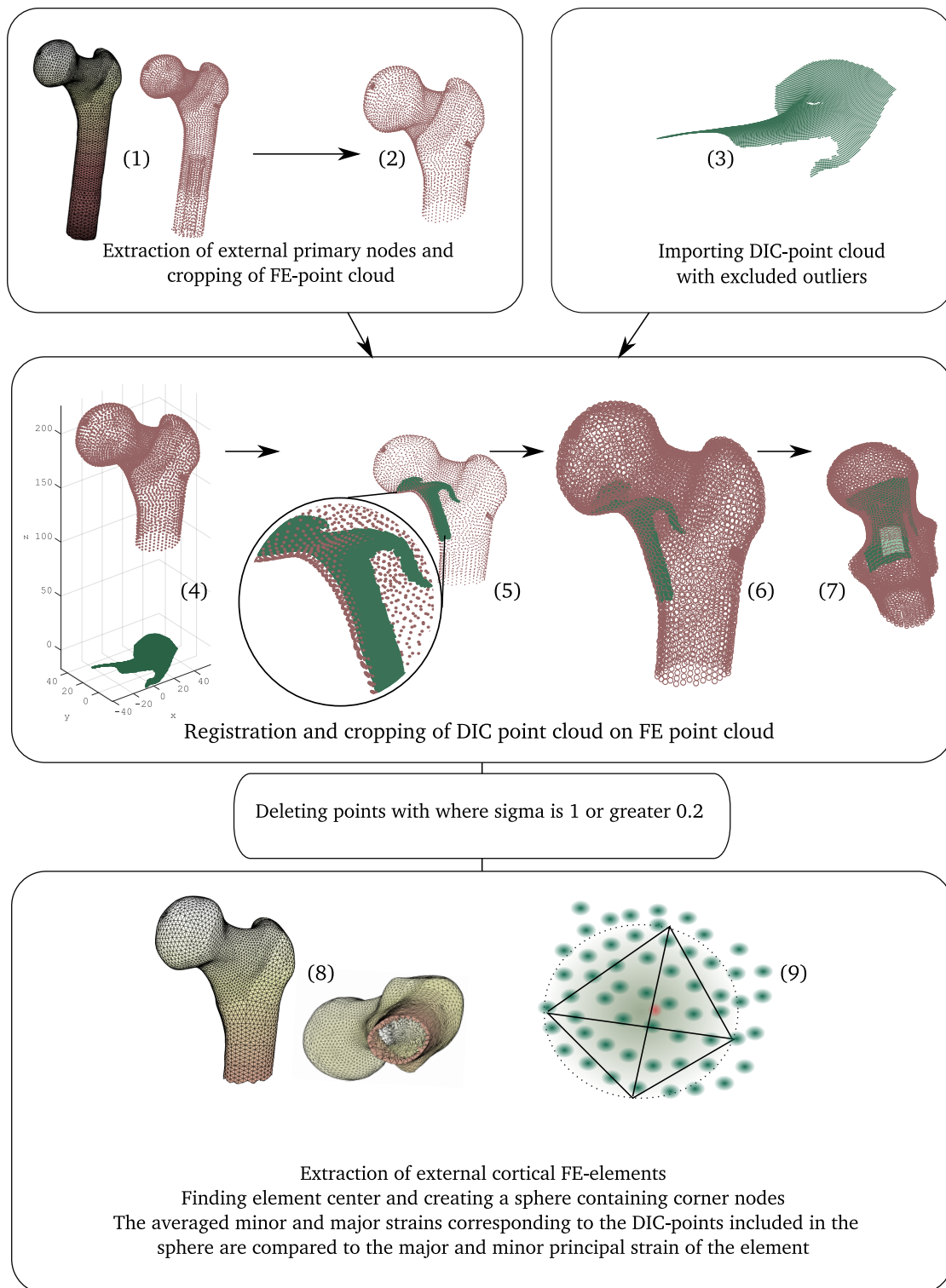


**Figure 3.11:** Validation procedure comparing minor and major principal strains of FE-models with data from DIC

rectangular stripe (see figure 3.11(7) and figure 3.12). Results for using the whole DIC-point cloud for validation can be found in the appendix.



**Figure 3.12:** Cropping were DIC was in focus, highest error excluded, approx. 1600 data points

### 3.4.2 Validation

The corresponding DIC-data to a load of 1120 N and 4000 N was selected. Measurement points where the confidence interval for the match at this point  $\sigma = -1$  or  $\sigma \geq 0.02$  were excluded according to the recommendations of the Vic3D 2007 software guidelines<sup>2</sup> (see section 3.2.2). External elements forming the surface of the femur were extracted by running a loop comparing node numbers of external cortical surface nodes and cortical elements. If all three corner nodes of one surface of a cortical element correspond to external nodes, then the element was assigned as external cortical element. In order to compare the different results for principal strains of DIC

<sup>2</sup> [www.correlatedsolutions.com/installs/Vic-3D-2010-manual.pdf](http://www.correlatedsolutions.com/installs/Vic-3D-2010-manual.pdf)

and FEA a sphere was created around each of the external cortical bone elements. The center and radius were calculated in a way that the surface of the sphere contains the three principal nodes of the elements. The major and minor principal strains of DIC-points within each sphere were averaged and compared to FE generated strains of the element (see figure 3.13).

A linear regression analysis was performed between the measured principal strains of the pooled DIC-data of the five tests and the principal strains computed by FE-analysis. Additionally, the data of the five bones was pooled and another linear regression analysis was performed.

Results of linear regression analysis of every single DIC-test at 1120 N compared to the corresponding FE-model cropped to a rectangular area where DIC was in focus ( $\sim 1600$  data points) can be found in the appendix. Note that at 1120 N each FE-model was compared to the data of 5 DIC-tests, whereas at 4000 N only one test was compared to the FE-model.

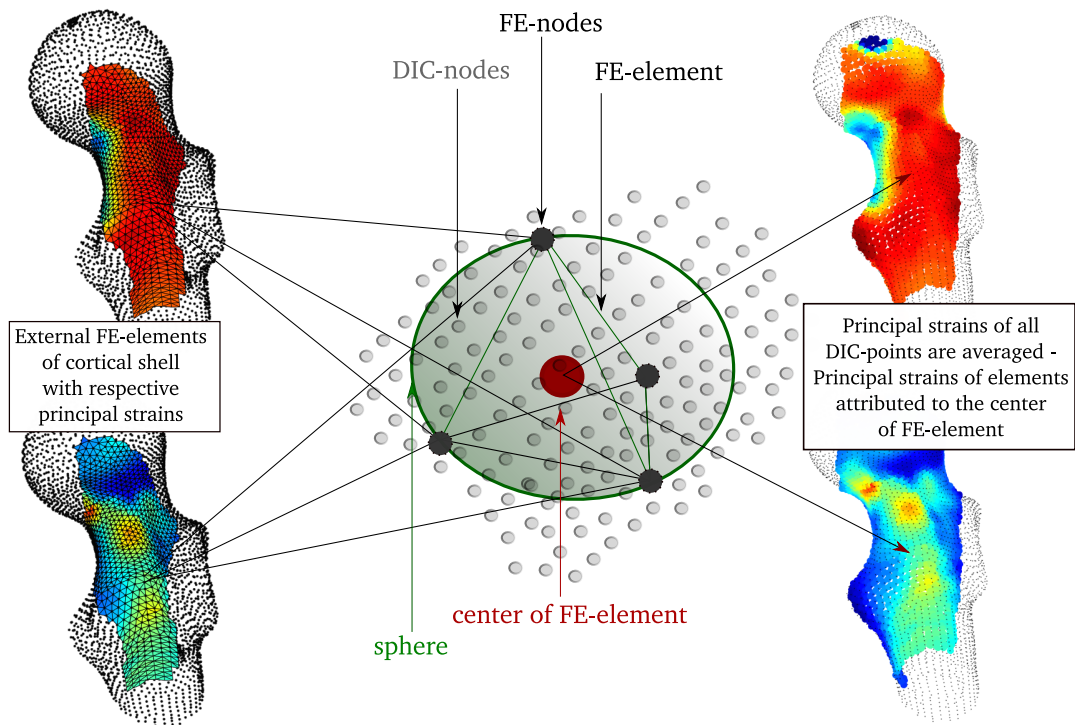


**Figure 3.13:** Comparison using principal strains: Building a sphere around the FE-elements and averaging strains

# Chapter 4

## Results

In the first section, the results of the comparison of DIC-point clouds and their associated data are presented. Data of femur 5 test 4 showed invalid data as it had not been loaded until the final load of 1120 N was achieved. Therefore, the data was excluded from the validation process. Additionally, results of inter-specimen repeatability investigations of pooled DIC-test data at 1120 N are presented. Second, we show the inter-specimen repeatability of FE-models of the 5 composite bones at 1120 N. Third, results of correlation between data from DIC and FEM are presented in areas of different size and with different loads applied. Finally, second and third are repeated with data obtained for applying a load of 4000 N, validating FE-models with one test per bone.

## 4.1 Repeatability test of DIC

### 4.1.1 Repeatability within every test set - point clouds, displacements and strains

The comparison of the DIC clouds concerning their form was performed by registering them on each other: we showed that within every test set (5 tests per specimen), every point cloud could be registered on the point cloud of test 3 with a distance of less than 0.05 mm, except on the far edges of the point clouds, where the greatest distance was 4 mm. Figure 4.1 shows the worst fitting clouds.

Strains and displacements of the other four tests were compared to test 3 at load level of 560 N and 1120 N:

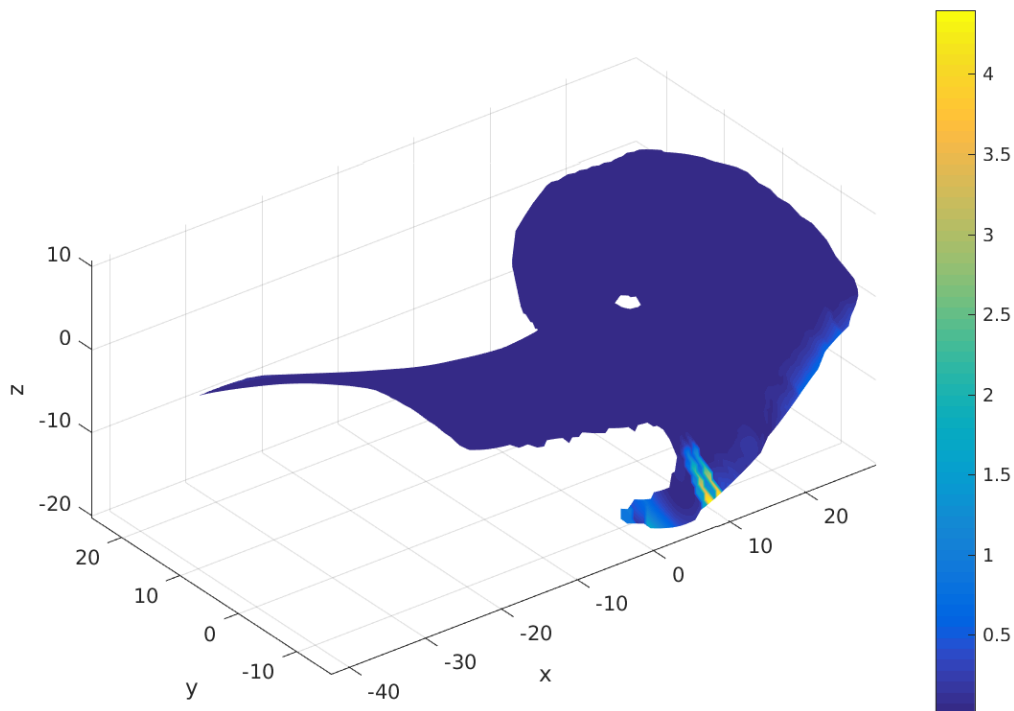


**Figure 4.1:** Distance between point clouds of specimen 1 (Test 2 on 3) in mm after registration: Specimen 1 showed the worst fit at the edges

### Absolute Displacement

Concerning displacements, the repeatability of DIC was good, except at the edges of the point clouds and the edges of the areas that could not be calculated due to reflection (figure 4.2 is representing the allocations of the highest displacement errors). With a load of 560 N the average slope of the linear regression line of single tests compared to test 3 was 1.030 (averaged standard deviation of slope was 0.170) and the averaged  $R^2$  was 0.842 (averaged standard deviation of  $R^2$  was 0.121). When 1120 N were applied, the average slope was 1.138 (averaged standard deviation of slope was 0.317) and the average  $R^2$  was 0.841 (averaged standard deviation of  $R^2$  was 0.111). For further information about the repeatability of displacement measurements within every single femur compared to test 3, see table 4.1, which provides the respective mean and standard deviation of slope and  $R^2$  (for data is also presented in the appendix, please refer to A.1 and A.3).

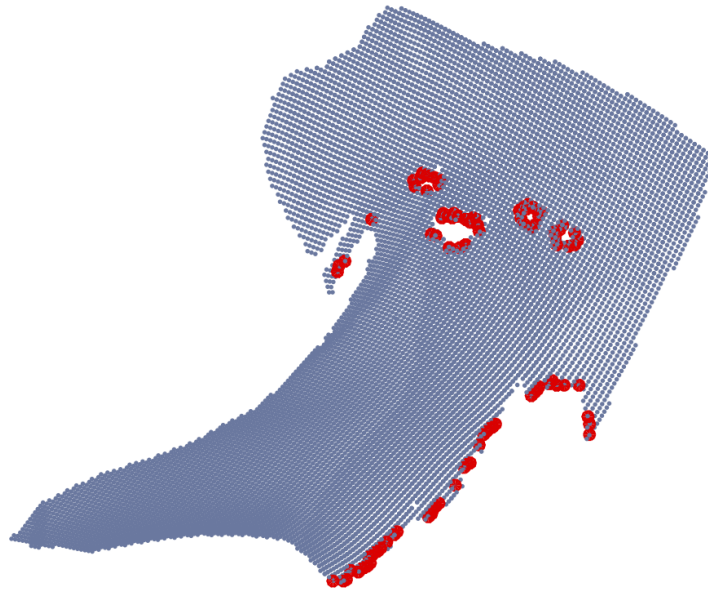


**Figure 4.2:** Nodes marked where the absolute ratio between absolute displacements was greater than 2 or smaller than 0.5 (here femur 2 test 4 compared to test 3 at a load of 1120 N)

|         | slope |       |        |       | $R^2$ |       |        |        |
|---------|-------|-------|--------|-------|-------|-------|--------|--------|
|         | 560 N |       | 1120 N |       | 560 N |       | 1120 N |        |
|         | mean  | std   | mean   | std   | mean  | std   | mean   | std    |
| Femur 1 | 1.063 | 0.128 | 1.159  | 0.326 | 0.918 | 0.033 | 0.914  | 0.026  |
| Femur 2 | 1.027 | 0.312 | 1.152  | 0.408 | 0.843 | 0.082 | 0.843  | 0.084  |
| Femur 3 | 1.067 | 0.122 | 1.157  | 0.298 | 0.690 | 0.443 | 0.668  | 0.403  |
| Femur 4 | 0.906 | 0.102 | 1.059  | 0.289 | 0.845 | 0.032 | 0.841  | 0.0272 |
| Femur 5 | 1.123 | 0.188 | 1.168  | 0.261 | 0.944 | 0.015 | 0.933  | 0.0170 |
| Average | 1.030 | 0.170 | 1.138  | 0.317 | 0.842 | 0.121 | 0.841  | 0.111  |

**Table 4.1:** Mean and standard deviation (std) of slope and  $R^2$  of displacements of test sets per femur compared to test 3

### Principal strains

Minor and major principal strains showed high noise with random errors over the whole measuring field in all the tests as can be seen in figure 4.3. Nodes were marked where the absolute ratio between principal minor and major strains of test 3 and other tests was greater than 2 or smaller than 0.5. While minor principal strains showed a completely random distribution of errors over the complete measuring field, major principal strains showed a small area with less or no noise (see figure 4.4) in all samples. It was decided to use an area according to this for validation of the FE-models later on.

For a general overview of the repeatability of strains, see also table 4.2, providing averaged slope and  $R^2$  within every test set compared to test 3 (for further information, refer to the appendix A.2 and A.4 ). With a load of 560 N the averaged slope of the linear regression line of single tests compared to test 3 was 0.711 (averaged standard deviation of slope was 0.080) and the averaged  $R^2$  was 0.591 (averaged standard deviation of  $R^2$  was 0.161). When 1120 N were applied, the average slope was 0.844 (averaged standard deviation of slope was 0.064) and the average  $R^2$  was 0.583 (averaged standard deviation of  $R^2$  was 0.108). The slope of the regression line was generally closer to one at a load of 1120 N than at 560 N.

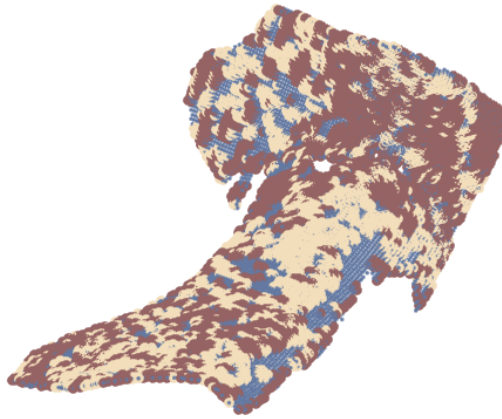


**Figure 4.3:** Nodes marked where the absolute ratio between principal minor and major strains of test 3 and others was greater than 2 or smaller than 0.5 - here femur 2 test 4 compared to test 3 at a load of 1120 N (beige: minor principal strains, brown: major principal strains)

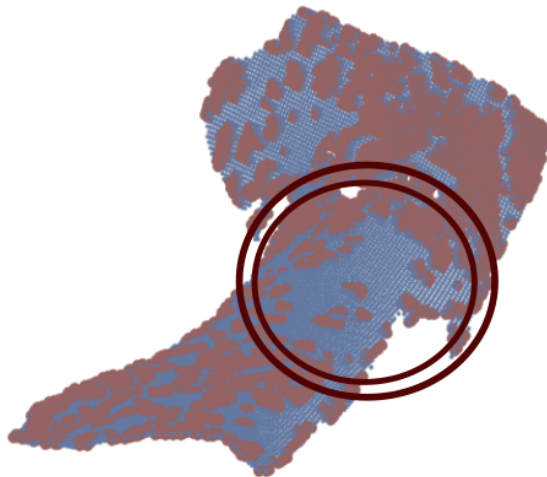


**Figure 4.4:** Major principal strains showing less error in a certain area, which was used for Validation of FE-models

|         | slope |       |        |       | $R^2$ |       |        |       |
|---------|-------|-------|--------|-------|-------|-------|--------|-------|
|         | 560 N |       | 1120 N |       | 560 N |       | 1120 N |       |
|         | mean  | std   | mean   | std   | mean  | std   | mean   | std   |
| Femur 1 | 0.694 | 0.039 | 0.873  | 0.060 | 0.591 | 0.107 | 0.557  | 0.089 |
| Femur 2 | 0.652 | 0.111 | 0.805  | 0.072 | 0.593 | 0.212 | 0.553  | 0.150 |
| Femur 3 | 0.802 | 0.067 | 0.873  | 0.024 | 0.623 | 0.200 | 0.638  | 0.091 |
| Femur 4 | 0.649 | 0.058 | 0.876  | 0.080 | 0.565 | 0.137 | 0.640  | 0.078 |
| Femur 5 | 0.771 | 0.125 | 0.775  | 0.083 | 0.577 | 0.148 | 0.509  | 0.132 |
| Average | 0.711 | 0.080 | 0.844  | 0.064 | 0.591 | 0.161 | 0.583  | 0.108 |

**Table 4.2:** Mean and standard deviation (std) of slope and  $R^2$  of minor and major principal strains of test sets per femur compared to test 3

### 4.1.2 Inter-specimens repeatability of DIC

Additionally, the inter-specimen repeatability was tested at a load of 1120 N in the area that was used for validation in the following section. We used composite bones which are supposed to show similar mechanical behaviour. Values of minor and major principal microstrains were plotted for each bone respectively (see figure 4.5 and figure 4.6) and mean and standard deviation of minor and major principal strains were calculated as can be seen in table 4.3 and in table 4.4. The values of principal strains did not show significant outliers concerning their mean and standard deviation, only femur 1 and 4 showed high maximum errors in major principal strains. Repeatability was also tested with respect to femur 1 and we obtained an averaged slope of 0.820 and an averaged  $R^2$  of 0.745. Slope and  $R^2$  of the single specimen compared to specimen 1 are presented in table 4.5. The plot of the comparison of strains of specimen 2 to 5 compared to specimen 1 is shown in figure 4.7.

The plots that were used for qualitative comparison of minor and major principal strains between the specimen can be seen in figure 4.8 and figure 4.9. In the region of our interest principal strain basically show the same pattern, but specimen 4 and 5 show diverging behaviour in the upper part of the point cloud close to the head-neck junction.

|         | Mean [ $\mu\epsilon$ ] | Standard Deviation [ $\mu\epsilon$ ] |
|---------|------------------------|--------------------------------------|
| Femur 1 | -394                   | 169                                  |
| Femur 2 | -436                   | 203                                  |
| Femur 3 | -368                   | 169                                  |
| Femur 4 | -534                   | 201                                  |
| Femur 5 | -307                   | 180                                  |
| Average | -408                   | 185                                  |

**Table 4.3:** Mean and standard deviation of minor principal microstrains in each femur

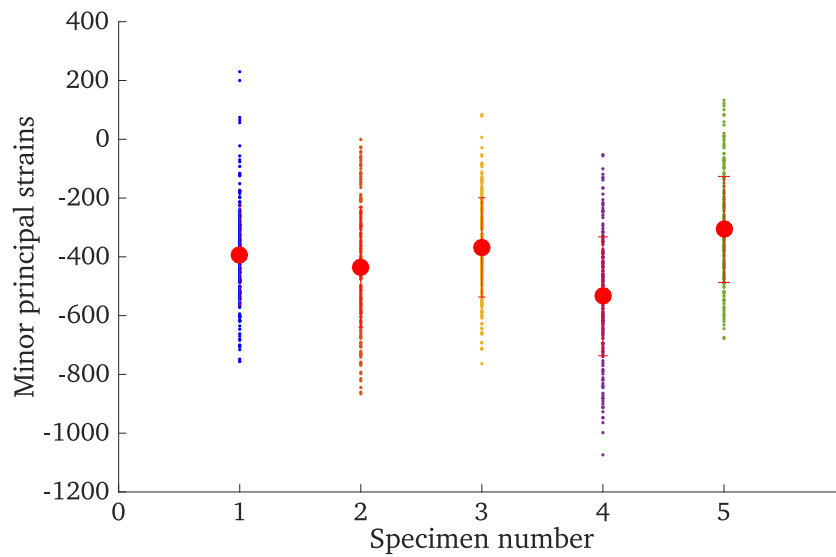


**Figure 4.5:** Minor principal strains ( [ $\mu\epsilon$ ]) in every specimen, mean and standard deviation(std)

|         | Mean [ $\mu\epsilon$ ] | Standard Deviation [ $\mu\epsilon$ ] |
|---------|------------------------|--------------------------------------|
| Femur 1 | 806                    | 361                                  |
| Femur 2 | 700                    | 247                                  |
| Femur 3 | 666                    | 247                                  |
| Femur 4 | 890                    | 388                                  |
| Femur 5 | 717                    | 249                                  |
| Average | 756                    | 298                                  |

**Table 4.4:** Mean and standard deviation of major principal microstrains in each femur

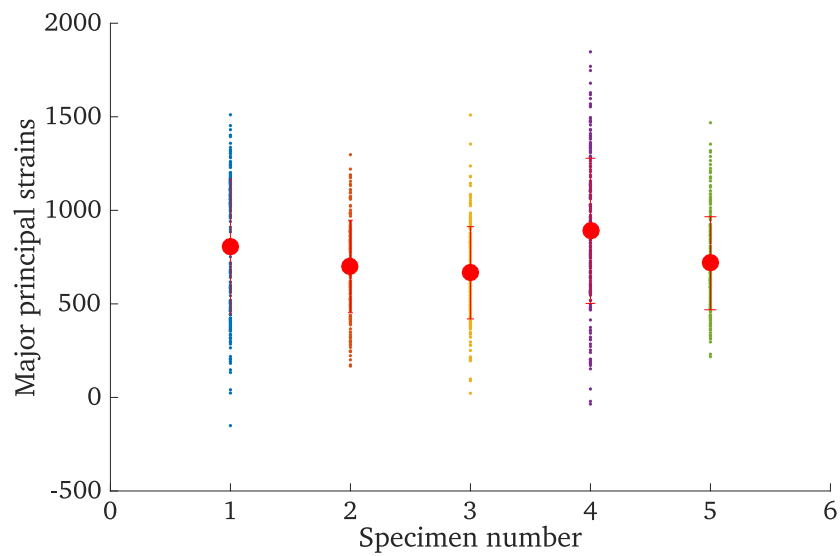


**Figure 4.6:** Major principal strains ( [ $\mu\epsilon$ ]) in every specimen, mean and standard deviation

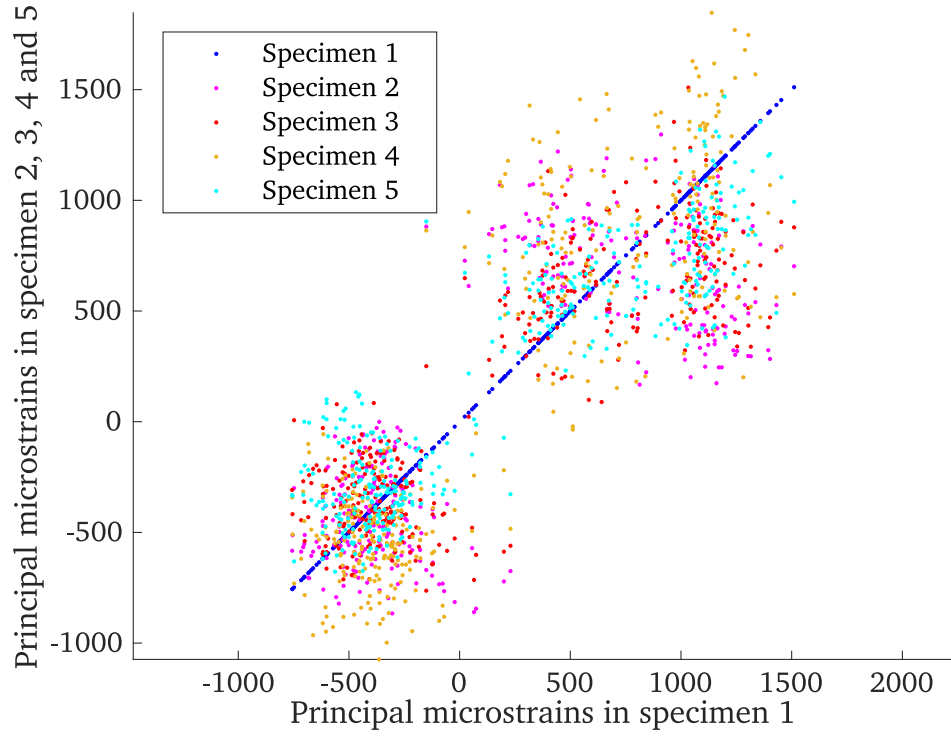


**Figure 4.7:** Principal strains ( $[\mu\varepsilon]$ ) in all specimens compared to femur 1

|       | Femur 1 | Femur 2 | Femur 3 | Femur 4 | Femur 5 | Average |
|-------|---------|---------|---------|---------|---------|---------|
| Slope | 1.000   | 0.737   | 0.742   | 1.031   | 0.769   | 0.820   |
| $R^2$ | 1.000   | 0.637   | 0.773   | 0.753   | 0.818   | 0.745   |

**Table 4.5:** Inter-specimen repeatability of DIC: Principal strains compared to Specimen 1

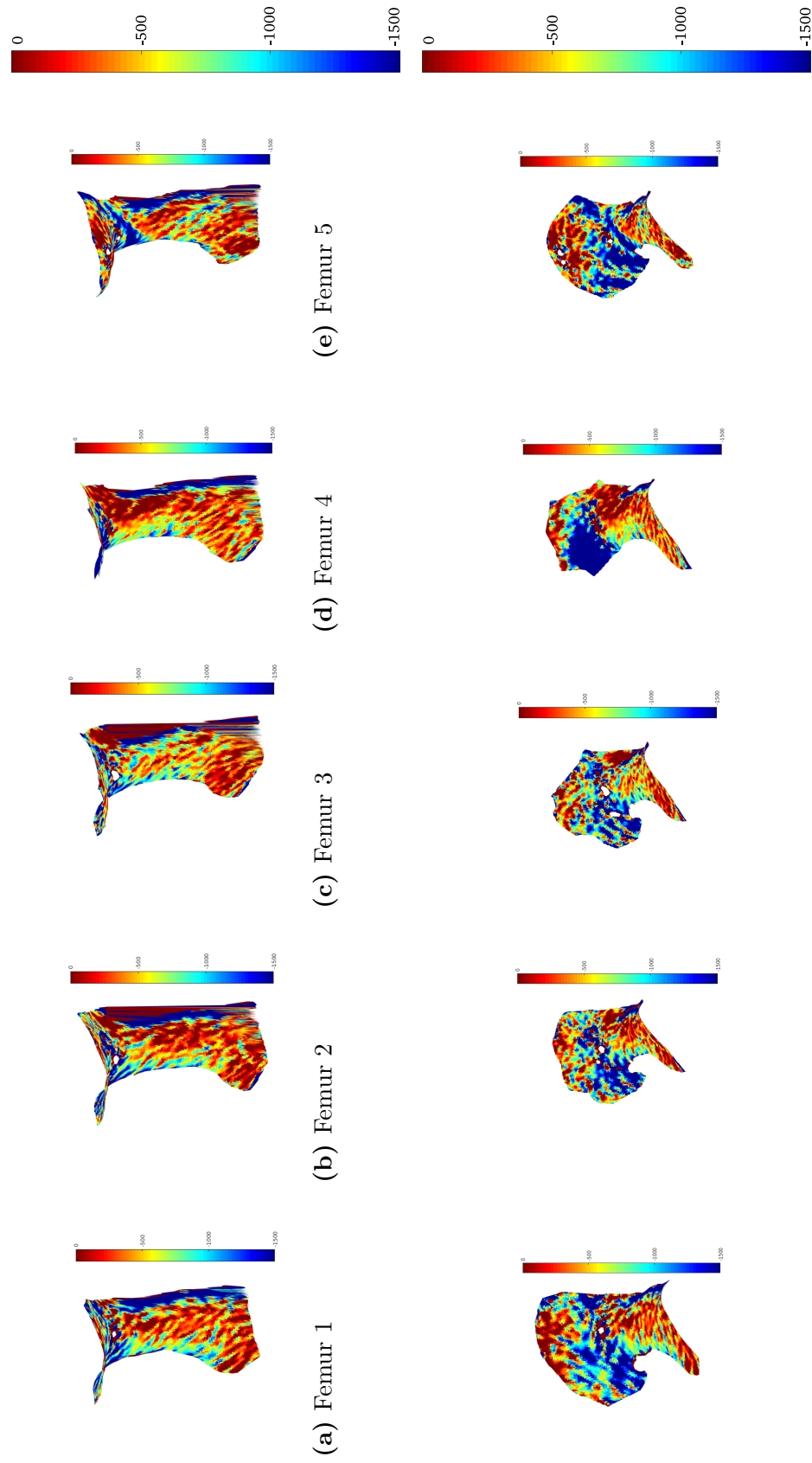


Figure 4.8: Minor principal strains  $[\mu\epsilon]$  obtained from DIC from two different perspectives

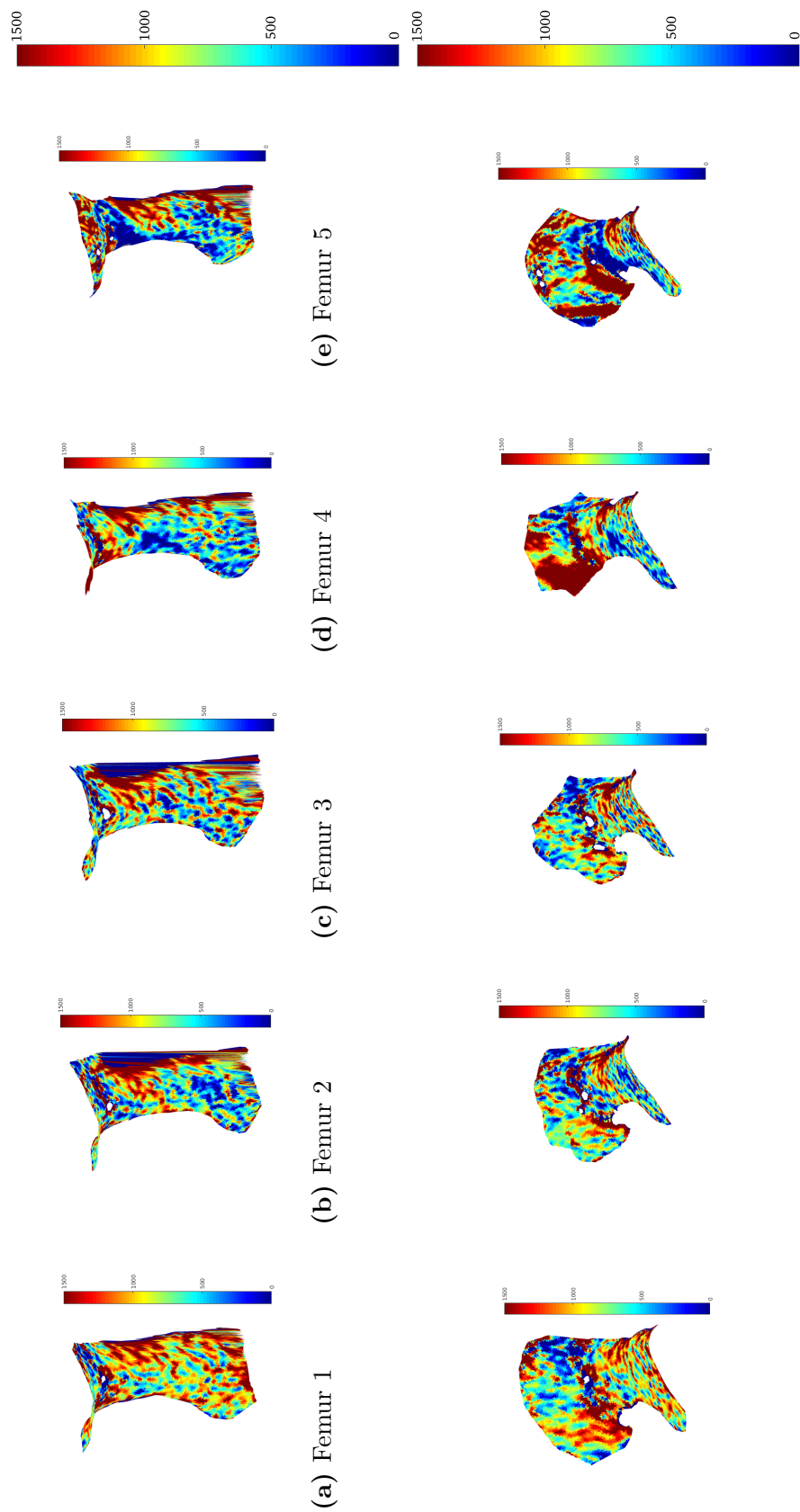


Figure 4.9: Major principal strains  $[\mu\epsilon]$  obtained from DIC from two different perspectives

## 4.2 Validation of FE-models at 1120 N

### 4.2.1 Inter-specimen repeatability of FE-models

FE-models were qualitatively compared to each other and showed good repeatability concerning principal strains between the different specimen. Table 4.6 and table 4.7 show mean and standard deviation of minor and major principal strains at a load of 1120 N in the elements located on the surface of the lateral femoral neck, which was validated by DIC measurements. The inter-specimen repeatability was also compared qualitatively and showed similar strain patterns. An example of model 4, which showed the best correlation with DIC-data after validation, can be seen in figure 4.11. For results of all models, please refer to the appendix B.

|         | Femur 1 | Femur 2 | Femur 3 | Femur 4 | Femur 5 | Femur 1 | Femur 2 | Femur 3 | Femur 4 | Femur 5 |
|---------|---------|---------|---------|---------|---------|---------|---------|---------|---------|---------|
|         | mean    |         |         |         |         | std     |         |         |         |         |
| Model 1 | -389    | -321    | -310    | -364    | -405    | 282     | 201     | 189     | 235     | 310     |
| Model 2 | -395    | -336    | -312    | -361    | -409    | 283     | 206     | 190     | 236     | 310     |
| Model 3 | -394    | -336    | -312    | -360    | -408    | 280     | 204     | 188     | 234     | 307     |
| Model 4 | -367    | -314    | -321    | -390    | -412    | 258     | 189     | 189     | 255     | 310     |
| Model 5 | -389    | -322    | -312    | -364    | -405    | 283     | 202     | 189     | 235     | 310     |
| Model 6 | -395    | -337    | -312    | -360    | -409    | 283     | 207     | 190     | 235     | 309     |
| Model 7 | -367    | -315    | -322    | -389    | -411    | 258     | 190     | 188     | 254     | 310     |
| Model 8 | -387    | -364    | -365    | -357    | -382    | 274     | 257     | 275     | 277     | 287     |

**Table 4.6:** Mean and standard deviation (std) of minor principal strains  $[\mu\epsilon]$  in FE-models in the lateral femoral neck region

|         | Femur 1 | Femur 2 | Femur 3 | Femur 4 | Femur 5 | Femur 1 | Femur 2 | Femur 3 | Femur 4 | Femur 5 |
|---------|---------|---------|---------|---------|---------|---------|---------|---------|---------|---------|
|         | mean    |         |         |         |         | std     |         |         |         |         |
| Model 1 | 540     | 502     | 479     | 433     | 523     | 209     | 190     | 177     | 167     | 180     |
| Model 2 | 556     | 529     | 488     | 442     | 546     | 215     | 201     | 181     | 171     | 186     |
| Model 3 | 551     | 525     | 484     | 437     | 540     | 214     | 201     | 180     | 169     | 185     |
| Model 4 | 548     | 473     | 549     | 482     | 557     | 210     | 170     | 209     | 191     | 190     |
| Model 5 | 550     | 515     | 495     | 435     | 534     | 212     | 194     | 183     | 168     | 182     |
| Model 6 | 559     | 537     | 489     | 432     | 538     | 216     | 205     | 182     | 167     | 184     |
| Model 7 | 553     | 478     | 555     | 474     | 549     | 212     | 172     | 211     | 187     | 187     |
| Model 8 | 228     | 220     | 215     | 192     | 218     | 160     | 155     | 162     | 143     | 154     |

**Table 4.7:** Mean and standard deviation(std) of major principal strains  $[\mu\epsilon]$  in FE-models in the lateral femoral neck region

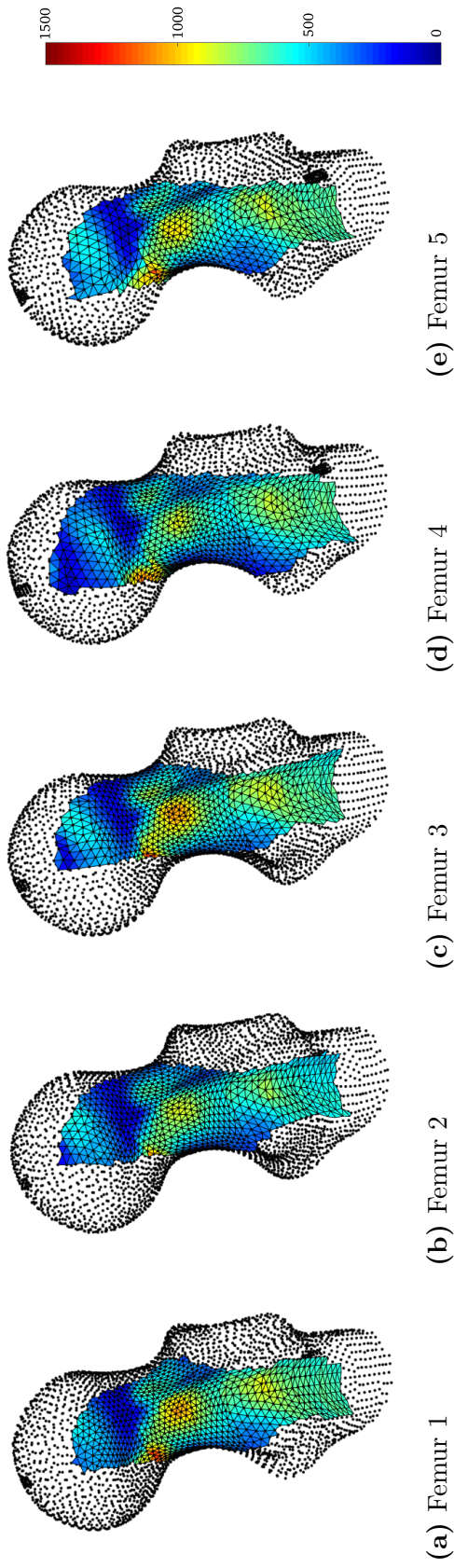


**Figure 4.10:** Major principal strains  $[\mu\epsilon]$  in external elements in Model 7

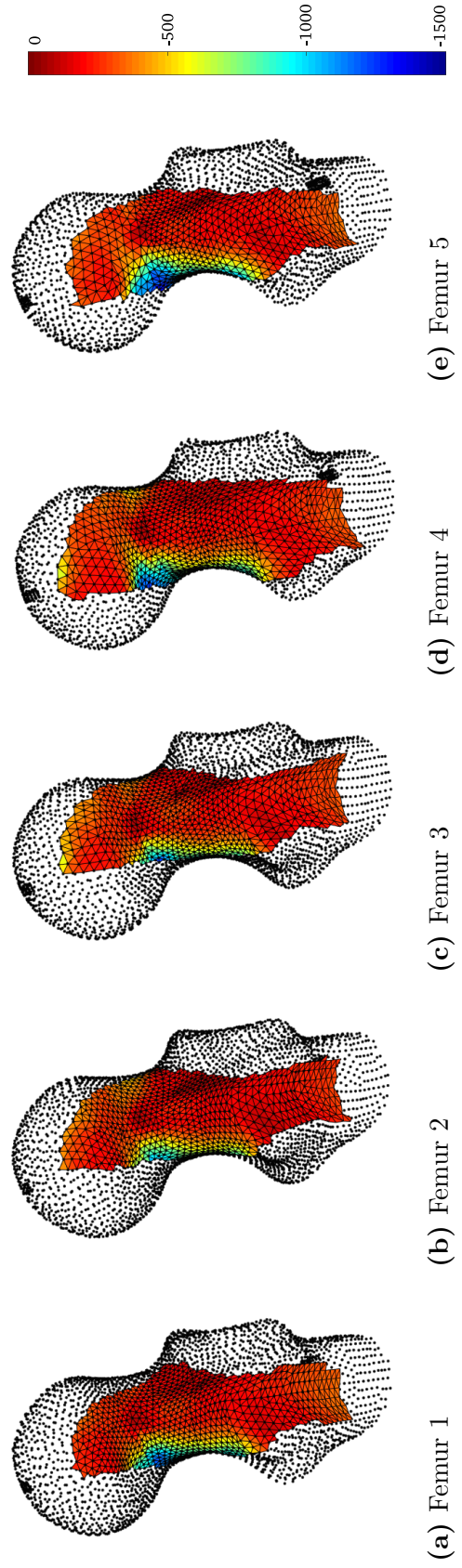


**Figure 4.11:** Minor principal strains  $[\mu\epsilon]$  in external elements in Model 7

## 4.2.2 Validation of FE-models against DIC-measurements

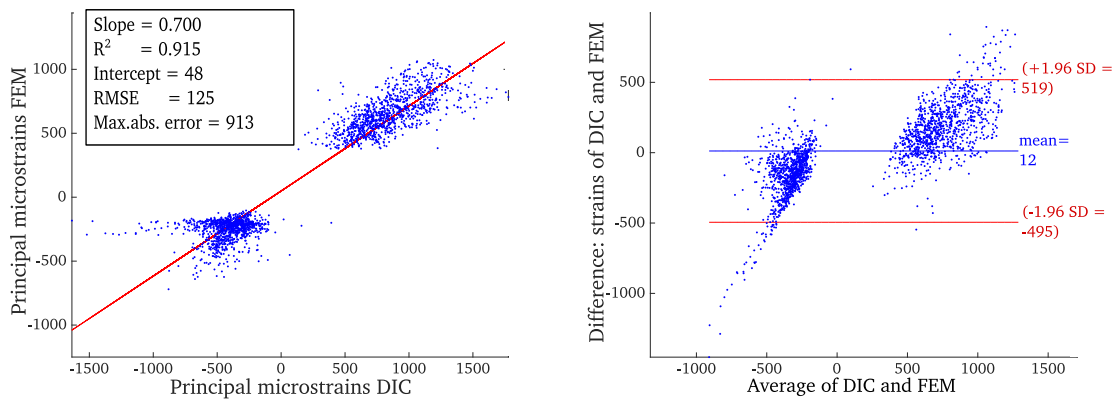


**Figure 4.12:** Light green: cropped section where data was validated (about 1600 data points)

The area in which the validation was performed can be seen in figure 4.12. When data of all five femurs was pooled we obtained a slope of 0.70 and a coefficient of determination of 0.92 in the model with the best correlation, which was model 4. A scatter plot and Bland-Altman plot of model 4 are provided in figure 4.13a and figure 4.13b. Table 4.8 contains slope,  $R^2$ , intercept, root mean square error (RMSE) and maximum absolute error of all models when data of all five femurs was pooled. Results obtained for each bone and model respectively can be found in the following tables (slope: table 4.9 ;  $R^2$ : table 4.10 ; Intercept: table 4.11 ; RMSE: table 4.12 ; maximum absolute error: table 4.13).

| -       | Slope | $R^2$ | Intercept [ $\mu\epsilon$ ] | RMSE [ $\mu\epsilon$ ] | Max. abs. error [ $\mu\epsilon$ ] |
|---------|-------|-------|-----------------------------|------------------------|-----------------------------------|
| Model 1 | 0.671 | 0.903 | 41                          | 133                    | 894                               |
| Model 2 | 0.691 | 0.902 | 46                          | 138                    | 921                               |
| Model 3 | 0.684 | 0.901 | 42                          | 138                    | 915                               |
| Model 4 | 0.700 | 0.915 | 48                          | 125                    | 913                               |
| Model 5 | 0.681 | 0.904 | 45                          | 134                    | 906                               |
| Model 6 | 0.690 | 0.900 | 45                          | 140                    | 922                               |
| Model 7 | 0.699 | 0.914 | 48                          | 127                    | 914                               |
| Model 8 | 0.214 | 0.771 | -41                         | 66                     | 467                               |

**Table 4.8:** Data of all five femurs pooled



**(a)** Scatter plot for five composite bones at 1120 N **(b)** Bland-Altman plot for five composite bones at 1120 N

**Figure 4.13:** Model with the best correlation: Model 4

|         | Femur 1 | Femur 2 | Femur 3 | Femur 4 | Femur 5 |
|---------|---------|---------|---------|---------|---------|
| Model 1 | 0.820   | 0.737   | 0.635   | 0.533   | 0.627   |
| Model 2 | 0.839   | 0.778   | 0.645   | 0.536   | 0.649   |
| Model 3 | 0.833   | 0.771   | 0.639   | 0.527   | 0.641   |
| Model 4 | 0.804   | 0.687   | 0.717   | 0.597   | 0.665   |
| Model 5 | 0.826   | 0.747   | 0.647   | 0.535   | 0.635   |
| Model 6 | 0.841   | 0.783   | 0.646   | 0.525   | 0.643   |
| Model 7 | 0.808   | 0.690   | 0.722   | 0.588   | 0.659   |
| Model 8 | 0.269   | 0.250   | 0.224   | 0.153   | 0.208   |

**Table 4.9:** Slope - Validation with approx. 1600 points in every DIC-point cloud

|         | Femur 1 | Femur 2 | Femur 3 | Femur 4 | Femur 5 |
|---------|---------|---------|---------|---------|---------|
| Model 1 | 0.902   | 0.944   | 0.937   | 0.907   | 0.913   |
| Model 2 | 0.904   | 0.947   | 0.937   | 0.907   | 0.915   |
| Model 3 | 0.903   | 0.946   | 0.937   | 0.907   | 0.914   |
| Model 4 | 0.908   | 0.945   | 0.939   | 0.904   | 0.915   |
| Model 5 | 0.903   | 0.945   | 0.938   | 0.907   | 0.915   |
| Model 6 | 0.904   | 0.947   | 0.937   | 0.908   | 0.915   |
| Model 7 | 0.909   | 0.945   | 0.939   | 0.905   | 0.914   |
| Model 8 | 0.761   | 0.782   | 0.834   | 0.876   | 0.792   |

**Table 4.10:**  $R^2$  - Validation with approx. 1600 points in every DIC-point cloud

|         | Femur 1 | Femur 2 | Femur 3 | Femur 4 | Femur 5 |
|---------|---------|---------|---------|---------|---------|
| Model 1 | 15      | 55      | 41      | 40      | 37      |
| Model 2 | 17      | 57      | 43      | 48      | 44      |
| Model 3 | 13      | 54      | 40      | 44      | 40      |
| Model 4 | 34      | 54      | 56      | 43      | 43      |
| Model 5 | 19      | 59      | 47      | 41      | 41      |
| Model 6 | 18      | 60      | 44      | 42      | 41      |
| Model 7 | 35      | 55      | 58      | 37      | 40      |
| Model 8 | -68     | -44     | -43     | -31     | -42     |

**Table 4.11:** Intercept  $[\mu\varepsilon]$  - Validation with approx. 1600 points

|         | Femur 1 | Femur 2 | Femur 3 | Femur 4 | Femur 5 |
|---------|---------|---------|---------|---------|---------|
| Model 1 | 122     | 109     | 100     | 110     | 131     |
| Model 2 | 122     | 113     | 102     | 111     | 134     |
| Model 3 | 122     | 113     | 101     | 108     | 133     |
| Model 4 | 114     | 101     | 111     | 126     | 137     |
| Model 5 | 122     | 110     | 102     | 111     | 131     |
| Model 6 | 122     | 114     | 102     | 108     | 133     |
| Model 7 | 114     | 101     | 112     | 123     | 136     |
| Model 8 | 80      | 68      | 57      | 38      | 60      |

**Table 4.12:** RMSE  $[\mu\varepsilon]$  - Validation with approx. 1600 points

|         | Femur 1 | Femur 2 | Femur 3 | Femur 4 | Femur 5 |
|---------|---------|---------|---------|---------|---------|
| Model 1 | 1005    | 489     | 594     | 668     | 370     |
| Model 2 | 1028    | 516     | 602     | 665     | 381     |
| Model 3 | 1024    | 515     | 599     | 655     | 379     |
| Model 4 | 965     | 461     | 646     | 750     | 390     |
| Model 5 | 1009    | 491     | 599     | 670     | 373     |
| Model 6 | 1031    | 517     | 602     | 656     | 379     |
| Model 7 | 969     | 462     | 649     | 743     | 388     |
| Model 8 | 392     | 458     | 288     | 201     | 302     |

**Table 4.13:** Maximum absolute error  $[\mu\varepsilon]$  - Validation with approx. 1600 points

### 4.3 Validation of FE-models at 4000 N

Validation was performed with models 1 to 6 with 4 femurs and one test in a sideways fall loading condition at 4000 N.

#### 4.3.1 Inter-specimen repeatability of FE-models

The repeatability between the different specimen was qualitatively assessed by plotting center points of the elements in a color representing the value of major and minor strains obtained from FE-analysis. Repeatability was primarily checked in the area of interest at the lateral femoral neck. The repeatability between the composite bones at this site was good, as can be seen in figure 4.14 for Model 6, showing the best slope of the regression line with DIC-measurements in the validation, but femur 4 showed a noticeable anomaly in the distribution of minor and major principal strains in the head region (figure 4.14d and 4.14h).

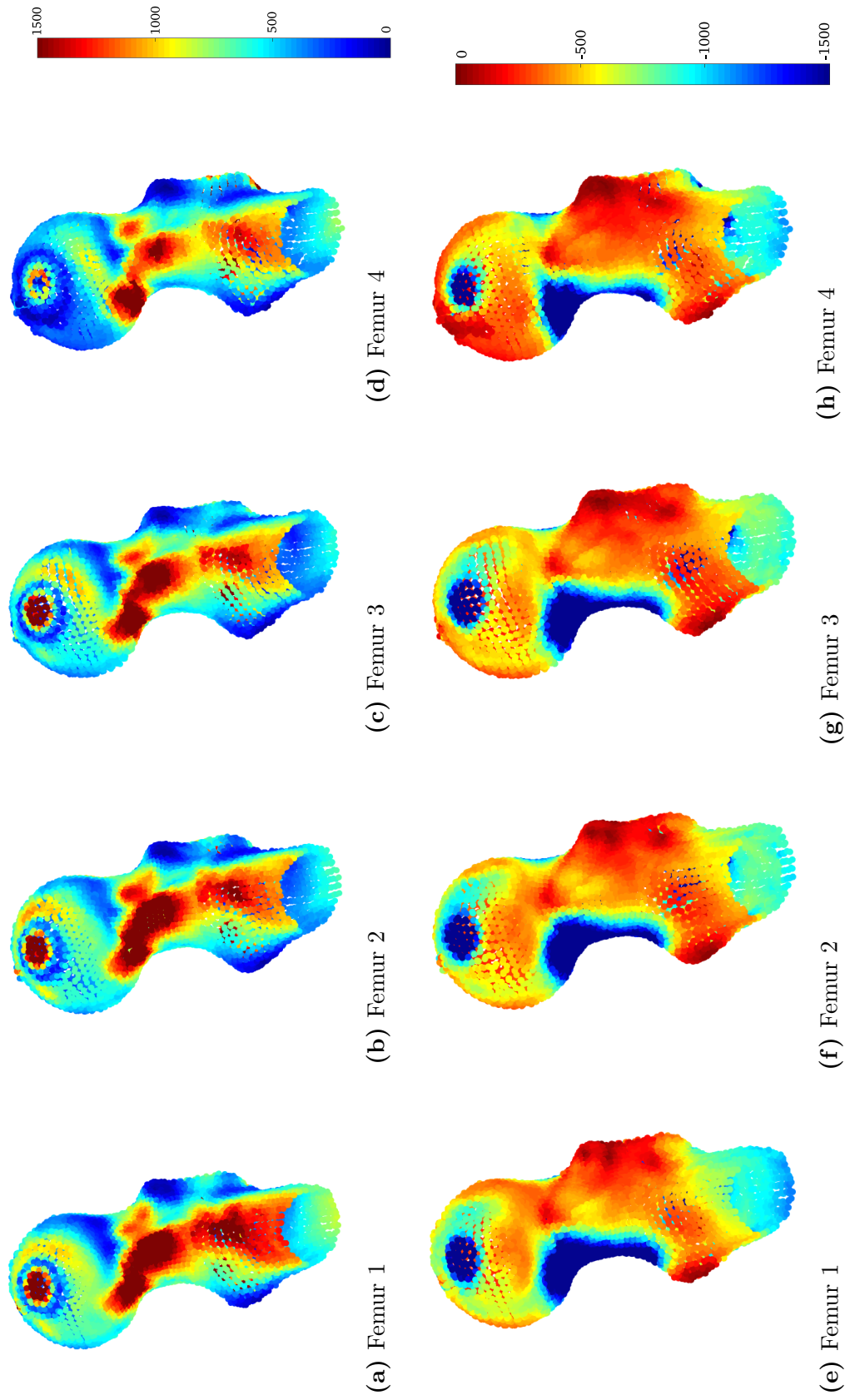
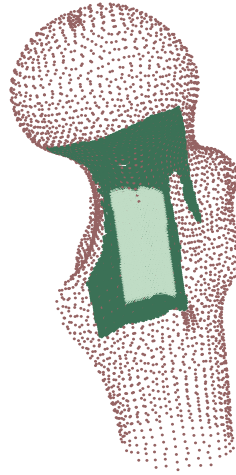


Figure 4.14: Repeatability test of FE-models in model 1: major principal strains (top) and minor principal strains (bottom)

### 4.3.2 Validation of FE-models against DIC-measurements



**Figure 4.15:** Cropped section where data was validated (about 1600 data points)

The area in which the validation was performed can be seen in figure 4.15.

The FE-model showing a slope closest to 1 ( $slope = 0.75$ ) when data of all five bones was pooled was model 6. The coefficient of determination was 0.773. A scatter plot and Bland-Altman plot of model 6 are provided in figure 4.16a and figure 4.16b. Table 4.14 contains slope,  $R^2$ , intercept, root mean square error (RMSE) and maximum absolute error of all models when data of all five femurs was pooled. Results obtained for each bone and model respectively can be found in the following tables (slope: table 4.15 ;  $R^2$ : table 4.16 ; Intercept: table 4.17 ; RMSE: table 4.18 ; maximum absolute error: table 4.19). Scatter plots of each bone respectively of model 6 are shown in figure 4.17a, figure 4.17b, figure 4.17c and figure 4.17d. Figure 4.17c and figure 4.17d illustrate that DIC measurements show high errors within some data points in specimen 3 and 4 at 4000 N. When these two specimen were removed from validation, a slope of 0.797 and a  $R^2$  of 0.9656 were obtained for model 6. Table 4.20 contains slope,  $R^2$ , intercept, root mean square error (RMSE) and maximum absolute error of all models when data of specimen 1 and 2 was pooled. Figure 4.18a and

figure 4.18b show scatter plot and Bland-Altman plot of model 6 when specimen 3 and 4 were excluded.

|         | Slope | $R^2$ | Intercept [ $\mu\epsilon$ ] | RMSE [ $\mu\epsilon$ ] | Maximum absolute error [ $\mu\epsilon$ ] |
|---------|-------|-------|-----------------------------|------------------------|--|
| Model 1 | 0.723 | 0.782 | 89                          | 398                    | 19213                                    |
| Model 2 | 0.717 | 0.775 | 90                          | 438                    | 19089                                    |
| Model 3 | 0.736 | 0.772 | 99                          | 388                    | 19604                                    |
| Model 4 | 0.721 | 0.824 | 143                         | 353                    | 19116                                    |
| Model 5 | 0.744 | 0.777 | 127                         | 383                    | 19758                                    |
| Model 6 | 0.750 | 0.773 | 120                         | 399                    | 19977                                    |

**Table 4.14:** Pooled data of four femurs per model

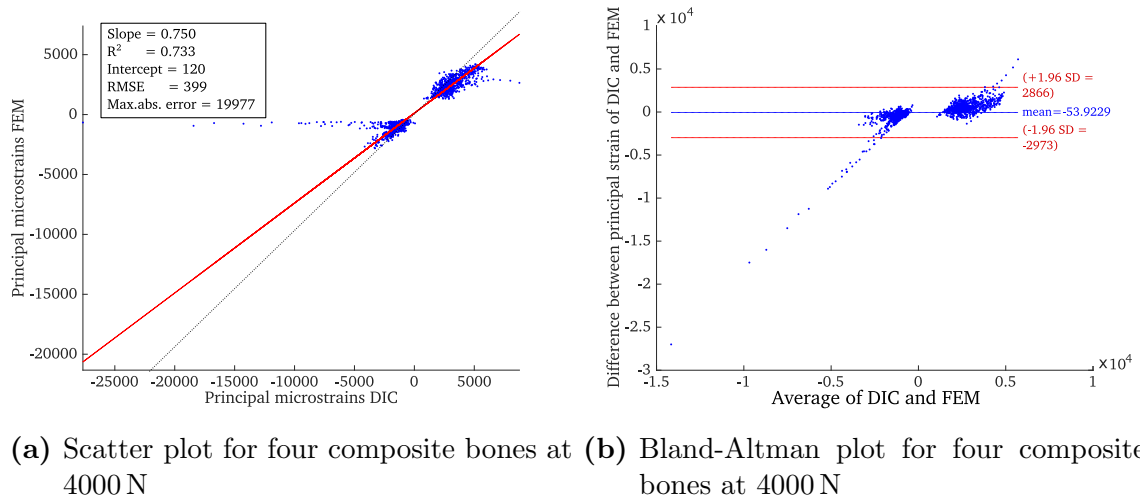


**Figure 4.16:** Model 6 - model with best slope

|         | Femur 1 | Femur 2 | Femur 3 | Femur 4 |
|---------|---------|---------|---------|---------|
| Model 1 | 0.794   | 0.743   | 0.735   | 0.658   |
| Model 2 | 0.803   | 0.779   | 0.740   | 0.642   |
| Model 3 | 0.792   | 0.767   | 0.728   | 0.632   |
| Model 4 | 0.753   | 0.718   | 0.750   | 0.667   |
| Model 5 | 0.799   | 0.754   | 0.747   | 0.658   |
| Model 6 | 0.806   | 0.787   | 0.744   | 0.637   |

**Table 4.15:** Slope - Validation with approximately 1600 data points

|         | Femur 1 | Femur 2 | Femur 3 | Femur 4 |
|---------|---------|---------|---------|---------|
| Model 1 | 0.954   | 0.979   | 0.701   | 0.583   |
| Model 2 | 0.954   | 0.978   | 0.699   | 0.583   |
| Model 3 | 0.954   | 0.978   | 0.699   | 0.583   |
| Model 4 | 0.957   | 0.978   | 0.831   | 0.581   |
| Model 5 | 0.954   | 0.978   | 0.705   | 0.583   |
| Model 6 | 0.955   | 0.978   | 0.701   | 0.583   |

**Table 4.16:**  $R^2$  - Validation with approximately 1100 data points

|         | Femur 1 | Femur 2 | Femur 3 | Femur 4 |
|---------|---------|---------|---------|---------|
| Model 1 | 166     | 206     | -15     | 71      |
| Model 2 | 170     | 218     | -28     | 86      |
| Model 3 | 159     | 203     | -37     | 76      |
| Model 4 | 199     | 204     | 68      | 68      |
| Model 5 | 188     | 228     | 9       | 74      |
| Model 6 | 186     | 231     | -15     | 79      |

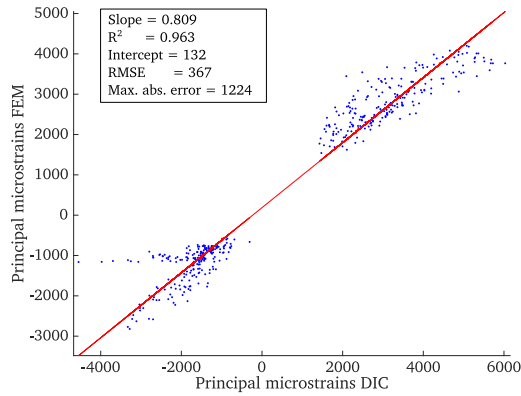
**Table 4.17:** Intercept  $[\mu\varepsilon]$  - Validation with approximately 1600 data points

|         | Femur 1 | Femur 2 | Femur 3 | Femur 4 |
|---------|---------|---------|---------|---------|
| Model 1 | 391     | 260     | 307     | 403     |
| Model 2 | 396     | 279     | 309     | 391     |
| Model 3 | 390     | 278     | 304     | 384     |
| Model 4 | 353     | 255     | 308     | 411     |
| Model 5 | 394     | 266     | 315     | 404     |
| Model 6 | 399     | 282     | 312     | 384     |

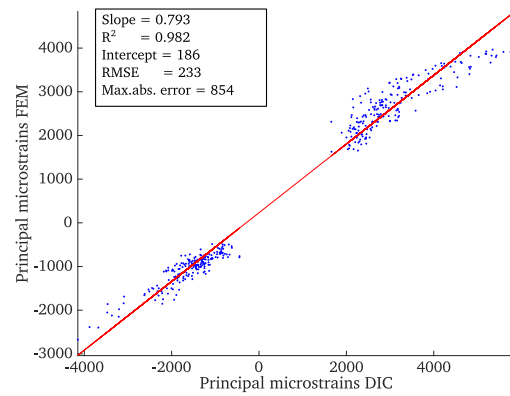
**Table 4.18:** RSME [ $\mu\varepsilon$ ] - Validation with approximately 1600 data points

|         | Femur 1 | Femur 2 | Femur 3 | Femur 4 |
|---------|---------|---------|---------|---------|
| Model 1 | 2312    | 941     | 12645   | 17437   |
| Model 2 | 2330    | 1063    | 12744   | 17020   |
| Model 3 | 2310    | 1014    | 12546   | 16748   |
| Model 4 | 2137    | 1048    | 6366    | 17690   |
| Model 5 | 2303    | 1002    | 12811   | 17440   |
| Model 6 | 2321    | 1083    | 12788   | 16890   |

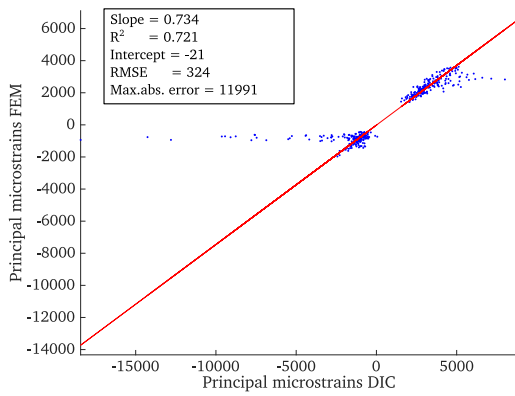
**Table 4.19:** Maximum error [ $\mu\varepsilon$ ] - Validation with approximately 1600 data points



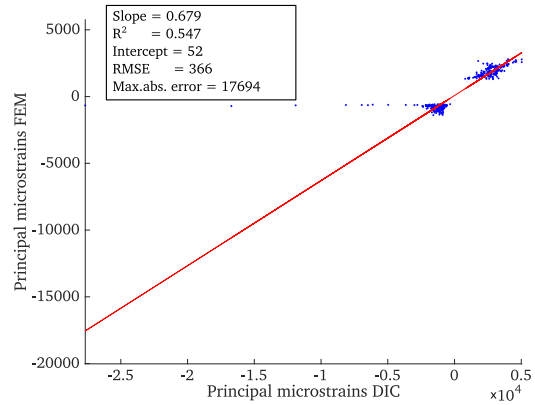
(a) Femur 1: Correlation of principal strains - Model 6



(b) Femur 2: Correlation of principal strains - Model 6



(c) Femur 3: Correlation of principal strains - Model 6

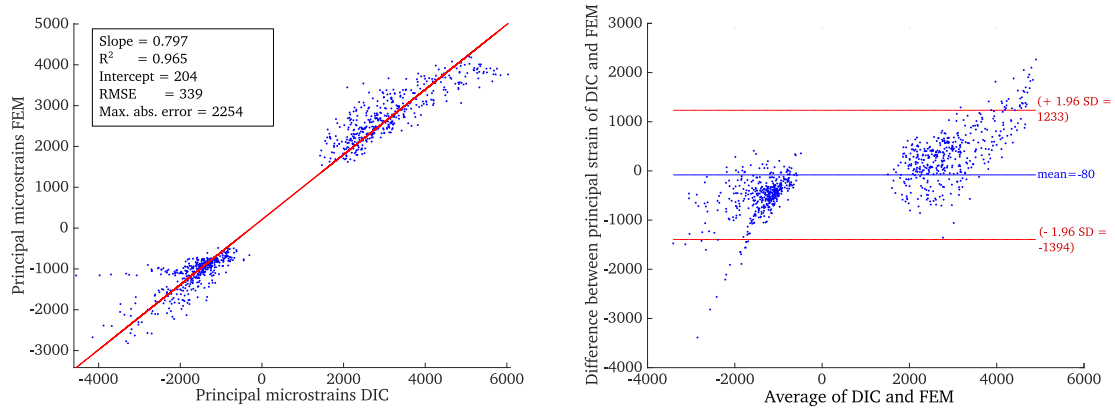


(d) Femur 4: Correlation of principal strains - Model 6

**Figure 4.17:** Scatter plots of each bone respectively - Specimen 3 and 4 show high errors

|         | Slope | $R^2$ | Intercept | RMSE | Maximum absolute error |
|---------|-------|-------|-----------|------|------------------------|
| Model 1 | 0.769 | 0.964 | 185       | 329  | 2178                   |
| Model 2 | 0.791 | 0.965 | 193       | 336  | 2253                   |
| Model 3 | 0.779 | 0.964 | 181       | 333  | 2230                   |
| Model 4 | 0.736 | 0.965 | 199       | 302  | 2057                   |
| Model 5 | 0.777 | 0.964 | 207       | 332  | 2180                   |
| Model 6 | 0.797 | 0.965 | 208       | 339  | 2254                   |

**Table 4.20:** Pooled data when femur 3 and 4 were removed



**(a)** Scatter plot for two composite bones **(b)** Bland-Altman plot for two composite bones (Specimen 1 and 2) at 4000 N

**Figure 4.18:** Model 6 - model with best correlation

# Chapter 5

## Discussion

The aim of the thesis was to validate subject-specific FE-models of composite bones against in-vitro measured strains at the medial aspect of the femoral neck in a sideways-fall loading configuration. First, in-vitro tests were performed to collect DIC-strain data in order to validate the models. Displacements and strains were measured in a non-destructive loading case at 1120 N and 4000 N. Repeatability of the data obtained was evaluated to ensure reliability of strain data used for validation. Second, eight different FE-models with varying boundary conditions at femoral head and trochanter were built. Third, a validation algorithm was developed to assess estimation of principal strains in FE-models with DIC data. Minor and major principal strains predicted by FE-models were validated against measurement data obtained using DIC. A linear regression analysis was performed between experimental and FE calculated values.

Five composite bones were tested in a sideways-fall loading condition. Each bone was tested non-destructively for 5 times at a load of 1120 N, and then finally tested until complete fracture. For estimating repeatability of the measurements, displacements and strains within every test set were compared to the data obtained from the third bone at a load of 560 N and 1120 N. Displacements showed good repeatability whereas major and minor principal strains revealed high noise all over the measured

area. Repeatability improved with higher strains from 560 N to 1120 N, which is consistent with findings of other studies [40].

Eight different FE-models were built from CT-images of the five composite bones. The goal was to find the best configuration of BCs in order to obtain the best accuracy in strain estimation. The following steps were consistently applied:

1. Segmentation of the CT-images
2. Reverse engineering of segmented surface geometries
3. Meshing with 10-noded tetrahedral elements
4. Assigning material properties to every component according to data provided by the manufacturer
5. Applying different BC

A similar modelling procedure has been used in the past, giving good accuracy in strain prediction in single-leg-stance condition [22]. BCs differed in modelling of the contact between loading device and femur at trochanter and head (simple constrain in the parallel direction to load, direct load application on femoral head, contact modelling on one or both sites) and in implementing conditions at the surface of the epoxy pot in which the femoral stem was embedded (constrain of surface, modelling hinge at the lateral side of the stem with kinematic coupling). For validation, minor and major principal strains were estimated at a load of 1120 N and 4000 N and were compared to data obtained from DIC in the medial aspect of the femoral neck. The inter-specimen repeatability was evaluated qualitatively by comparing strain plots. As expected, the strain data of FE-models of composite bones did not show significant differences between the samples, except at 4000 N in femur 4 (see figure 4.14). The strain distributions were similar in the region of interest in all samples concerning minor and major principal strains.

DIC as a non-contact measuring technique provided a full-field strain distribution which could be used to more extensively validate strains in that region than e.g. with SGs which only provide a limited number of measurement points. Neverthe-

less, some data points had to be removed due to invalid measurements because of curvature and reflection and at the edges of the point cloud. The models were validated with about 1600 data points per test. At a load of 1120 N the best prediction accuracy of principal strains with pooled data showed a correlation of 96 percent ( $slope = 0.70$ ,  $R^2 = 0.915$ ). As noise is known to have higher influence on strain derivation from DIC when strains are small, we included modelling and measurements with higher load (4000 N). For tests at 4000 N we excluded one model with contact modelled with friction at head and trochanter, since it had shown very low correlation at 1120 N (model 8). The best correlation obtained at this load was 88 percent ( $slope = 0.750$ ,  $R^2 = 0.773$ ). The low  $R^2$  resulted from some significant outliers during the measurements with DIC in femur 3 and 4 (see figure 4.17c and figure 4.17d). The maximum error was about 8 to 16 times higher than in the other bones. Therefore, we excluded these specimens from the pooled data and obtained a correlation of 98 percent ( $slope = 0.797$ ) and the  $R^2$  improved to 0.965.

In general, FE-models with different boundary conditions did not show significant differences except when contact was implemented with friction of 0.65, which led to significantly worse correlation (Model 8). Models with more complex boundary conditions (e.g. contact modelling) did not perform significantly better than models implemented very straight forward with constrained nodes and force directly applied. At 1120 N, the slope of the regression curve varied from 0.671 to 0.700 and  $R^2$  was consistently high between 0.900 and 0.914. At 4000 N slope varied from 0.717 to 0.750 and the  $R^2$  was between 0.772 and 0.824, which is significantly lower due to outliers in DIC measurements of femur 3 and 4. When these femurs were removed from the pooled data, the slope improved to values from 0.736 to 0.797 and  $R^2$  was either 0.964 or 0.965. The coefficients of determination obtained from linear regression analysis between strains of measured during experiments and FE-models corresponds to these reported in literature, where  $R^2$  ranged between 0.87 and 0.95 [20] [18] [22] [14] [3] [48] [49] [44] (see also table 3.4). The accuracy obtained was inferior compared to the studies of others, as we obtained a maximum slope of the regression function

of 0.797 at a load of 4000 N, whereas slopes in literature ranged between 0.84 [22] and 1.06 [20]. Our FE-models generally underestimated absolute values of principal strains by 30 percent.

Limitations of the study were the high noise in strain measurements and that FE-models were only compared to one test at 4000 N. Noise has more influence when strains are small since the strains are calculated as the spatial derivative of the measured displacements. Therefore, we included tests at 4000 N for validation. We further tried to overcome the issue by pooling the data of the five DIC-test at 1120 N and filtering.

Furthermore, models 3, 6 and 7 did not converge for femur 5 at a load of 4000 N, therefore this bone was excluded. Further investigations will be performed to find out the reason for that, as models were built in a consistent way. Also the fact that FE-models of femur 4 showed different distribution of strains especially in the femoral head (see figure 4.14) deserves further attention. Refining the mesh size and decreasing the minimum loading step might be a solution, but would also lead to much longer calculation times.

We did not implement the different stiffness of cortical bone in tension and compression as indicated by the manufacturer, which might also have influenced the prediction accuracy of our FE-models.

Another limitation was the loading configuration, which might have changed during load application. The jig which was manufactured to hold the specimen in position deformed several millimeters and the rotation of the bone increased with about 15 degrees when applying higher loads until fracture. It should be further investigated how much changing BCs are influencing strain distribution and correlation.

A further issue might be the resolution of the CT-scans, as the cortical shell showed sub-pixel thickness in some parts of the surface located also in the area of the femoral neck. The overestimation of the cortical thickness might explain why strains were underestimated, as an increased amount of cortical material correlates with increased stiffness of the bone.

To the authors knowledge this was the first study to use DIC measurements for validations of FE-models of a sideways fall with non-destructive loads. DIC as an optical non-contact technique provides a rich data set with a high resolution for validation. This is an advantage compared to discrete measurement devices like SGs, as the full field can be used for validation of FE-models and allows tracking of peak strain values more accurately [22].

Composite bones have similar mechanical properties as cadaver femurs, but show less inter-specimen variability. They were used to simplify evaluating effectiveness, repeatability and automation of the modelling and validation procedure. We were concentrating on the medial femoral neck, which also may be a sensitive site for assessment of fracture risk due to fall [4]. The models were consistently underestimating strains by about 30 percent, but correlation was consistently high (above 0.9 in the pooled data). This deserves further attention, as it is crucial to not underestimate strains for assessment of fracture risk in the long run and the femoral neck is assumed to be an important site concerning high strains and fracture during sideways falls. Despite those limitations, the proposed combined experimental and numerical method proved to be ready for direct application in human cadaver femur testing. The algorithm used has proved to be valuable for the registration and validation of FE-models concerning principal strain prediction. Tests in the same loading configuration are currently prepared in our group, which will allow an accurate tuning of the FE-modelling procedure. Furthermore, a deeper insight into the strain behaviour of human femurs will be provided. In the long run, this should contribute to the development of a reliable subject-specific fracture risk criterion.

# Appendix A

## Repeatability of DIC

### A.1 Repeatability of displacements and strains - compared to test 3

|         | slope |       |       |       |       | $R^2$ |       |       |       |       |
|---------|-------|-------|-------|-------|-------|-------|-------|-------|-------|-------|
|         | T1    | T2    | T3    | T4    | T5    | T1    | T2    | T3    | T4    | T5    |
| Femur 1 | 1.251 | 1.031 | 1.000 | 1.003 | 0.966 | 0.869 | 0.941 | 1.000 | 0.934 | 0.928 |
| Femur 2 | 1.495 | 0.875 | 1.000 | 0.871 | 0.868 | 0.728 | 0.913 | 1.000 | 0.887 | 0.845 |
| Femur 3 | 1.182 | 1.162 | 1.000 | 0.969 | 0.955 | 0.884 | 0.027 | 1.000 | 0.935 | 0.915 |
| Femur 4 | 1.022 | 0.959 | 1.000 | 0.840 | 0.803 | 0.811 | 0.874 | 1.000 | 0.869 | 0.824 |
| Femur 5 | 1.340 | 1.000 | 1.000 | -     | 1.030 | 0.925 | 0.939 | 1.000 | -     | 0.955 |

**Table A.1:** LOAD: 560 N - Displacements of tests (T) compared to T3: Slope and  $R^2$  for each test respective to T3

|         | slope |       |       |       |       | $R^2$ |       |       |       |       |
|---------|-------|-------|-------|-------|-------|-------|-------|-------|-------|-------|
|         | T1    | T2    | T3    | T4    | T5    | T1    | T2    | T3    | T4    | T5    |
| Femur 1 | 0.639 | 0.703 | 1.000 | 0.699 | 0.733 | 0.442 | 0.667 | 1.000 | 0.586 | 0.670 |
| Femur 2 | 0.487 | 0.716 | 1.000 | 0.715 | 0.691 | 0.292 | 0.603 | 1.000 | 0.770 | 0.708 |
| Femur 3 | 0.711 | 0.791 | 1.000 | 0.855 | 0.850 | 0.520 | 0.436 | 1.000 | 0.639 | 0.896 |
| Femur 4 | 0.564 | 0.672 | 1.000 | 0.668 | 0.693 | 0.373 | 0.663 | 1.000 | 0.665 | 0.559 |
| Femur 5 | 0.722 | 0.680 | 1.000 | -     | 0.915 | 0.407 | 0.680 | 1.000 | -     | 0.644 |

**Table A.2:** LOAD: 560 N - Major and minor principal strains: Slope and  $R^2$  for each test respective to T3

|         | slope |       |       |       |       | $R^2$ |       |       |       |       |
|---------|-------|-------|-------|-------|-------|-------|-------|-------|-------|-------|
|         | T1    | T2    | T3    | T4    | T5    | T1    | T2    | T3    | T4    | T5    |
| Femur 1 | 1.647 | 1.011 | 1.000 | 1.003 | 0.973 | 0.886 | 0.941 | 1.000 | 0.936 | 0.933 |
| Femur 2 | 1.761 | 0.994 | 1.000 | 0.922 | 0.929 | 0.723 | 0.913 | 1.000 | 0.887 | 0.847 |
| Femur 3 | 1.584 | 1.150 | 1.000 | 0.961 | 0.943 | 0.854 | 0.083 | 1.000 | 0.914 | 0.896 |
| Femur 4 | 1.481 | 1.015 | 1.000 | 0.880 | 0.861 | 0.815 | 0.865 | 1.000 | 0.864 | 0.820 |
| Femur 5 | 1.469 | 1.036 | 1.000 | -     | 0.999 | 0.916 | 0.933 | 1.000 | -     | 0.950 |

**Table A.3:** LOAD: 1120 N - Displacements of tests (T) compared to T3: Slope and  $R^2$  for each test respective to T3

|         | slope |       |       |       |       | $R^2$ |       |       |       |       |
|---------|-------|-------|-------|-------|-------|-------|-------|-------|-------|-------|
|         | T1    | T2    | T3    | T4    | T5    | T1    | T2    | T3    | T4    | T5    |
| Femur 1 | 0.894 | 0.816 | 1.000 | 0.835 | 0.950 | 0.469 | 0.618 | 1.000 | 0.493 | 0.646 |
| Femur 2 | 0.704 | 0.807 | 1.000 | 0.872 | 0.836 | 0.337 | 0.566 | 1.000 | 0.675 | 0.634 |
| Femur 3 | 0.882 | 0.857 | 1.000 | 0.903 | 0.851 | 0.544 | 0.627 | 1.000 | 0.616 | 0.763 |
| Femur 4 | 0.968 | 0.782 | 1.000 | 0.908 | 0.845 | 0.531 | 0.665 | 1.000 | 0.716 | 0.648 |
| Femur 5 | 0.796 | 0.684 | 1.000 | -     | 0.846 | 0.360 | 0.552 | 1.000 | -     | 0.614 |

**Table A.4:** LOAD: 1120 N - Major and minor principal strains: Slope and  $R^2$  for each test respective to T3

## A.2 Deviation of Absolute displacements and Minor and Major strains for every Specimen

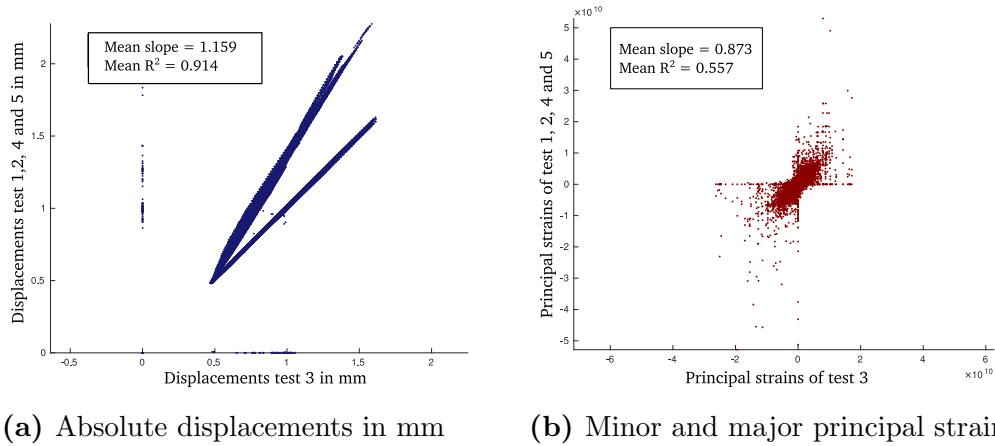


Figure A.1: Specimen 1 - load 1120 N - pooled data of 4 tests compared to test 3

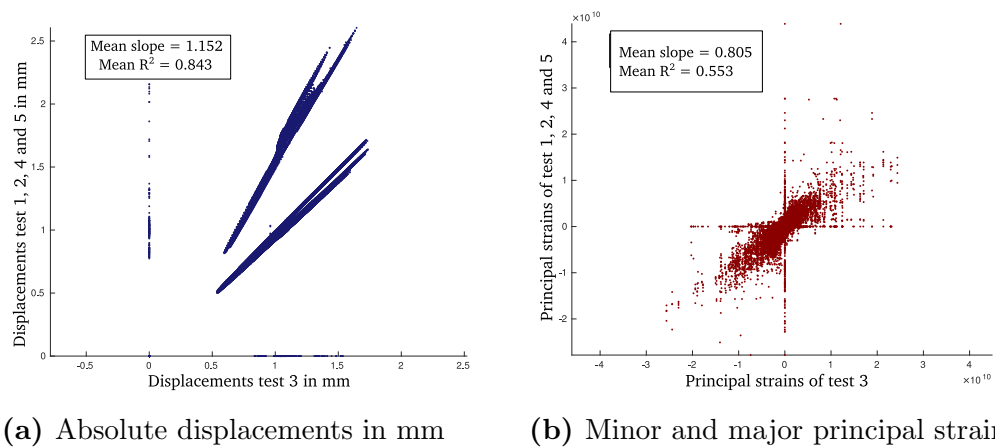
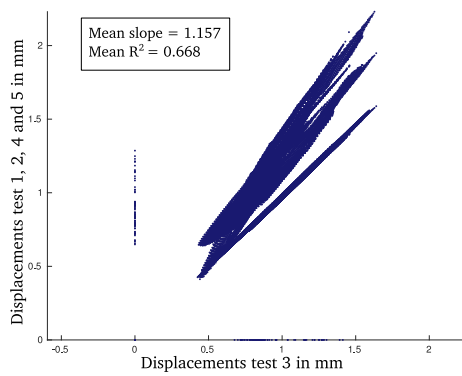
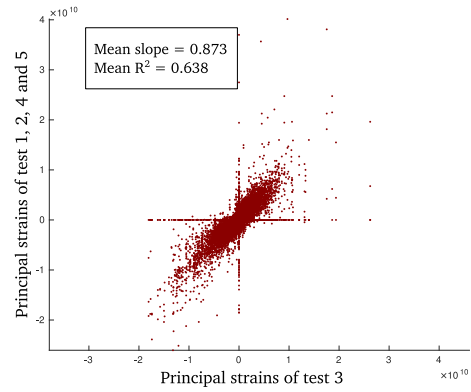


Figure A.2: Specimen 2 - load 1120 N - pooled data of 4 tests compared to test 3

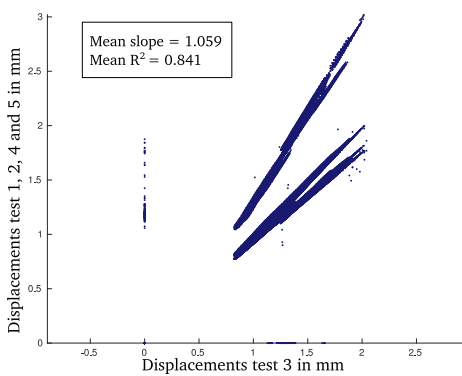


(a) Absolute displacements in mm

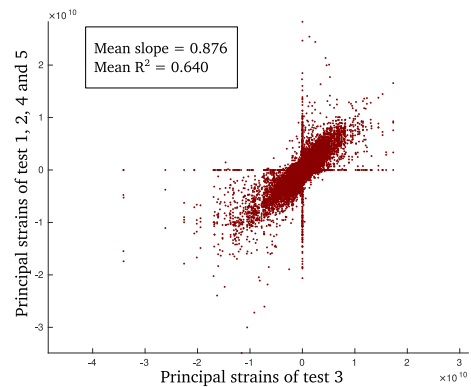


(b) Minor and major principal strains

**Figure A.3:** Specimen 3 - load 1120 N - pooled data of 4 tests compared to test 3

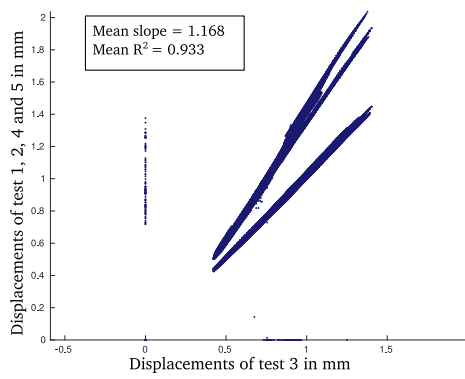


(a) Absolute displacements in mm

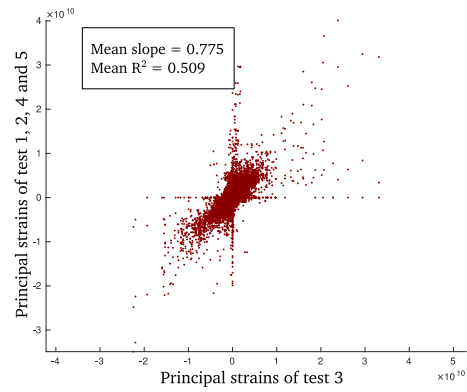


(b) Minor and major principal strains

**Figure A.4:** Specimen 4 - load 1120 N - pooled data of 4 tests compared to test 3



(a) Absolute displacement in mm



(b) Minor and major principal strains

**Figure A.5:** Specimen 5 - load 1120 N - pooled data of 4 tests compared to test 3

## Appendix B

### Repeatability of FE-models - qualitative

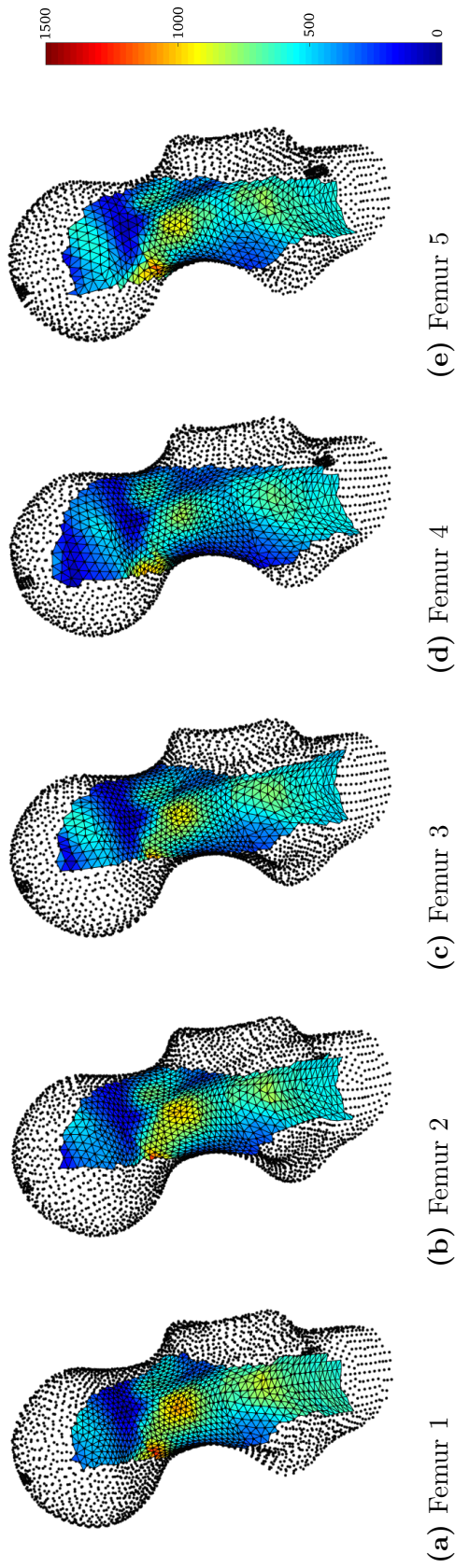


Figure B.1: Major principal strains  $[\mu\epsilon]$  in external elements in Model 1

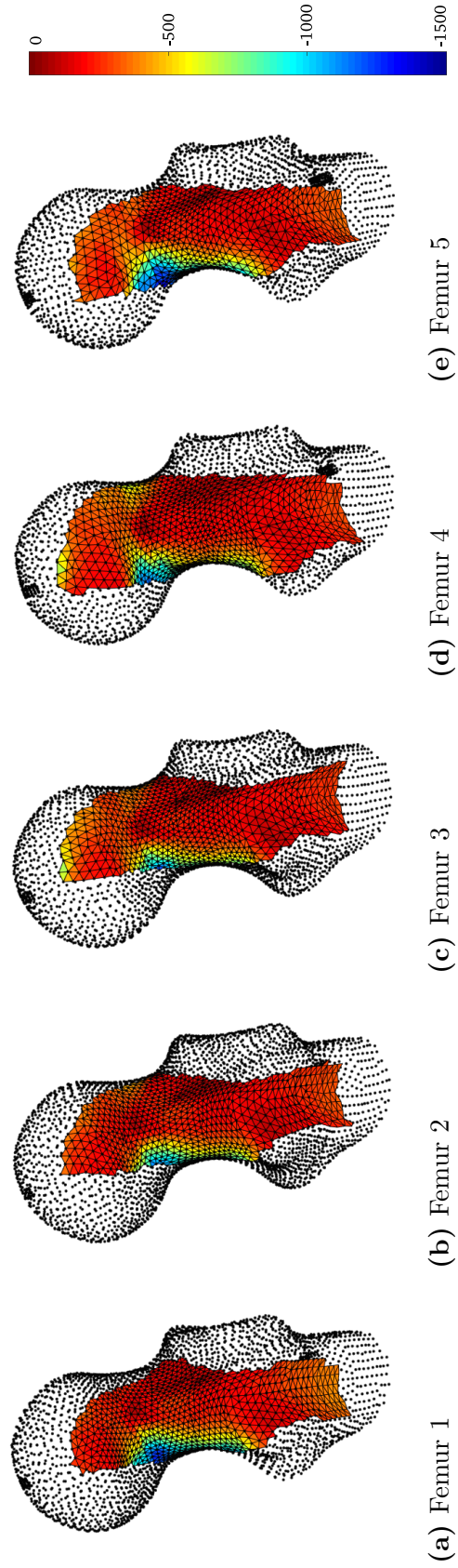
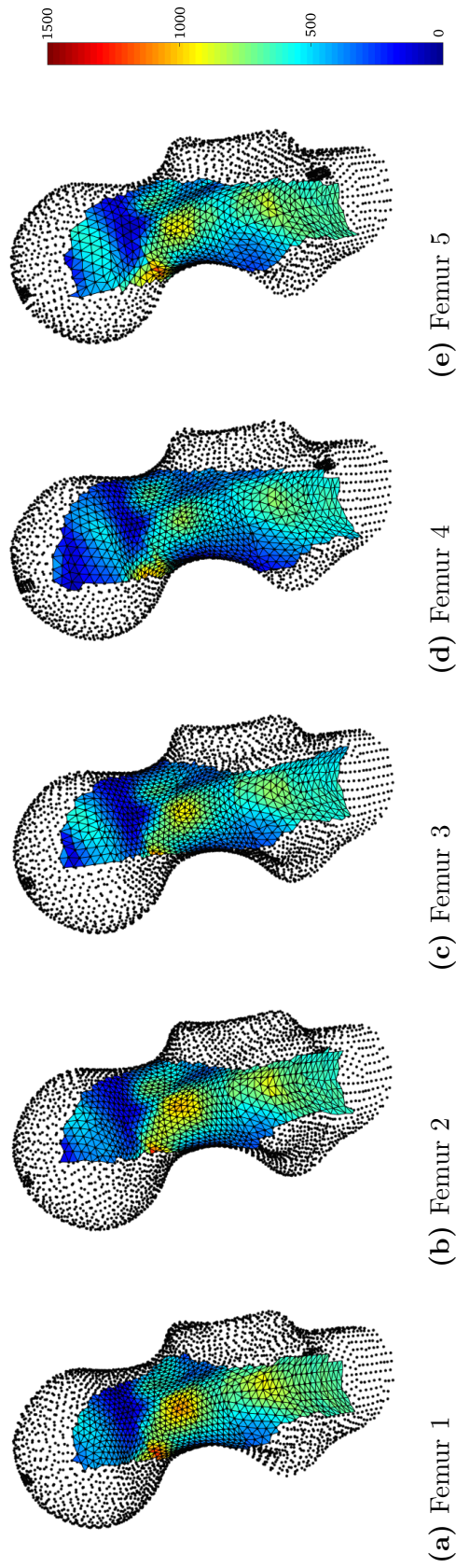
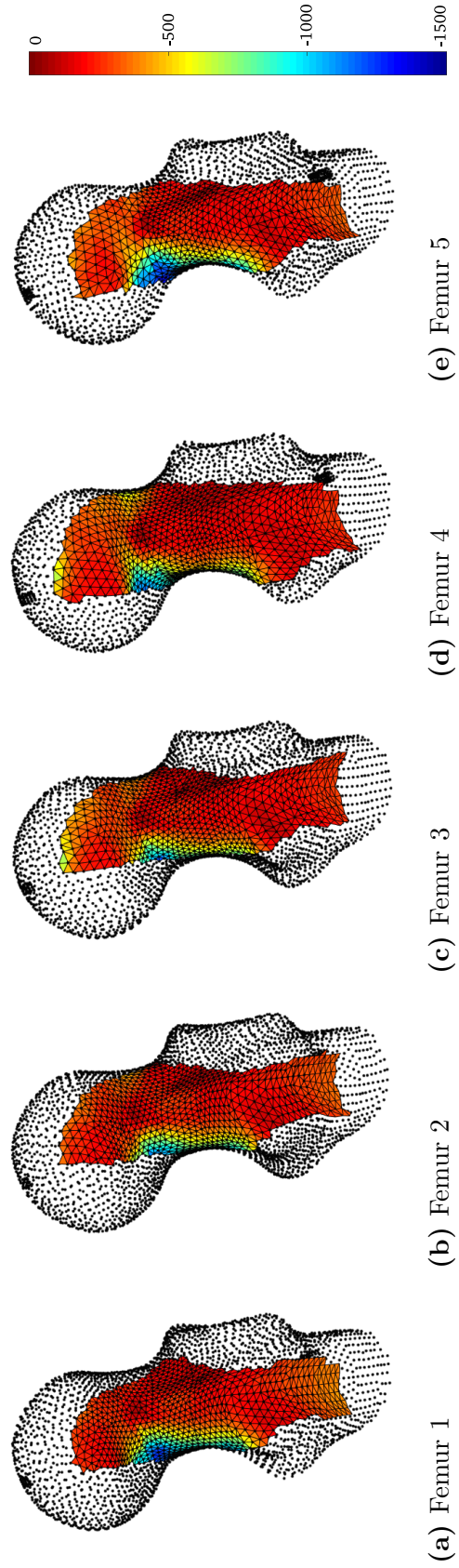


Figure B.2: Minor principal strains  $[\mu\epsilon]$  in external elements in Model 1



**Figure B.3:** Major principal strains  $[\mu\epsilon]$  in external elements in **Model 2**



**Figure B.4:** Minor principal strains  $[\mu\epsilon]$  in external elements in **Model 2**

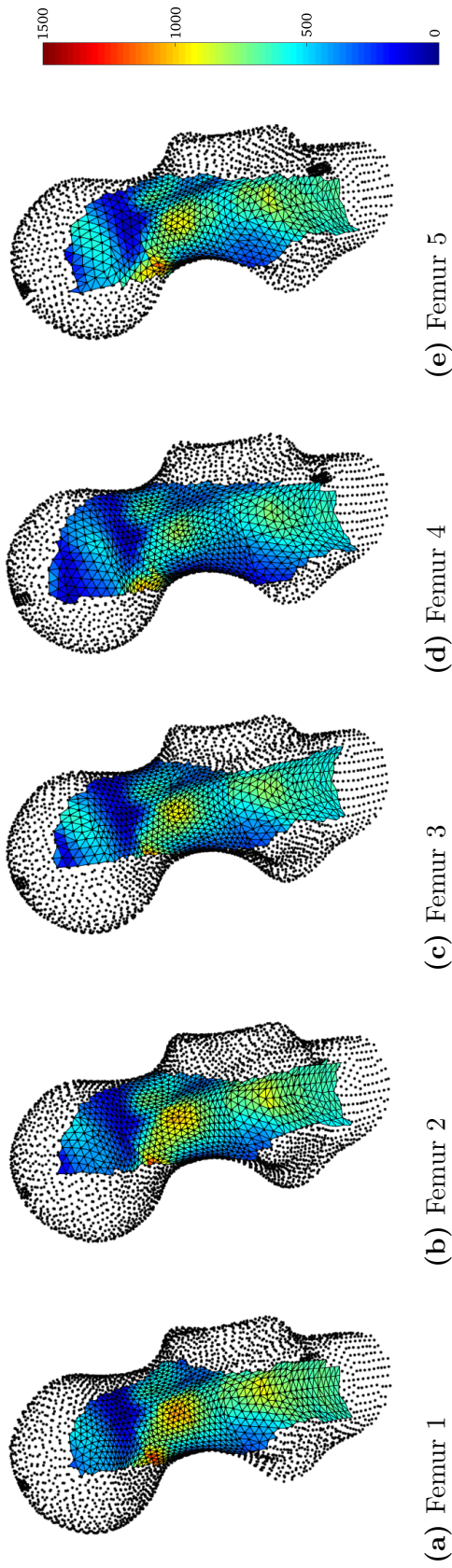


Figure B.5: Major principal strains  $[\mu\epsilon]$  in external elements in Model 3

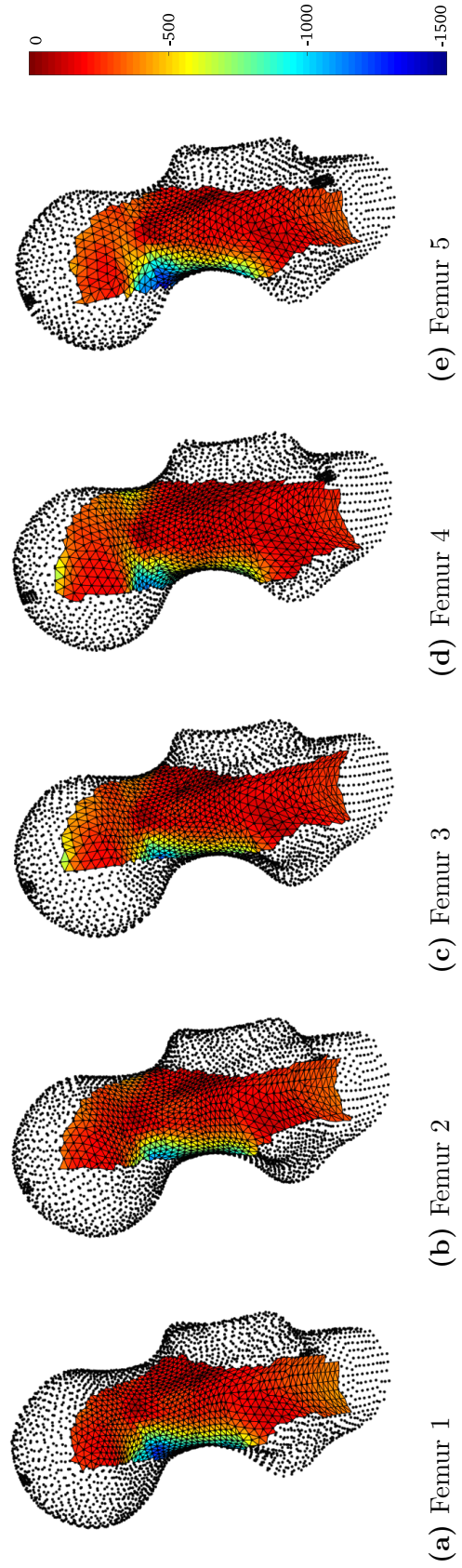
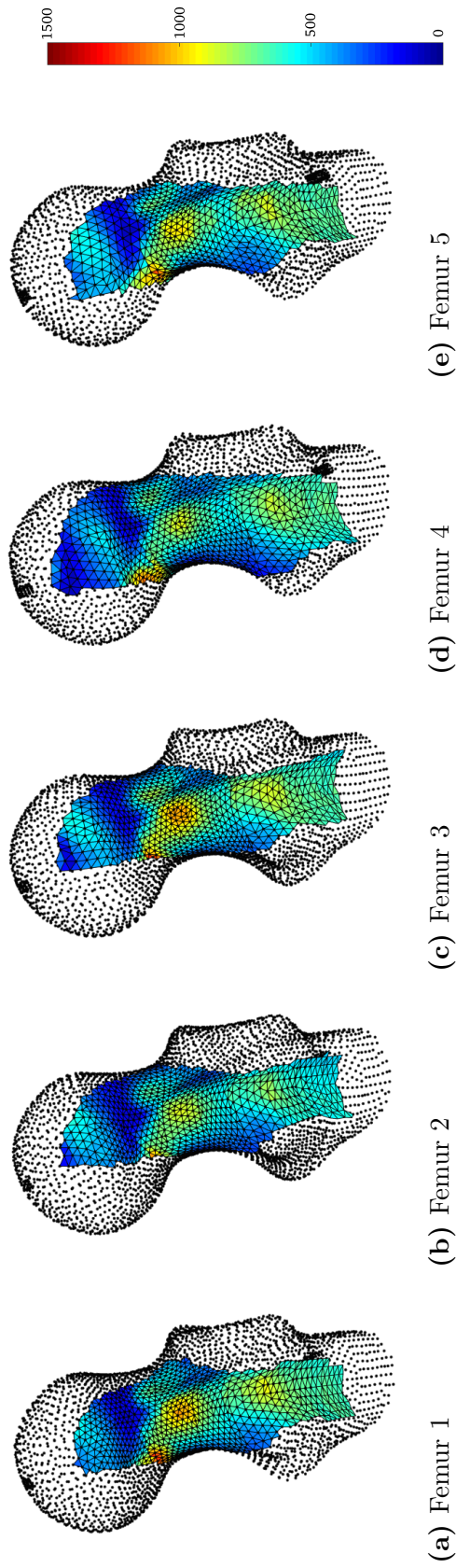
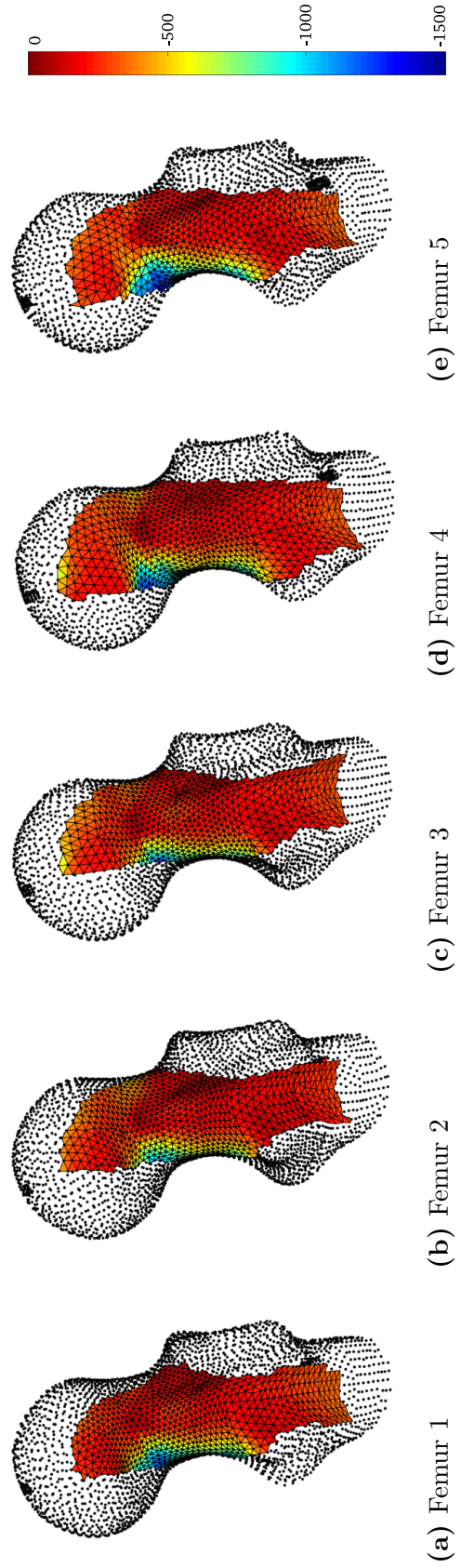


Figure B.6: Minor principal strains  $[\mu\epsilon]$  in external elements in Model 3



**Figure B.7:** Major principal strains  $[\mu\epsilon]$  in external elements in Model 4



**Figure B.8:** Minor principal strains  $[\mu\epsilon]$  in external elements in Model 4

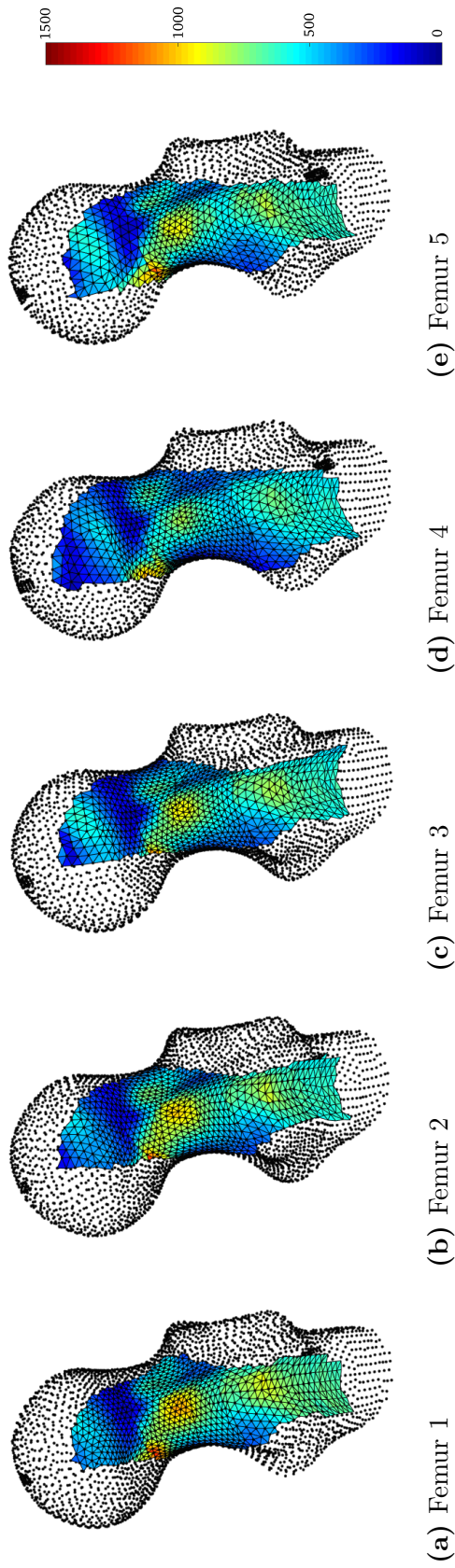


**Figure B.9:** Major principal strains [ $\mu\epsilon$ ] in external elements in Model 5

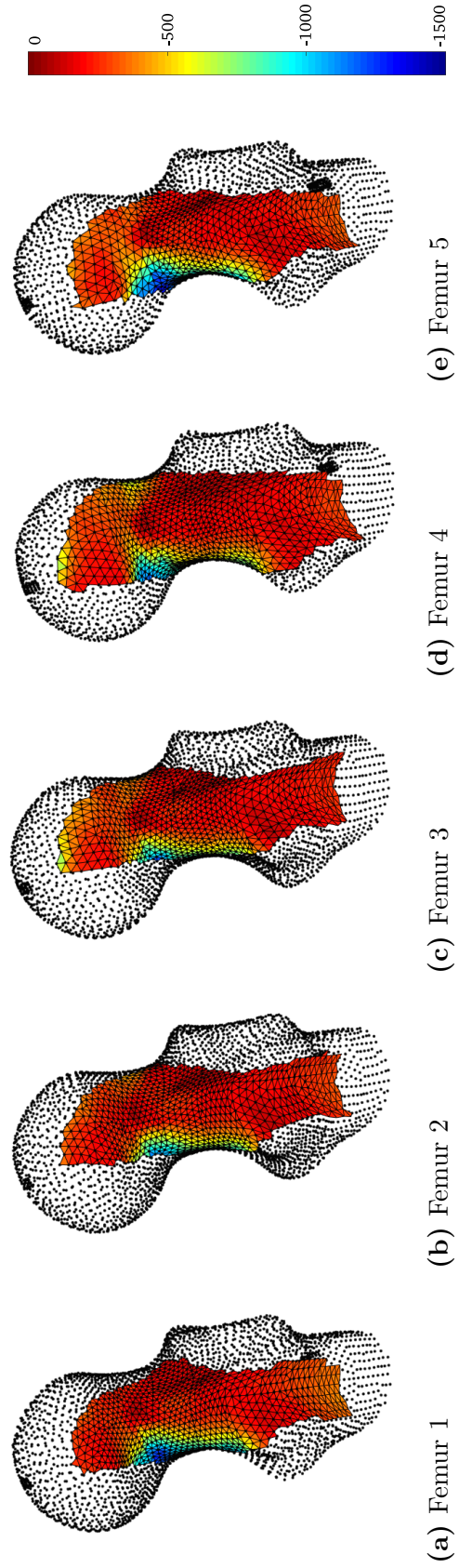


**Figure B.10:** Minor principal strains [ $\mu\epsilon$ ] in external elements in Model 5

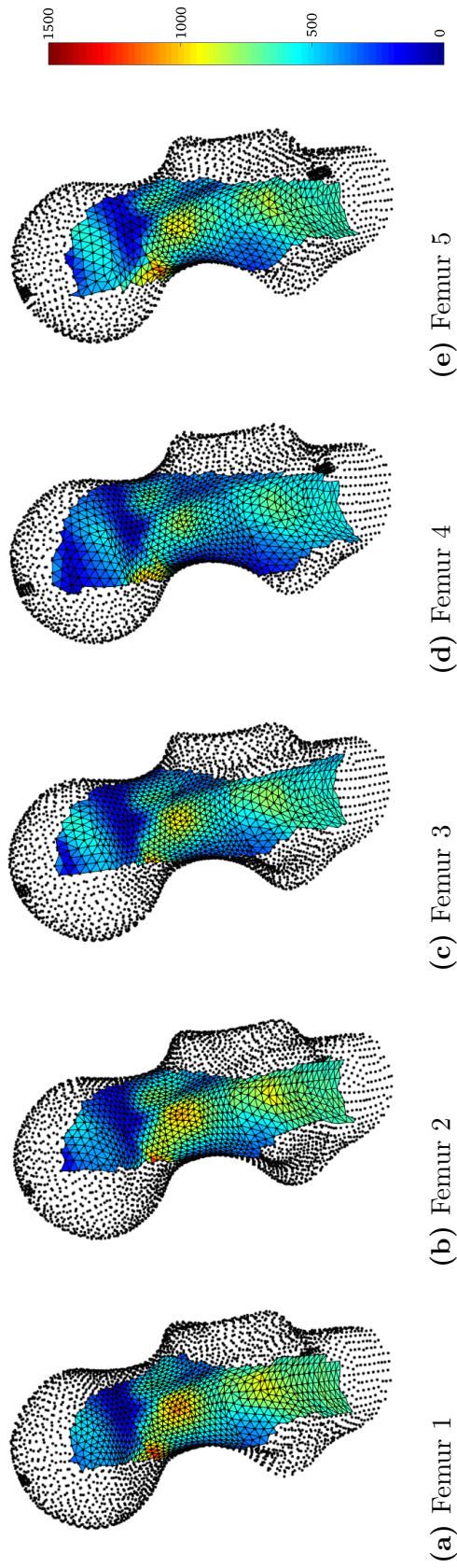


Figure B.11: Major principal strains  $[\mu\varepsilon]$  in external elements in Model 6

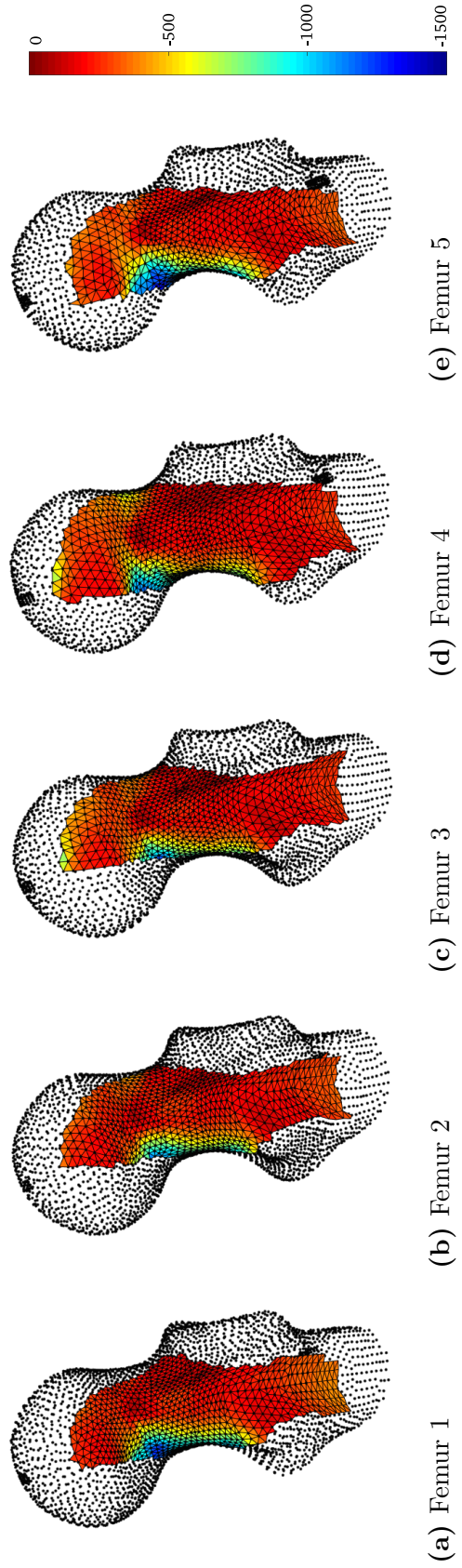
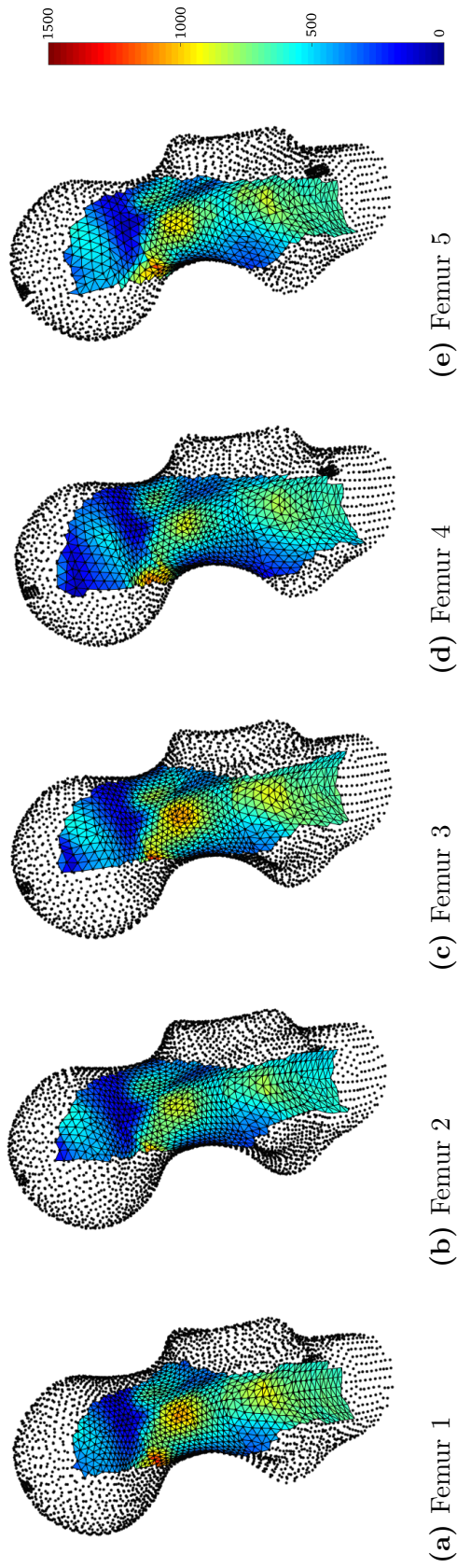
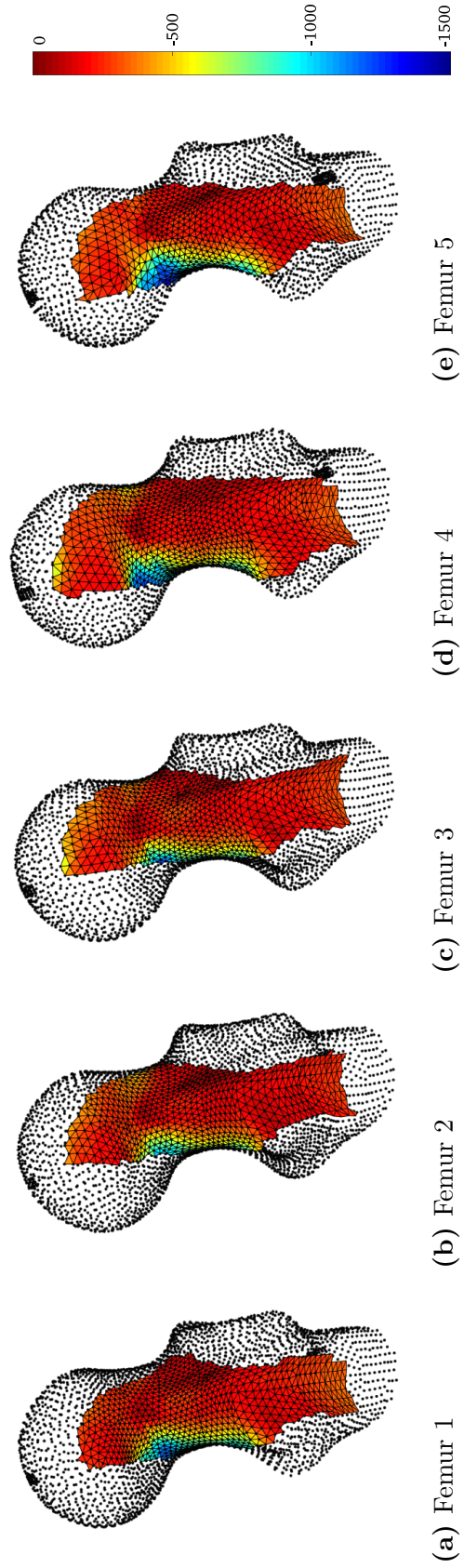


Figure B.12: Minor principal strains  $[\mu\varepsilon]$  in external elements in Model 6



**Figure B.13:** Major principal strains  $[\mu\epsilon]$  in external elements in Model 7



**Figure B.14:** Minor principal strains  $[\mu\epsilon]$  in external elements in Model 7

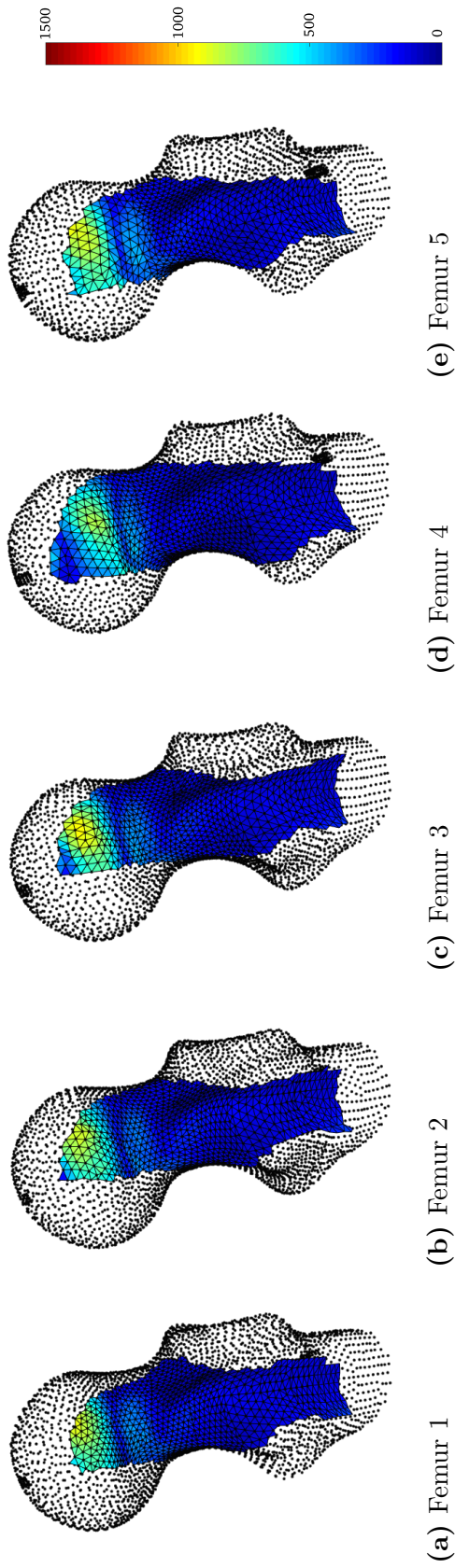


Figure B.15: Major principal strains  $[\mu\epsilon]$  in external elements in Model 8

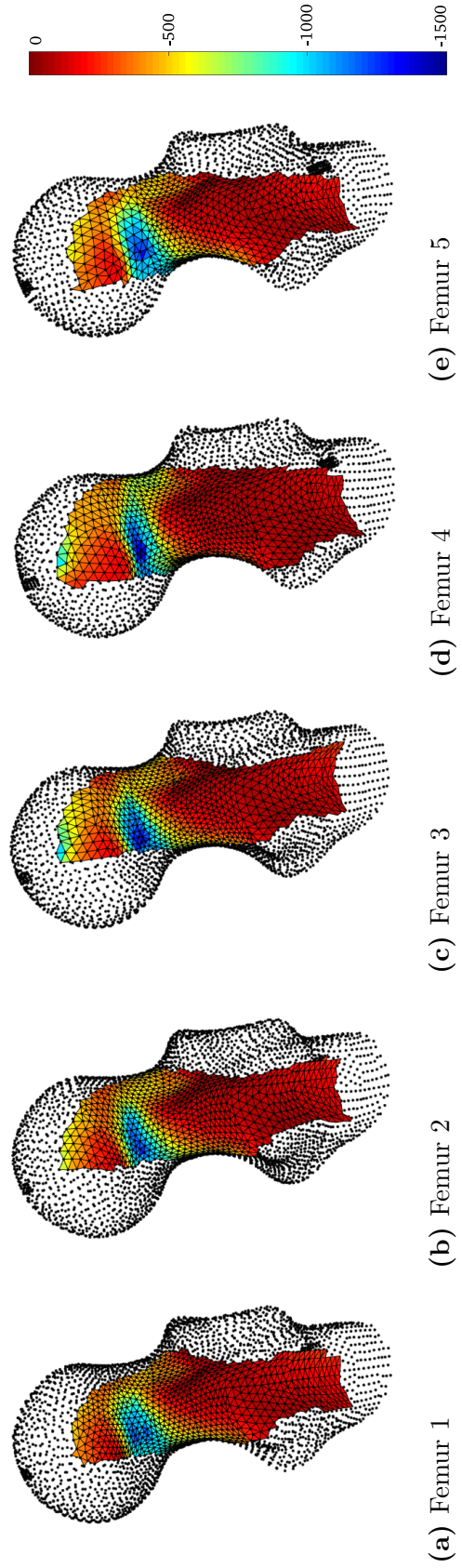


Figure B.16: Minor principal strains  $[\mu\epsilon]$  in external elements in Model 8

## Appendix C

### Inter-specimen repeatability of FEM at 4000N

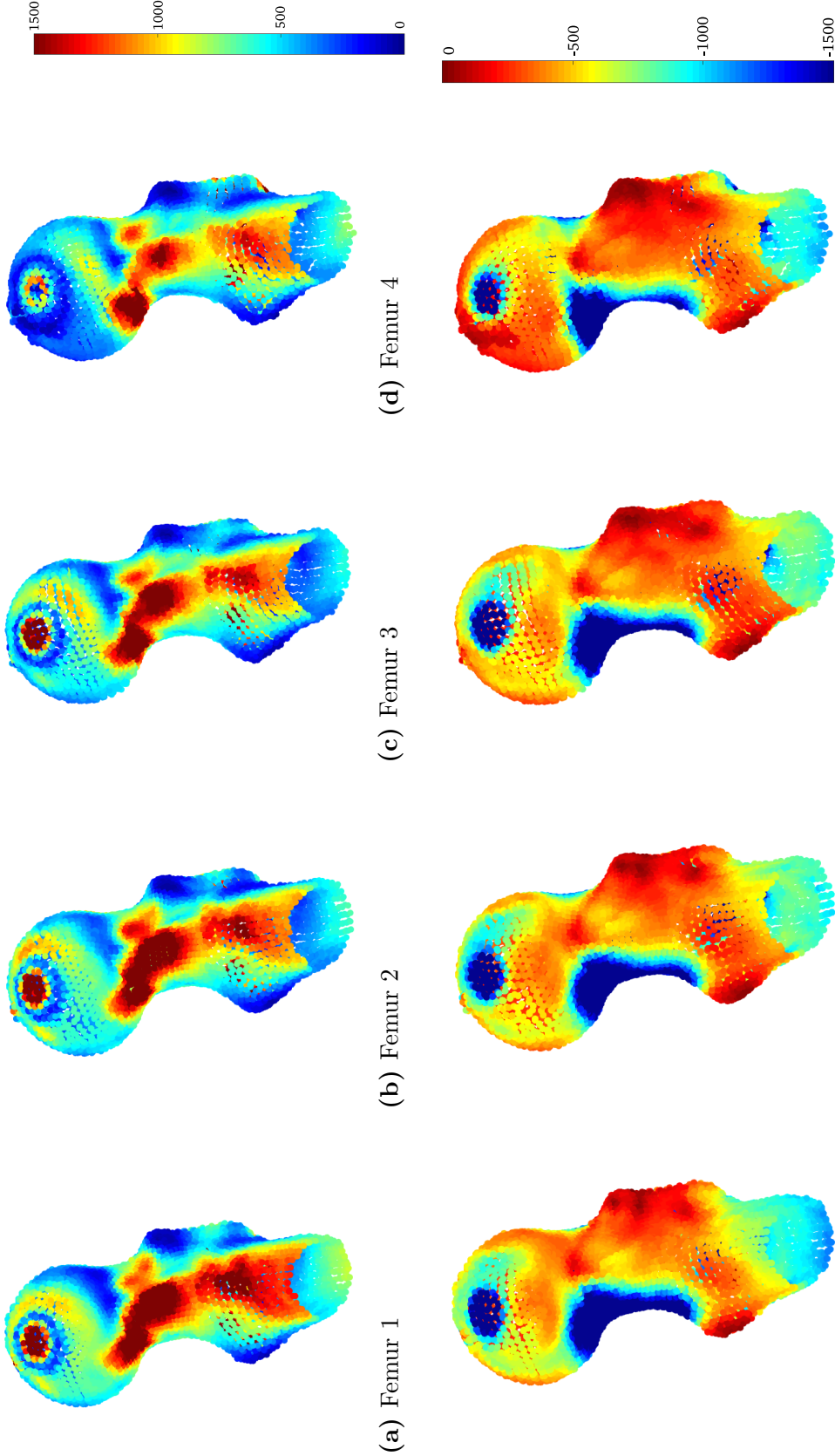


Figure C.1: Repeatability test of FE-models in model 1: major principal strains (top) and minor principal strains (bottom)

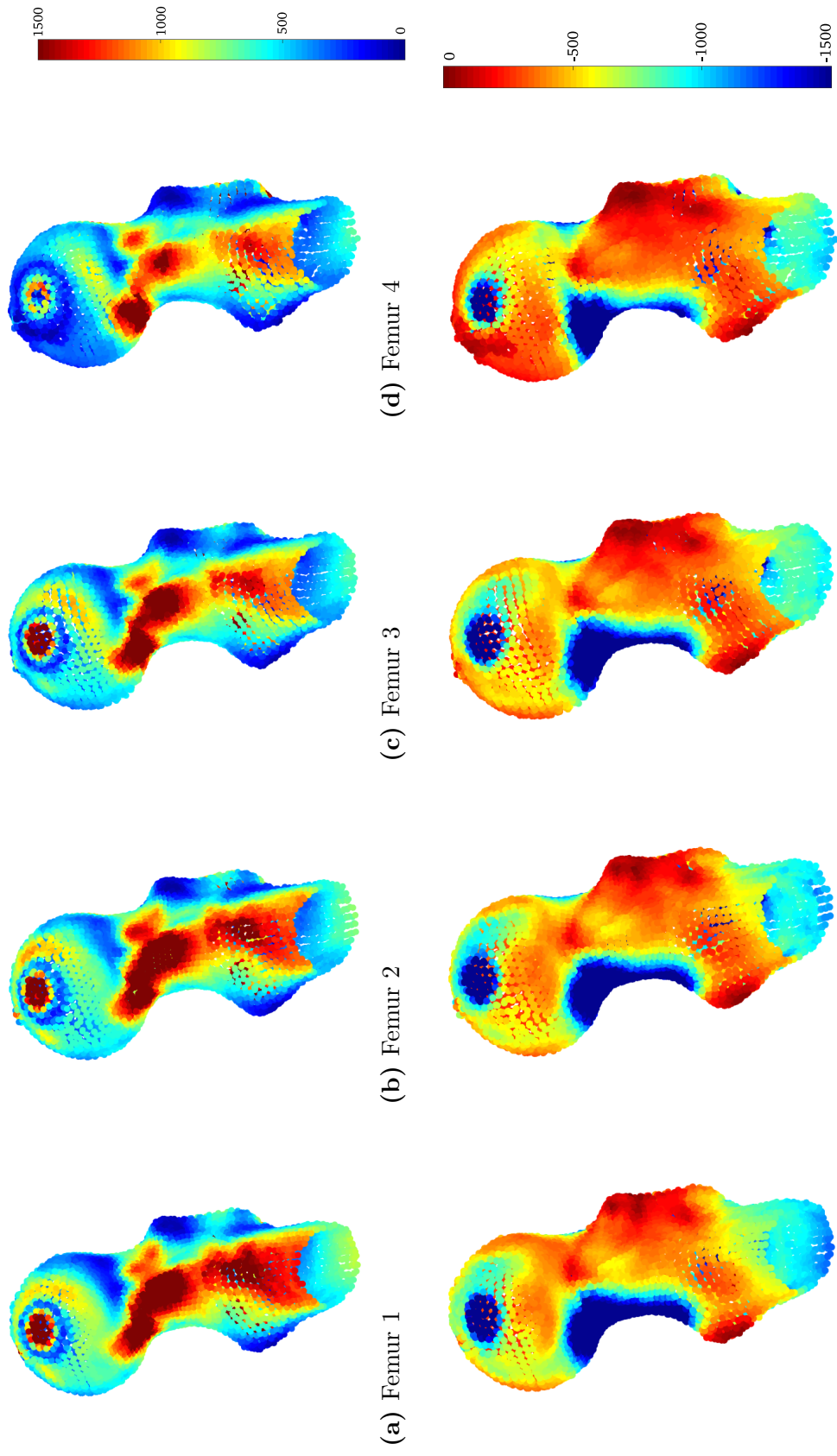


Figure C.2: Repeatability test of FE-models in model 2: major principal strains (top) and minor principal strains (bottom)

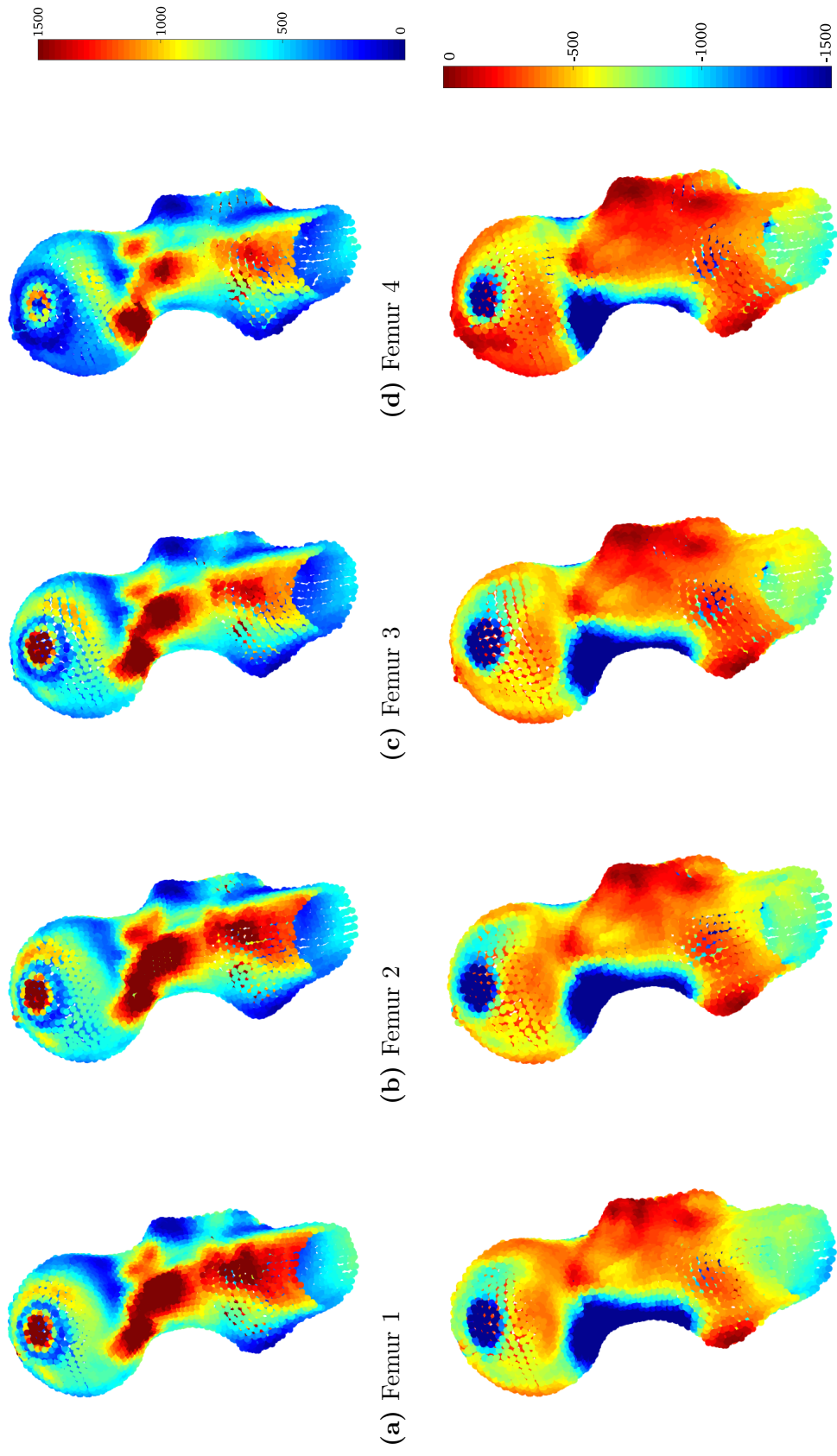


Figure C.3: Repeatability test of FE-models in model 3: major principal strains (top) and minor principal strains (bottom)

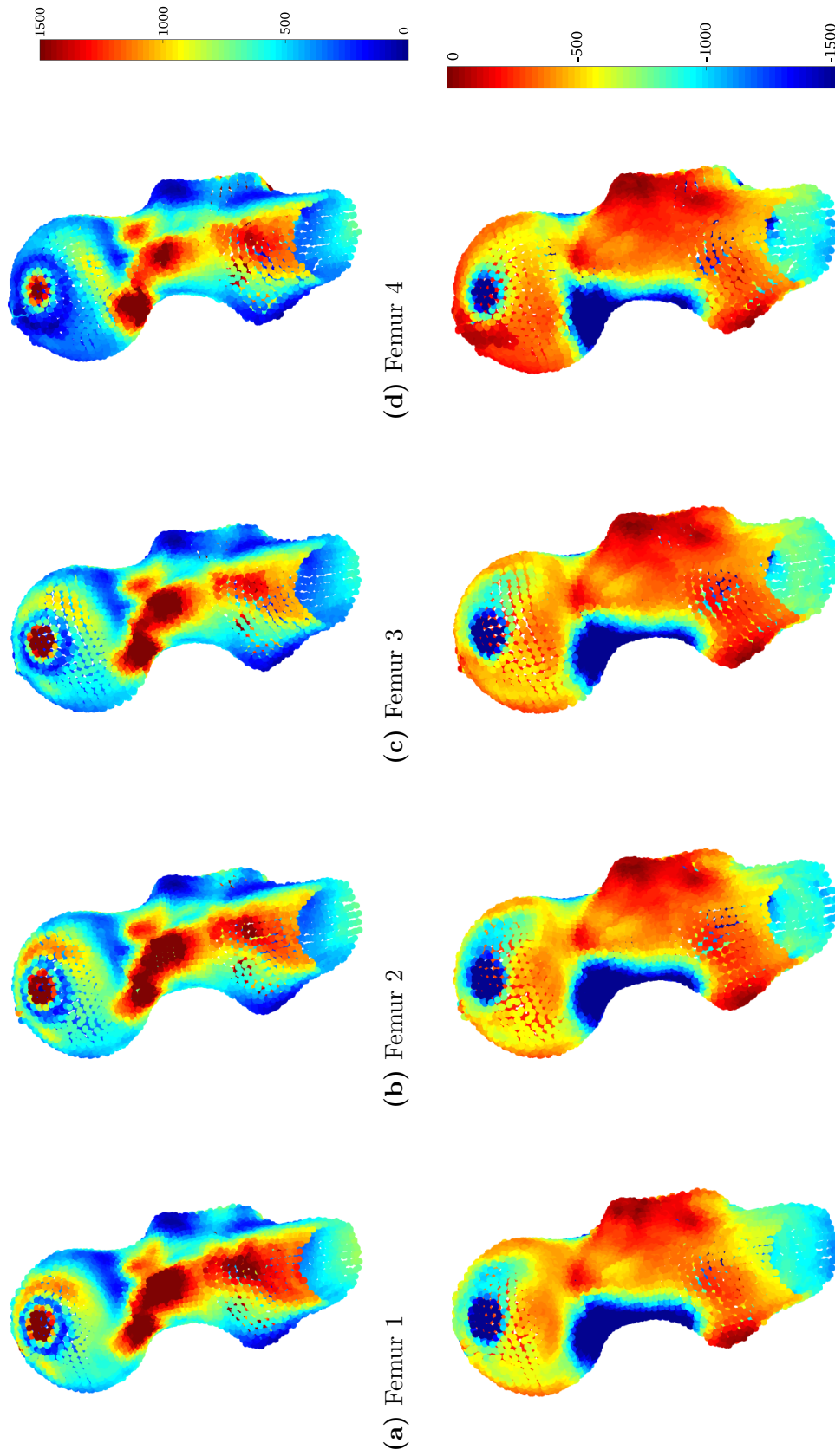


Figure C.4: Repeatability test of FE-models in model 4: major principal strains (top) and minor principal strains (bottom)

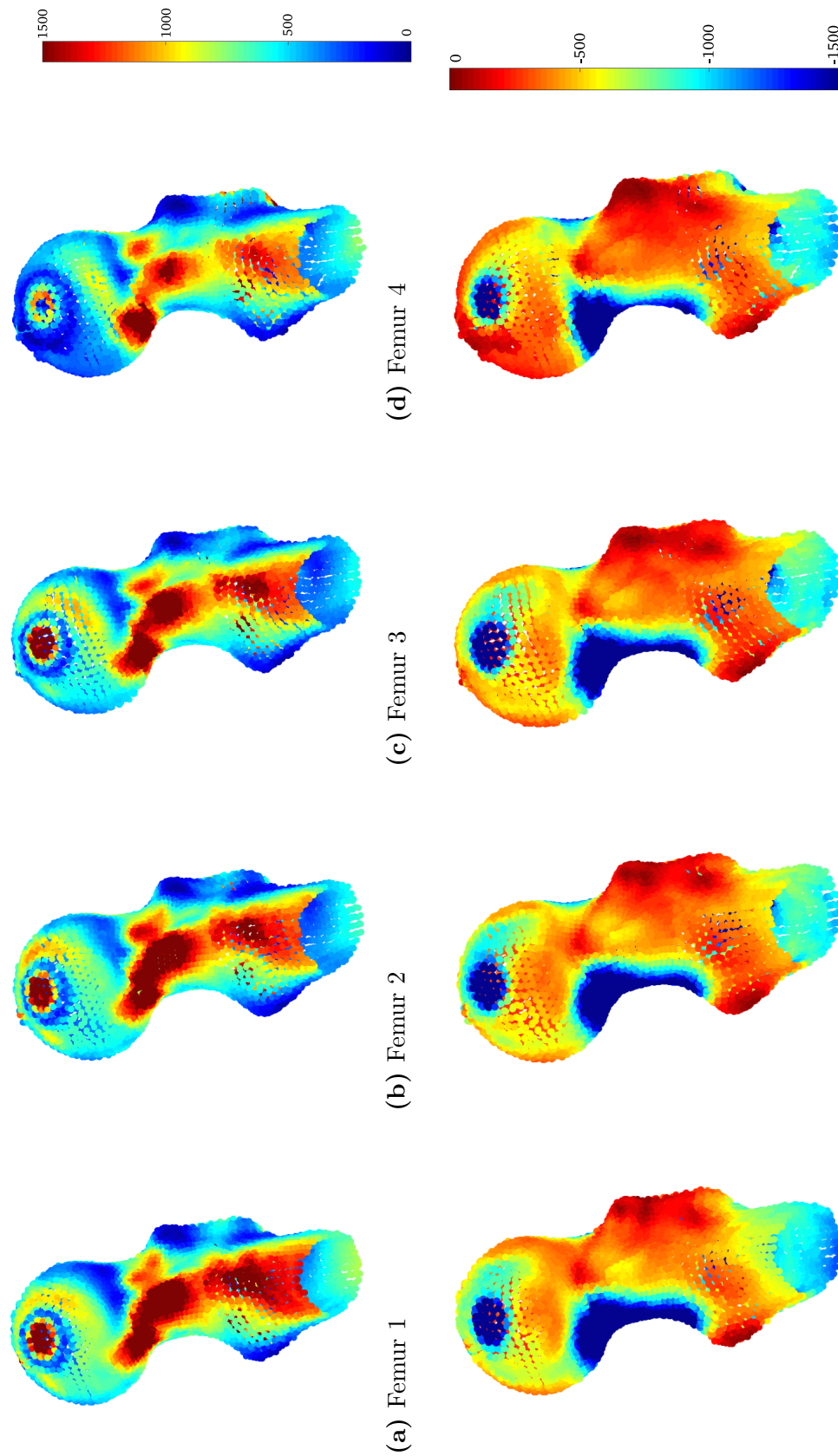


Figure C.5: Repeatability test of FE-models in model 5: major principal strains (top) and minor principal strains (bottom)

## Appendix D

### Validation with all DIC-data points at 1120 N

|         | Femur 1 | Femur 2 | Femur 3 | Femur 4 | Femur 5 |
|---------|---------|---------|---------|---------|---------|
| Model 1 | 0.430   | 0.533   | 0.549   | 0.280   | 0.510   |
| Model 2 | 0.436   | 0.548   | 0.552   | 0.279   | 0.516   |
| Model 3 | 0.431   | 0.541   | 0.547   | 0.278   | 0.511   |
| Model 4 | 0.421   | 0.514   | 0.591   | 0.299   | 0.509   |
| Model 5 | 0.433   | 0.536   | 0.551   | 0.279   | 0.513   |
| Model 6 | 0.436   | 0.549   | 0.552   | 0.280   | 0.515   |
| Model 7 | 0.424   | 0.513   | 0.592   | 0.300   | 0.509   |
| Model 8 | 0.308   | 0.325   | 0.321   | 0.163   | 0.327   |

**Table D.1:** Slope: Validation with all DIC-data points

|         | Femur 1 | Femur 2 | Femur 3 | Femur 4 | Femur 5 |
|---------|---------|---------|---------|---------|---------|
| Model 1 | 0.306   | 0.334   | 0.430   | 0.447   | 0.352   |
| Model 2 | 0.309   | 0.340   | 0.431   | 0.450   | 0.355   |
| Model 3 | 0.310   | 0.341   | 0.432   | 0.450   | 0.356   |
| Model 4 | 0.319   | 0.335   | 0.442   | 0.449   | 0.359   |
| Model 5 | 0.308   | 0.337   | 0.433   | 0.447   | 0.353   |
| Model 6 | 0.310   | 0.341   | 0.431   | 0.448   | 0.354   |
| Model 7 | 0.319   | 0.336   | 0.443   | 0.448   | 0.358   |
| Model 8 | 0.264   | 0.236   | 0.298   | 0.287   | 0.235   |

**Table D.2:**  $R^2$ : Validation with all DIC-data points

|         | Femur 1 | Femur 2 | Femur 3 | Femur 4 | Femur 5 |
|---------|---------|---------|---------|---------|---------|
| Model 1 | 35      | 28      | 7       | 41      | 2       |
| Model 2 | 37      | 32      | 11      | 45      | 7       |
| Model 3 | 35      | 29      | 7       | 42      | 4       |
| Model 4 | 48      | 17      | 35      | 51      | 11      |
| Model 5 | 37      | 32      | 11      | 41      | 5       |
| Model 6 | 38      | 34      | 11      | 41      | 5       |
| Model 7 | 49      | 18      | 36      | 48      | 9       |
| Model 8 | -97     | -105    | -121    | -52     | -96     |

**Table D.3:** Intercept  $[\mu\varepsilon]$ : Validation with all DIC-data points

|         | Femur 1 | Femur 2 | Femur 3 | Femur 4 | Femur 5 |
|---------|---------|---------|---------|---------|---------|
| Model 1 | 346     | 255     | 218     | 279     | 276     |
| Model 2 | 350     | 264     | 222     | 281     | 281     |
| Model 3 | 349     | 263     | 220     | 277     | 279     |
| Model 4 | 333     | 230     | 246     | 311     | 289     |
| Model 5 | 347     | 259     | 223     | 280     | 278     |
| Model 6 | 350     | 267     | 222     | 276     | 279     |
| Model 7 | 333     | 233     | 248     | 307     | 287     |
| Model 8 | 272     | 256     | 268     | 215     | 261     |

**Table D.4:** RMSE  $[\mu\varepsilon]$ : Validation with all DIC-data points

|         | Femur 1 | Femur 2 | Femur 3 | Femur 4 | Femur 5 |
|---------|---------|---------|---------|---------|---------|
| Model 1 | 9470    | 9101    | 7375    | 3219    | 8401    |
| Model 2 | 9583    | 9345    | 7405    | 3202    | 8484    |
| Model 3 | 9470    | 9220    | 7341    | 3194    | 8384    |
| Model 4 | 9245    | 8795    | 7891    | 3411    | 8347    |
| Model 5 | 9528    | 9137    | 7391    | 3210    | 8433    |
| Model 6 | 9585    | 9356    | 7408    | 3221    | 8470    |
| Model 7 | 9305    | 8772    | 7899    | 3435    | 8341    |
| Model 8 | 6604    | 5724    | 4463    | 1985    | 5572    |

**Table D.5:** Maximum absolute error [ $\mu\epsilon$ ]: Validation with all DIC-data points

|         | Slope | $R^2$ | Intercept | RMSE [ $\mu\epsilon$ ] | Maximum absolute error [ $\mu\epsilon$ ] |
|---------|-------|-------|-----------|------------------------|--|
| Model 1 | 0.450 | 0.362 | 24        | 284                    | 9916                                     |
| Model 2 | 0.450 | 0.365 | 28        | 293                    | 9902                                     |
| Model 3 | 0.446 | 0.365 | 25        | 291                    | 9827                                     |
| Model 4 | 0.458 | 0.372 | 32        | 289                    | 10099                                    |
| Model 5 | 0.450 | 0.364 | 27        | 288                    | 9920                                     |
| Model 6 | 0.450 | 0.365 | 27        | 293                    | 9909                                     |
| Model 7 | 0.461 | 0.371 | 32        | 288                    | 10147                                    |
| Model 8 | 0.270 | 0.261 | -93       | 271                    | 5740                                     |

**Table D.6:** Data pooled of all five specimen per model - 1120 N - whole DIC-point cloud

## Appendix E

### Validation against single DIC-tests at 1120 N



**Figure E.1:** Cropped section where data was validated (1600 data points)

The single tests were performed with the DIC-data points that were in focus during measurement and did not show high curvature.

**Model 1**

|        | Test 1 | Test 2 | Test 3 | Test 4 | Test 5 |
|--------|--------|--------|--------|--------|--------|
| Bone 1 | 0.686  | 0.759  | 0.742  | 0.738  | 0.675  |
| Bone 2 | 0.596  | 0.726  | 0.656  | 0.582  | 0.764  |
| Bone 3 | 0.645  | 0.598  | 0.532  | 0.532  | 0.530  |
| Bone 4 | 0.410  | 0.447  | 0.466  | 0.481  | 0.592  |
| Bone 5 | 0.640  | 0.595  | 0.436  | -      | 0.521  |

**Table E.1:** Slope:  
FE-models validated against single DIC-tests (Model 1)

|        | Test 1 | Test 2 | Test 3 | Test 4 | Test 5 |
|--------|--------|--------|--------|--------|--------|
| Bone 1 | 0.836  | 0.741  | 0.868  | 0.858  | 0.839  |
| Bone 2 | 0.815  | 0.767  | 0.887  | 0.860  | 0.863  |
| Bone 3 | 0.830  | 0.846  | 0.863  | 0.740  | 0.846  |
| Bone 4 | 0.831  | 0.772  | 0.634  | 0.756  | 0.791  |
| Bone 5 | 0.760  | 0.849  | 0.814  | -      | 0.806  |

**Table E.2:**  $R^2$ :  
FE-models validated against single DIC-tests (Model 1)

|        | Test 1 | Test 2 | Test 3 | Test 4 | Test 5 |
|--------|--------|--------|--------|--------|--------|
| Bone 1 | 31     | -111   | 98     | 104    | 6      |
| Bone 2 | 130    | 89     | 34     | 44     | -5     |
| Bone 3 | 75     | 55     | 88     | 14     | 89     |
| Bone 4 | 91     | -27    | 129    | 50     | 59     |
| Bone 5 | 11     | 128    | 35     | -      | 68     |

**Table E.3:** Intercept  $[\mu\varepsilon]$ :  
FE-models validated against single DIC-tests (Model 1)

|        | Test 1 | Test 2 | Test 3 | Test 4 | Test 5 |
|--------|--------|--------|--------|--------|--------|
| Bone 1 | 209    | 264    | 181    | 190    | 179    |
| Bone 2 | 196    | 228    | 144    | 182    | 175    |
| Bone 3 | 162    | 162    | 159    | 212    | 156    |
| Bone 4 | 156    | 172    | 218    | 191    | 166    |
| Bone 5 | 191    | 159    | 174    | -      | 181    |

**Table E.4:** RMSE  $[\mu\varepsilon]$ :  
FE-models validated against single DIC-tests (Model 1)

|        | Test 1 | Test 2 | Test 3 | Test 4 | Test 5 |
|--------|--------|--------|--------|--------|--------|
| Bone 1 | 725    | 1041   | 748    | 637    | 1100   |
| Bone 2 | 972    | 716    | 843    | 465    | 532    |
| Bone 3 | 813    | 593    | 374    | 703    | 571    |
| Bone 4 | 464    | 628    | 728    | 490    | 543    |
| Bone 5 | 720    | 494    | 606    | -      | 533    |

**Table E.5:** Maximum error  $[\mu\varepsilon]$ :  
FE-models validated against single DIC-tests (Model 1)

**Model 2**

|        | Test 1 | Test 2 | Test 3 | Test 4 | Test 5 |
|--------|--------|--------|--------|--------|--------|
| Bone 1 | 0.701  | 0.776  | 0.760  | 0.756  | 0.692  |
| Bone 2 | 0.635  | 0.767  | 0.693  | 0.616  | 0.810  |
| Bone 3 | 0.657  | 0.608  | 0.541  | 0.542  | 0.539  |
| Bone 4 | 0.412  | 0.447  | 0.473  | 0.484  | 0.596  |
| Bone 5 | 0.664  | 0.617  | 0.451  | -      | 0.538  |

**Table E.6:** Slope:  
FE-models validated against single DIC-tests (Model 2)

|        | Test 1 | Test 2 | Test 3 | Test 4 | Test 5 |
|--------|--------|--------|--------|--------|--------|
| Bone 1 | 0.834  | 0.742  | 0.869  | 0.859  | 0.841  |
| Bone 2 | 0.817  | 0.764  | 0.886  | 0.860  | 0.863  |
| Bone 3 | 0.830  | 0.847  | 0.863  | 0.741  | 0.848  |
| Bone 4 | 0.835  | 0.765  | 0.640  | 0.759  | 0.794  |
| Bone 5 | 0.758  | 0.849  | 0.811  | -      | 0.805  |

**Table E.7:**  $R^2$ :  
FE-models validated against single DIC-tests (Model 2)

|        | Test 1 | Test 2 | Test 3 | Test 4 | Test 5 |
|--------|--------|--------|--------|--------|--------|
| Bone 1 | 33     | -111   | 102    | 109    | 7      |
| Bone 2 | 137    | 93     | 36     | 44     | -7     |
| Bone 3 | 78     | 58     | 92     | 17     | 92     |
| Bone 4 | 100    | -19    | 138    | 58     | 67     |
| Bone 5 | 17     | 139    | 43     | -      | 76     |

**Table E.8:** Intercept  $[\mu\varepsilon]$ :  
FE-models validated against single DIC-tests (Model 2)

|        | Test 1 | Test 2 | Test 3 | Test 4 | Test 5 |
|--------|--------|--------|--------|--------|--------|
| Bone 1 | 216    | 270    | 185    | 195    | 182    |
| Bone 2 | 205    | 241    | 153    | 192    | 185    |
| Bone 3 | 164    | 164    | 162    | 215    | 158    |
| Bone 4 | 155    | 175    | 216    | 191    | 165    |
| Bone 5 | 198    | 165    | 183    | -      | 188    |

**Table E.9:** RMSE [ $\mu\varepsilon$ ]:  
FE-models validated against single DIC-tests (Model 2)

|        | Test 1 | Test 2 | Test 3 | Test 4 | Test 5 |
|--------|--------|--------|--------|--------|--------|
| Bone 1 | 737    | 1063   | 765    | 641    | 1125   |
| Bone 2 | 1040   | 747    | 888    | 513    | 558    |
| Bone 3 | 826    | 601    | 388    | 717    | 575    |
| Bone 4 | 456    | 618    | 751    | 486    | 536    |
| Bone 5 | 770    | 506    | 616    | -      | 558    |

**Table E.10:** Maximum absolute error [ $\mu\varepsilon$ ]:  
FE-models validated against single DIC-tests (Model 2)

**Model 3**

|        | Test 1 | Test 2 | Test 3 | Test 4 | Test 5 |
|--------|--------|--------|--------|--------|--------|
| Bone 1 | 0.696  | 0.771  | 0.754  | 0.748  | 0.685  |
| Bone 2 | 0.627  | 0.761  | 0.688  | 0.611  | 0.804  |
| Bone 3 | 0.648  | 0.601  | 0.535  | 0.536  | 0.532  |
| Bone 4 | 0.405  | 0.439  | 0.463  | 0.475  | 0.585  |
| Bone 5 | 0.656  | 0.609  | 0.445  | -      | 0.532  |

**Table E.11:** Slope:  
FE-models validated against single DIC-tests (Model 3)

|        | Test 1 | Test 2 | Test 3 | Test 4 | Test 5 |
|--------|--------|--------|--------|--------|--------|
| Bone 1 | 0.835  | 0.741  | 0.868  | 0.858  | 0.839  |
| Bone 2 | 0.815  | 0.765  | 0.885  | 0.861  | 0.864  |
| Bone 3 | 0.830  | 0.847  | 0.862  | 0.742  | 0.846  |
| Bone 4 | 0.834  | 0.766  | 0.639  | 0.759  | 0.793  |
| Bone 5 | 0.758  | 0.850  | 0.811  | -      | 0.805  |

**Table E.12:**  $R^2$ :  
FE-models validated against single DIC-tests (Model 3)

|        | Test 1 | Test 2 | Test 3 | Test 4 | Test 5 |
|--------|--------|--------|--------|--------|--------|
| Bone 1 | 30     | -114   | 98     | 105    | 4      |
| Bone 2 | 133    | 89     | 32     | 41     | -10    |
| Bone 3 | 74     | 54     | 88     | 13     | 88     |
| Bone 4 | 95     | -21    | 133    | 55     | 64     |
| Bone 5 | 13     | 133    | 39     | -      | 71     |

**Table E.13:** Intercept [ $\mu\varepsilon$ ]:  
FE-models validated against single DIC-tests (Model 3)

|        | Test 1 | Test 2 | Test 3 | Test 4 | Test 5 |
|--------|--------|--------|--------|--------|--------|
| Bone 1 | 213    | 268    | 184    | 194    | 182    |
| Bone 2 | 204    | 239    | 152    | 190    | 183    |
| Bone 3 | 163    | 162    | 160    | 212    | 156    |
| Bone 4 | 153    | 172    | 212    | 187    | 162    |
| Bone 5 | 196    | 162    | 181    | -      | 186    |

**Table E.14:** RMSE  $[\mu\varepsilon]$ :  
FE-models validated against single DIC-tests (Model 3)

|        | Test 1 | Test 2 | Test 3 | Test 4 | Test 5 |
|--------|--------|--------|--------|--------|--------|
| Bone 1 | 734    | 1059   | 762    | 641    | 1116   |
| Bone 2 | 1028   | 743    | 883    | 505    | 556    |
| Bone 3 | 816    | 595    | 382    | 710    | 574    |
| Bone 4 | 450    | 609    | 734    | 479    | 529    |
| Bone 5 | 755    | 502    | 613    | -      | 554    |

**Table E.15:** Maximum absolute error  $[\mu\varepsilon]$ :  
FE-models validated against single DIC-tests (Model 3)

**Model 4**

|        | Test 1 | Test 2 | Test 3 | Test 4 | Test 5 |
|--------|--------|--------|--------|--------|--------|
| Bone 1 | 0.674  | 0.748  | 0.731  | 0.730  | 0.666  |
| Bone 2 | 0.565  | 0.680  | 0.615  | 0.545  | 0.715  |
| Bone 3 | 0.728  | 0.673  | 0.600  | 0.599  | 0.597  |
| Bone 4 | 0.459  | 0.498  | 0.524  | 0.537  | 0.665  |
| Bone 5 | 0.681  | 0.633  | 0.462  | -      | 0.551  |

**Table E.16:** Slope:  
FE-models validated against single DIC-tests (Model 4)

|        | Test 1 | Test 2 | Test 3 | Test 4 | Test 5 |
|--------|--------|--------|--------|--------|--------|
| Bone 1 | 0.832  | 0.744  | 0.870  | 0.864  | 0.846  |
| Bone 2 | 0.818  | 0.765  | 0.888  | 0.859  | 0.861  |
| Bone 3 | 0.832  | 0.848  | 0.865  | 0.741  | 0.848  |
| Bone 4 | 0.830  | 0.764  | 0.638  | 0.752  | 0.796  |
| Bone 5 | 0.758  | 0.850  | 0.810  | -      | 0.805  |

**Table E.17:**  $R^2$ :  
FE-models validated against single DIC-tests (Model 4)

|        | Test 1 | Test 2 | Test 3 | Test 4 | Test 5 |
|--------|--------|--------|--------|--------|--------|
| Bone 1 | 48     | -92    | 113    | 119    | 23     |
| Bone 2 | 125    | 85     | 35     | 43     | -2     |
| Bone 3 | 93     | 72     | 109    | 26     | 109    |
| Bone 4 | 102    | -31    | 144    | 55     | 64     |
| Bone 5 | 14     | 139    | 42     | -      | 75     |

**Table E.18:** Intercept [ $\mu\varepsilon$ ]:  
FE-models validated against single DIC-tests (Model 4)

|        | Test 1 | Test 2 | Test 3 | Test 4 | Test 5 |
|--------|--------|--------|--------|--------|--------|
| Bone 1 | 208    | 260    | 177    | 183    | 172    |
| Bone 2 | 179    | 214    | 134    | 171    | 165    |
| Bone 3 | 181    | 182    | 178    | 238    | 173    |
| Bone 4 | 175    | 196    | 243    | 215    | 183    |
| Bone 5 | 203    | 168    | 188    | -      | 193    |

**Table E.19:** RMSE  $[\mu\varepsilon]$ :  
 FE-models validated against single DIC-tests (Model 4)

|        | Test 1 | Test 2 | Test 3 | Test 4 | Test 5 |
|--------|--------|--------|--------|--------|--------|
| Bone 1 | 688    | 1008   | 718    | 620    | 1063   |
| Bone 2 | 927    | 661    | 785    | 457    | 495    |
| Bone 3 | 906    | 654    | 428    | 791    | 644    |
| Bone 4 | 512    | 700    | 822    | 548    | 603    |
| Bone 5 | 788    | 522    | 632    | -      | 576    |

**Table E.20:** Maximum error  $[\mu\varepsilon]$ :  
 FE-models validated against single DIC-tests (Model 4)

**Model 5**

|        | Test 1 | Test 2 | Test 3 | Test 4 | Test 5 |
|--------|--------|--------|--------|--------|--------|
| Bone 1 | 0.691  | 0.765  | 0.748  | 0.744  | 0.681  |
| Bone 2 | 0.607  | 0.735  | 0.665  | 0.590  | 0.775  |
| Bone 3 | 0.659  | 0.610  | 0.544  | 0.545  | 0.542  |
| Bone 4 | 0.411  | 0.448  | 0.469  | 0.483  | 0.594  |
| Bone 5 | 0.649  | 0.603  | 0.441  | -      | 0.527  |

**Table E.21:** Slope:  
FE-models validated against single DIC-tests (Model 5)

|        | Test 1 | Test 2 | Test 3 | Test 4 | Test 5 |
|--------|--------|--------|--------|--------|--------|
| Bone 1 | 0.834  | 0.742  | 0.869  | 0.859  | 0.841  |
| Bone 2 | 0.818  | 0.765  | 0.887  | 0.859  | 0.862  |
| Bone 3 | 0.834  | 0.848  | 0.864  | 0.739  | 0.850  |
| Bone 4 | 0.832  | 0.770  | 0.635  | 0.756  | 0.791  |
| Bone 5 | 0.759  | 0.849  | 0.813  | -      | 0.805  |

**Table E.22:**  $R^2$ :  
FE-models validated against single DIC-tests (Model 5)

|        | Test 1 | Test 2 | Test 3 | Test 4 | Test 5 |
|--------|--------|--------|--------|--------|--------|
| Bone 1 | 35     | -108   | 102    | 109    | 10     |
| Bone 2 | 136    | 94     | 39     | 48     | -1     |
| Bone 3 | 81     | 61     | 95     | 19     | 96     |
| Bone 4 | 93     | -26    | 131    | 52     | 61     |
| Bone 5 | 15     | 135    | 41     | -      | 73     |

**Table E.23:** Intercept [ $\mu\varepsilon$ ]:  
FE-models validated against single DIC-tests (Model 5)

|        | Test 1 | Test 2 | Test 3 | Test 4 | Test 5 |
|--------|--------|--------|--------|--------|--------|
| Bone 1 | 212    | 266    | 182    | 191    | 179    |
| Bone 2 | 197    | 232    | 146    | 186    | 178    |
| Bone 3 | 163    | 164    | 162    | 217    | 158    |
| Bone 4 | 157    | 173    | 218    | 192    | 166    |
| Bone 5 | 193    | 161    | 177    | -      | 184    |

**Table E.24:** RMSE  $[\mu\varepsilon]$ :  
 FE-models validated against single DIC-tests (Model 5)

|        | Test 1 | Test 2 | Test 3 | Test 4 | Test 5 |
|--------|--------|--------|--------|--------|--------|
| Bone 1 | 724    | 1046   | 751    | 634    | 1104   |
| Bone 2 | 988    | 723    | 851    | 483    | 539    |
| Bone 3 | 823    | 596    | 388    | 724    | 571    |
| Bone 4 | 464    | 629    | 734    | 491    | 543    |
| Bone 5 | 743    | 496    | 608    | -      | 543    |

**Table E.25:** Maximum error  $[\mu\varepsilon]$ :  
 FE-models validated against single DIC-tests (Model 5)

**Model 6**

|        | Test 1 | Test 2 | Test 3 | Test 4 | Test 5 |
|--------|--------|--------|--------|--------|--------|
| Bone 1 | 0.702  | 0.778  | 0.762  | 0.757  | 0.694  |
| Bone 2 | 0.641  | 0.772  | 0.698  | 0.620  | 0.815  |
| Bone 3 | 0.658  | 0.609  | 0.542  | 0.543  | 0.539  |
| Bone 4 | 0.403  | 0.439  | 0.460  | 0.474  | 0.582  |
| Bone 5 | 0.657  | 0.611  | 0.447  | -      | 0.533  |

**Table E.26:** Slope:  
FE-models validated against single DIC-tests (Model 6)

|        | Test 1 | Test 2 | Test 3 | Test 4 | Test 5 |
|--------|--------|--------|--------|--------|--------|
| Bone 1 | 0.833  | 0.742  | 0.869  | 0.859  | 0.841  |
| Bone 2 | 0.818  | 0.763  | 0.886  | 0.860  | 0.862  |
| Bone 3 | 0.831  | 0.847  | 0.863  | 0.741  | 0.848  |
| Bone 4 | 0.833  | 0.770  | 0.636  | 0.758  | 0.791  |
| Bone 5 | 0.759  | 0.850  | 0.812  | -      | 0.805  |

**Table E.27:**  $R^2$ :  
FE-models validated against single DIC-tests (Model 6)

|        | Test 1 | Test 2 | Test 3 | Test 4 | Test 5 |
|--------|--------|--------|--------|--------|--------|
| Bone 1 | 34     | -110   | 103    | 110    | 8      |
| Bone 2 | 140    | 95     | 39     | 46     | -5     |
| Bone 3 | 78     | 58     | 92     | 17     | 93     |
| Bone 4 | 92     | -24    | 129    | 52     | 61     |
| Bone 5 | 14     | 135    | 40     | -      | 73     |

**Table E.28:** Intercept [ $\mu\varepsilon$ ]:  
FE-models validated against single DIC-tests (Model 6)

|        | Test 1 | Test 2 | Test 3 | Test 4 | Test 5 |
|--------|--------|--------|--------|--------|--------|
| Bone 1 | 216    | 271    | 186    | 195    | 182    |
| Bone 2 | 205    | 244    | 154    | 193    | 187    |
| Bone 3 | 164    | 164    | 162    | 215    | 158    |
| Bone 4 | 153    | 170    | 213    | 187    | 163    |
| Bone 5 | 196    | 163    | 180    | -      | 186    |

**Table E.29:** RMSE  $[\mu\varepsilon]$ :  
FE-models validated against single DIC-tests (Model 6)

|        | Test 1 | Test 2 | Test 3 | Test 4 | Test 5 |
|--------|--------|--------|--------|--------|--------|
| Bone 1 | 737    | 1065   | 765    | 641    | 1126   |
| Bone 2 | 1047   | 750    | 892    | 523    | 561    |
| Bone 3 | 827    | 601    | 389    | 719    | 575    |
| Bone 4 | 454    | 614    | 723    | 480    | 531    |
| Bone 5 | 754    | 505    | 614    | -      | 551    |

**Table E.30:** Maximum error  $[\mu\varepsilon]$ :  
FE-models validated against single DIC-tests (Model 6)

**Model 7**

|        | Test 1 | Test 2 | Test 3 | Test 4 | Test 5 |
|--------|--------|--------|--------|--------|--------|
| Bone 1 | 0.676  | 0.751  | 0.734  | 0.733  | 0.669  |
| Bone 2 | 0.570  | 0.684  | 0.618  | 0.548  | 0.720  |
| Bone 3 | 0.734  | 0.679  | 0.605  | 0.606  | 0.602  |
| Bone 4 | 0.451  | 0.492  | 0.514  | 0.529  | 0.654  |
| Bone 5 | 0.674  | 0.627  | 0.458  | -      | 0.547  |

**Table E.31:** Slope:  
FE-models validated against single DIC-tests (Model 7)

|        | Test 1 | Test 2 | Test 3 | Test 4 | Test 5 |
|--------|--------|--------|--------|--------|--------|
| Bone 1 | 0.831  | 0.745  | 0.870  | 0.865  | 0.847  |
| Bone 2 | 0.819  | 0.764  | 0.888  | 0.858  | 0.860  |
| Bone 3 | 0.834  | 0.848  | 0.866  | 0.740  | 0.850  |
| Bone 4 | 0.828  | 0.768  | 0.635  | 0.751  | 0.793  |
| Bone 5 | 0.758  | 0.850  | 0.810  | -      | 0.805  |

**Table E.32:**  $R^2$ :  
FE-models validated against single DIC-tests (Model 7)

|        | Test 1 | Test 2 | Test 3 | Test 4 | Test 5 |
|--------|--------|--------|--------|--------|--------|
| Bone 1 | 49     | -91    | 115    | 121    | 24     |
| Bone 2 | 126    | 87     | 37     | 44     | -1     |
| Bone 3 | 95     | 74     | 111    | 28     | 112    |
| Bone 4 | 95     | -36    | 136    | 50     | 58     |
| Bone 5 | 11     | 135    | 39     | -      | 72     |

**Table E.33:** Intercept [ $\mu\varepsilon$ ]:  
FE-models validated against single DIC-tests (Model 7)

|        | Test 1 | Test 2 | Test 3 | Test 4 | Test 5 |
|--------|--------|--------|--------|--------|--------|
| Bone 1 | 210    | 261    | 178    | 183    | 172    |
| Bone 2 | 180    | 216    | 135    | 172    | 167    |
| Bone 3 | 181    | 183    | 179    | 240    | 174    |
| Bone 4 | 174    | 191    | 240    | 212    | 181    |
| Bone 5 | 201    | 167    | 186    | -      | 191    |

**Table E.34:** RMSE  $[\mu\varepsilon]$ :  
FE-models validated against single DIC-tests (Model 7)

|        | Test 1 | Test 2 | Test 3 | Test 4 | Test 5 |
|--------|--------|--------|--------|--------|--------|
| Bone 1 | 689    | 1011   | 719    | 619    | 1066   |
| Bone 2 | 936    | 663    | 788    | 463    | 497    |
| Bone 3 | 911    | 656    | 433    | 804    | 644    |
| Bone 4 | 511    | 695    | 799    | 542    | 560    |
| Bone 5 | 773    | 521    | 629    | -      | 570    |

**Table E.35:** Maximum error  $[\mu\varepsilon]$ :  
FE-models validated against single DIC-tests (Model 7)

**Model 8**

|        | Test 1 | Test 2 | Test 3 | Test 4 | Test 5 |
|--------|--------|--------|--------|--------|--------|
| Bone 1 | 0.237  | 0.262  | 0.251  | 0.246  | 0.227  |
| Bone 2 | 0.221  | 0.257  | 0.237  | 0.211  | 0.287  |
| Bone 3 | 0.236  | 0.224  | 0.195  | 0.199  | 0.194  |
| Bone 4 | 0.115  | 0.129  | 0.129  | 0.135  | 0.170  |
| Bone 5 | 0.224  | 0.211  | 0.149  | -      | 0.177  |

**Table E.36:** Slope:  
FE-models validated against single DIC-tests (Model 8)

|        | Test 1 | Test 2 | Test 3 | Test 4 | Test 5 |
|--------|--------|--------|--------|--------|--------|
| Bone 1 | 0.798  | 0.707  | 0.815  | 0.782  | 0.753  |
| Bone 2 | 0.734  | 0.697  | 0.832  | 0.802  | 0.853  |
| Bone 3 | 0.768  | 0.814  | 0.816  | 0.736  | 0.813  |
| Bone 4 | 0.809  | 0.770  | 0.606  | 0.725  | 0.793  |
| Bone 5 | 0.719  | 0.824  | 0.762  | -      | 0.721  |

**Table E.37:**  $R^2$ :  
FE-models validated against single DIC-tests (Model 8)

|        | Test 1 | Test 2 | Test 3 | Test 4 | Test 5 |
|--------|--------|--------|--------|--------|--------|
| Bone 1 | -64    | -113   | -37    | -31    | -68    |
| Bone 2 | -22    | -33    | -55    | -52    | -77    |
| Bone 3 | -33    | -42    | -28    | -59    | -25    |
| Bone 4 | -14    | -47    | -5     | -26    | -24    |
| Bone 5 | -58    | -17    | -45    | -      | -35    |

**Table E.38:** Intercept [ $\mu\varepsilon$ ]:  
FE-models validated against single DIC-tests (Model 8)

|        | Test 1 | Test 2 | Test 3 | Test 4 | Test 5 |
|--------|--------|--------|--------|--------|--------|
| Bone 1 | 82     | 98     | 75     | 79     | 80     |
| Bone 2 | 87     | 95     | 65     | 79     | 68     |
| Bone 3 | 72     | 64     | 68     | 83     | 66     |
| Bone 4 | 47     | 48     | 63     | 58     | 47     |
| Bone 5 | 77     | 59     | 66     | -      | 75     |

**Table E.39:** RMSE [ $\mu\varepsilon$ ]  
FE-models validated against single DIC-tests (Model 8)

|        | Test 1 | Test 2 | Test 3 | Test 4 | Test 5 |
|--------|--------|--------|--------|--------|--------|
| Bone 1 | 336    | 381    | 277    | 275    | 448    |
| Bone 2 | 413    | 386    | 340    | 302    | 228    |
| Bone 3 | 333    | 261    | 243    | 241    | 211    |
| Bone 4 | 135    | 188    | 191    | 143    | 156    |
| Bone 5 | 243    | 218    | 234    | -      | 296    |

**Table E.40:** Maximum error [ $\mu\varepsilon$ ]  
FE-models validated against single DIC-tests (Model 8)

# Bibliography

- [1] P. Augat, D. Weyand, S. Panzer, and T. Klier. Osteoporosis prevalence and fracture characteristics in elderly female patients with fractures. *Archives of orthopaedic and trauma surgery*, 130(11):1405–1410, 2010.
- [2] S. D. Berry and R. R. Miller. Falls: epidemiology, pathophysiology, and relationship to fracture. *Current osteoporosis reports*, 6(4):149–154, 2008.
- [3] M. Bessho, I. Ohnishi, J. Matsuyama, T. Matsumoto, K. Imai, and K. Nakamura. Prediction of strength and strain of the proximal femur by a ct-based finite element method. *Journal of biomechanics*, 40(8):1745–1753, 2007.
- [4] J. D. Blaha and C. M. Logue. The biomechanics of hip fractures. *Techniques in Orthopaedics*, 4(2):7–18, 1989.
- [5] C. E. Canal, C. T. Hung, and G. A. Ateshian. Two-dimensional strain fields on the cross-section of the bovine humeral head under contact loading. *Journal of biomechanics*, 41(15):3145–3151, 2008.
- [6] S.-F. Chuang, C.-H. Chang, and T. Y.-F. Chen. Contraction behaviors of dental composite restorations—finite element investigation with dic validation. *Journal of the mechanical behavior of biomedical materials*, 4(8):2138–2149, 2011.
- [7] D. D. Cody, G. J. Gross, F. J. Hou, H. J. Spencer, S. A. Goldstein, and D. P. Fyhrie. Femoral strength is better predicted by finite element models than qct and dxa. *Journal of biomechanics*, 32(10):1013–1020, 1999.

- [8] C. Cooper, E. J. Atkinson, S. J. Jacobsen, W. M. O'Fallon, and L. J. Melton. Population-based study of survival after osteoporotic fractures. *American journal of epidemiology*, 137(9):1001–1005, 1993.
- [9] C. Cooper, G. Campion, and L. r. Melton. Hip fractures in the elderly: a world-wide projection. *Osteoporosis international*, 2(6):285–289, 1992.
- [10] A. C. Courtney, E. F. Wachtel, E. R. Myers, and W. C. Hayes. Age-related reductions in the strength of the femur tested in a fall-loading configuration. *J Bone Joint Surg Am*, 77(3):387–395, 1995.
- [11] S. R. Cummings and L. J. Melton. Epidemiology and outcomes of osteoporotic fractures. *The Lancet*, 359(9319):1761–1767, 2002.
- [12] P. D. Delmas. Treatment of postmenopausal osteoporosis. *The Lancet*, 359(9322):2018–2026, 2002.
- [13] J. O. Den Buijs and D. Dragomir-Daescu. Validated finite element models of the proximal femur using two-dimensional projected geometry and bone density. *Computer methods and programs in biomedicine*, 104(2):168–174, 2011.
- [14] A. Dickinson, A. Taylor, H. Ozturk, and M. Browne. Experimental validation of a finite element model of the proximal femur using digital image correlation and a composite bone model. *Journal of biomechanical engineering*, 133(1):014504, 2011.
- [15] J. Elfar, S. Stanbury, R. M. G. Menorca, and J. D. Reed. Composite bone models in orthopaedic surgery research and education. *The Journal of the American Academy of Orthopaedic Surgeons*, 22(2):111, 2014.
- [16] Q. Fang. iso2mesh. Technical report, Photon Migration Lab, Massachusetts General Hospital (Harvard Medical School), 2008.

- [17] M. P. Gardner, A. C. Chong, A. G. Pollock, and P. H. Wooley. Mechanical evaluation of large-size fourth-generation composite femur and tibia models. *Annals of biomedical engineering*, 38(3):613–620, 2010.
- [18] L. Grassi. *Femoral strength prediction using finite element models*. PhD thesis, 2016.
- [19] L. Grassi and H. Isaksson. Extracting accurate strain measurements in bone mechanics: a critical review of current methods. *Journal of the mechanical behavior of biomedical materials*, 50:43–54, 2015.
- [20] L. Grassi, E. Schileo, F. Taddei, L. Zani, M. Juszczuk, L. Cristofolini, and M. Viceconti. Accuracy of finite element predictions in sideways load configurations for the proximal human femur. *Journal of biomechanics*, 45(2):394–399, 2012.
- [21] L. Grassi, S. P. Väänänen, M. Ristinmaa, J. S. Jurvelin, and H. Isaksson. How accurately can subject-specific finite element models predict strains and strength of human femora? investigation using full-field measurements. *Journal of biomechanics*, 49(5):802–806, 2016.
- [22] L. Grassi, S. P. Väänänen, S. A. Yavari, H. Weinans, J. S. Jurvelin, A. A. Zadpoor, and H. Isaksson. Experimental validation of finite element model for proximal composite femur using optical measurements. *Journal of the mechanical behavior of biomedical materials*, 21:86–94, 2013.
- [23] A. D. Heiner. Structural properties of fourth-generation composite femurs and tibias. *Journal of biomechanics*, 41(15):3282–3284, 2008.
- [24] O. Johnell and J. Kanis. <https://www.sheffield.ac.uk/frax/tool.jsp?lang=en>. 15-05-2017.

- [25] O. Johnell and J. Kanis. An estimate of the worldwide prevalence, mortality and disability associated with hip fracture. *Osteoporosis International*, 15(11):897–902, 2004.
- [26] O. Johnell and J. Kanis. An estimate of the worldwide prevalence and disability associated with osteoporotic fractures. *Osteoporosis international*, 17(12):1726–1733, 2006.
- [27] L. Joseph Melton. A “gompertzian” view of osteoporosis. *Calcified tissue international*, 46(5):285–286, 1990.
- [28] J. Kanis, A. Odén, O. Johnell, H. Johansson, C. De Laet, J. Brown, P. Burckhardt, C. Cooper, C. Christiansen, S. Cummings, et al. The use of clinical risk factors enhances the performance of bmd in the prediction of hip and osteoporotic fractures in men and women. *Osteoporosis international*, 18(8):1033–1046, 2007.
- [29] G. S. Keene, M. J. Parker, and G. A. Pryor. Mortality and morbidity after hip fractures. *Bmj*, 307(6914):1248–1250, 1993.
- [30] R. Kerr, D. Resnick, D. J. Sartoris, S. Kursunoglu, C. Pineda, P. Haghighi, G. Greenway, and J. Guerra. Computerized tomography of proximal femoral trabecular patterns. *Journal of orthopaedic research*, 4(1):45–56, 1986.
- [31] J. E. Koivumäki, J. Thevenot, P. Pulkkinen, V. Kuhn, T. M. Link, F. Eckstein, and T. Jämsä. Cortical bone finite element models in the estimation of experimentally measured failure loads in the proximal femur. *Bone*, 51(4):737–740, 2012.
- [32] J. E. Koivumäki, J. Thevenot, P. Pulkkinen, V. Kuhn, T. M. Link, F. Eckstein, and T. Jämsä. Ct-based finite element models can be used to estimate experimentally measured failure loads in the proximal femur. *Bone*, 50(4):824–829, 2012.

- [33] J. Lotz, E. Cheal, and W. C. Hayes. Fracture prediction for the proximal femur using finite element models: part ii—nonlinear analysis. *J Biomech Eng*, 113(4):361–365, 1991.
- [34] J. Magaziner, E. M. Simonsick, T. M. Kashner, J. R. Hebel, and J. E. Kenzora. Predictors of functional recovery one year following hospital discharge for hip fracture: a prospective study. *Journal of gerontology*, 45(3):M101–M107, 1990.
- [35] P. M. Mayhew, C. D. Thomas, J. G. Clement, N. Loveridge, T. J. Beck, W. Bonfield, C. J. Burgoyne, and J. Reeve. Relation between age, femoral neck cortical stability, and hip fracture risk. *The Lancet*, 366(9480):129–135, 2005.
- [36] M. M. McCarron and B. J. Devine. Clinical pharmacy: Case studies: Case number 25 gentamicin therapy. *Drug Intelligence & Clinical Pharmacy*, 8(11):650–655, 1974.
- [37] K. M. Moerman, C. A. Holt, S. L. Evans, and C. K. Simms. Digital image correlation and finite element modelling as a method to determine mechanical properties of human soft tissue in vivo. *Journal of biomechanics*, 42(8):1150–1153, 2009.
- [38] W. H. Organization et al. Assessment of fracture risk and its application to screening for postmenopausal osteoporosis: report of a who study group [meeting held in rome from 22 to 25 june 1992]. 1994.
- [39] W. H. Organization et al. Who scientific group on the assessment of osteoporosis at primary health care level. In *Summary meeting report*, pages 5–7, 2004.
- [40] M. Palanca, G. Tozzi, and L. Cristofolini. The use of digital image correlation in the biomechanical area: a review. *International biomechanics*, 3(1):1–21, 2016.
- [41] B. Pan, K. Qian, H. Xie, and A. Asundi. Two-dimensional digital image correlation for in-plane displacement and strain measurement: a review. *Measurement science and technology*, 20(6):062001, 2009.

- [42] K. H. Rubin, T. Friis-Holmberg, A. P. Hermann, B. Abrahamsen, and K. Brixen. Risk assessment tools to identify women with increased risk of osteoporotic fracture: complexity or simplicity? a systematic review. *Journal of Bone and Mineral Research*, 28(8):1701–1717, 2013.
- [43] P. Sambrook and C. Cooper. Osteoporosis. *Lancet*, 367(9527):2010–2018, 2006.
- [44] E. Schileo, E. Dall’Ara, F. Taddei, A. Malandrino, T. Schotkamp, M. Baleani, and M. Viceconti. An accurate estimation of bone density improves the accuracy of subject-specific finite element models. *Journal of biomechanics*, 41(11):2483–2491, 2008.
- [45] E. Schileo, F. Taddei, L. Cristofolini, and M. Viceconti. Subject-specific finite element models implementing a maximum principal strain criterion are able to estimate failure risk and fracture location on human femurs tested in vitro. *Journal of biomechanics*, 41(2):356–367, 2008.
- [46] D. G. Seeley, W. S. Browner, M. C. Nevitt, H. K. Genant, J. C. Scott, and S. R. Cummings. Which fractures are associated with low appendicular bone mass in elderly women? *Annals of internal medicine*, 115(11):837–842, 1991.
- [47] S. L. Silverman and A. D. Calderon. The utility and limitations of frax: a us perspective. *Current osteoporosis reports*, 8(4):192–197, 2010.
- [48] N. Trabelsi, Z. Yosibash, and C. Milgrom. Validation of subject-specific automated p-fe analysis of the proximal femur. *Journal of biomechanics*, 42(3):234–241, 2009.
- [49] N. Trabelsi, Z. Yosibash, C. Wutte, P. Augat, and S. Eberle. Patient-specific finite element analysis of the human femur—a double-blinded biomechanical validation. *Journal of biomechanics*, 44(9):1666–1672, 2011.

- [50] M. Trotter and G. C. Gleser. Estimation of stature from long bones of american whites and negroes. *American journal of physical anthropology*, 10(4):463–514, 1952.
- [51] A. Unnanuntana, B. P. Gladnick, E. Donnelly, and J. M. Lane. The assessment of fracture risk. *J Bone Joint Surg Am*, 92:743–53, 2010.
- [52] S. P. Väänänen, S. A. Yavari, H. Weinans, A. A. Zadpoor, J. S. Jurvelin, and H. Isaksson. Repeatability of digital image correlation for measurement of surface strains in composite long bones. *Journal of biomechanics*, 46(11):1928–1932, 2013.
- [53] N. B. Watts, B. Ettinger, and M. S. LeBoff. Frax facts. *Journal of Bone and Mineral Research*, 24(6):975–979, 2009.
- [54] S. A. Yavari, J. van der Stok, H. Weinans, and A. A. Zadpoor. Full-field strain measurement and fracture analysis of rat femora in compression test. *Journal of biomechanics*, 46(7):1282–1292, 2013.
- [55] L. Zani, L. Cristofolini, M. M. Juszczuk, L. Grassi, and M. Viceconti. A new paradigm for the in vitro simulation of sideways fall loading of the proximal human femur. *Journal of Mechanics in Medicine and Biology*, 14(01):1450005, 2014.